Politecnico di Torino

in collaboration with Royal Melbourne Institute of Technology

Master's Degree in Aerospace Engineering
A.a. 2024/2025
Graduation session December 2025

Numerical and Experimental Investigation of Small Ducted Propellers in Ground Effect

Supervisors:
Prof. Emanuele Martelli
Dr. Vincenzo Muscarello
Prof. Pier Marzocca

Candidate:
Fatime Kuci

Acknowledgements

Many thanks to Pier Marzocca for welcoming us to Australia, believing in our potential, and supporting our work throughout this entire period.

A big thank you to Vincenzo Muscarello and Paul Kantzidis for their continuous support and constant encouragement. The time they dedicated to us allowed us to improve our work step by step; their great trust in us and patience were far from obvious and were truly appreciated, making a real difference.

I would like to thank my supervisor, Emanuele Martelli, for supporting me and agreeing to follow me in this work from the very beginning.

Thanks to all the technical staff at RMIT for their availability and the support they provided us.

I thank my friend Nicoleta for sharing these months with me, through laughter, moments of frustration, and the unforgettable experiences we lived together in this new land. Without you, it wouldn't have been the same.

Finally, my deepest gratitude goes to my sister for understanding me and standing by me throughout my studies, to my brother for being a constant point of reference, and to my mom and dad for always supporting me and giving me the freedom to make my own choices without pressure. My thanks also go to my cousins Klaudia and Matilda, who have been like sisters I could always count on, and to all my family and friends for appreciating me and never making me feel alone. Every achievement of mine is also yours.

Abstract

This work investigates the aerodynamic behavior of small ducted propellers operating in ground effect using a combined numerical and experimental approach. Simulations were carried out with the mid-fidelity vortex-based solver DUST and validated against measurements obtained in a controlled indoor environment. The study focused on the baseline propeller and two modified configurations with different twist angles. Results indicate that, in out of ground effect (OGE) conditions, the duct increases total thrust compared to the isolated propeller. In ground effect (IGE) conditions, the duct consistently reduces total thrust, showing a behavior adverse to thrust generation. Comparison with literature data highlights similarities and differences with respect to similar configurations. The study underlines the importance of understanding the duct's influence in ground effect, as it can generate significant instabilities and represents a key component in the design of urban mobility systems based on small rotors.

Questo lavoro analizza il comportamento aerodinamico di piccoli propulsori intubati operanti in effetto suolo, attraverso un approccio combinato numerico e sperimentale. Le simulazioni sono state eseguite con il codice DUST, un solver a vortici di media fedeltà, e validate mediante misure sperimentali ottenute in un ambiente controllato indoor. Lo studio si è concentrato sull'elica di riferimento e su due configurazioni modificate caratterizzate da differenti angoli di twist. I risultati mostrano che, in condizioni fuori dall'effetto suolo (OGE), il condotto aumenta la spinta totale rispetto all'elica isolata. In condizioni di effetto suolo (IGE), invece, il condotto riduce sistematicamente la spinta totale, mostrando un comportamento sfavorevole alla generazione di spinta. Il confronto con i dati disponibili in letteratura evidenzia analogie e differenze rispetto a configurazioni simili. Lo studio sottolinea l'importanza di comprendere l'influenza del condotto in effetto suolo, poiché esso può generare significative instabilità e rappresenta un elemento chiave nella progettazione di sistemi di mobilità urbana basati su piccoli rotori.

Contents

Chapter 1

Introduction

Over the past two decades, unmanned aerial vehicles (UAVs) have gained increasing importance in the aviation sector, owing to their versatility in adapting to different mission profiles while maintaining relatively low operational costs [1].

These aircraft, which do not carry a human operator, are commonly known as drones. They can be either remotely piloted or operate autonomously, thanks to advances in navigation, remote control technologies, and energy storage systems that enable flights over long distances.

The use of such vehicles is highly valuable, as it enables operations in environments hazardous to humans, provides a partial alternative to satellite imagery, facilitates the delivery of goods in developing countries, allows the inspection of confined spaces [2], and supports the exploration of planets that remain beyond human reach.

Clearly, depending on the mission target, the types of drones and their equipment vary [3]. Hassanalian et al. [3], in their work, developed a comprehensive classification of existing drones, Figure 1.1, based on several parameters such as weight, wingspan, wing loading, range, maximum altitude, speed, endurance, and production costs, after a careful review of previous categorizations of these aircraft. Drones can have extremely different dimensions, also thanks to technological developments; Figure 1.2 shows the wide range of this spectrum.

As can be observed, the range of aircraft categories is very broad, with distinctions also based on the type of propulsion system employed. For instance, MAVs typically use electric motors, whereas UAVs are generally powered by fuel.

HTOLs are fixed-wing aircraft designed for horizontal take-off and landing, while VTOLs do not require a runway since they are capable of vertical flight. These are rotary-wing vehicles, although they are limited in terms of maximum speed. To combine the advantages of both configurations, hybrid drones such as tilt-rotors and ducted fans have been developed.

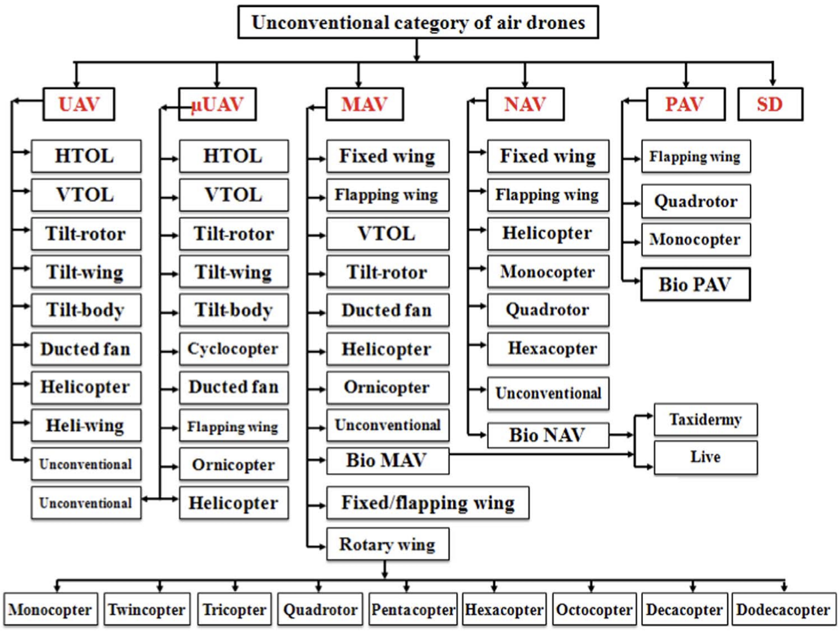

Figure 1.1: Drones classification , ref [3].

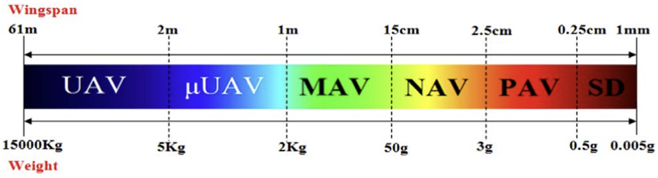

Figure 1.2: Spectrum of drones from UAV to SD, ref [3].

Drones intended for civilian applications, as well as for military use, are attracting significant interest. However, enabling the operation of autonomous drones in urban environments requires major scientific advancements and the establishment of an appropriate regulatory framework, since particular attention must always be devoted to ensuring public safety and mitigating both the acoustic and environmental impact of these vehicles.

Among the various aspects that influence their design and operation, aerodynamic interactions with the surrounding environment play a crucial role. In particular, one of the main challenges in the study of such vehicles is represented by the ground effect, which significantly alters aerodynamic behavior when flying close to surfaces and obstacles, such as buildings. This phenomenon introduces instabilities and changes in performance that must be thoroughly understood. Detailed knowledge of the ground effect is therefore crucial, not only to predict

Figure 1.3: Examples of drone applications in environmental protection, ref [3].

vehicle behavior accurately, but also to support the design of control systems and to enable future applications in complex environments, including urban areas on Earth and extraterrestrial surfaces, such as Mars [4].

In this thesis, the ground effect phenomenon will be investigated by analyzing how proximity to the ground influences the performance of a ducted propeller. This work builds upon a previous project that focused on a scaled three-bladed 15-inch propeller, conducted within the framework of the HOVERA project [5], a student-designed electric vertical take-off and landing (eVTOL) aircraft developed at RMIT University, with the same propeller now equipped with a duct.
The investigation approaches the problem from both a numerical and experimental perspective. Numerically, the DUST software [6] is employed to model the ground effect using the image method, while experimental tests are performed to validate the computational results and provide a comprehensive understanding of the ducted propeller behavior in near-ground conditions.

The overall work will be presented as follows: in Chapter 2, the HOVERA drone will be described in more detail, and some fundamental characteristics of the propellers will be introduced, which will be useful for understanding the subsequent chapters.
Chapter 3 focuses in detail on the ground effect, providing an explanation of its physical nature. This is followed by an introduction to the existing thrust theories and a discussion of the main methods employed to predict ground influence.
Chapter 4 is dedicated to the literature review and is divided into three sections: the first presents an in-depth discussion on the advantages of using ducts and coaxial rotors in drones; the second reviews existing experimental studies on ground effect; and the third focuses on numerical simulations Chapter 5 presents the numerical

analysis, including a detailed description of the DUST software and the setup of the numerical model, followed by the discussion of the obtained results. Chapter 6 is devoted to the experimental tests, providing a description of the experimental setup and the presentation of the results. Both chapters include an investigation of the effects that the presence of a duct has on the propeller performance, both in proximity to the ground and in free air conditions.
And the final chapter presents the conclusions of the entire work.

Chapter 2

HOVERA

The Hovera is a drone developed by a team of students from RMIT University in Melbourne to participate in the GoFly competition in 2018, sponsored by Boeing. This competition required the design of an electric vertical take-off and landing (E-VTOL) aircraft capable of carrying a human pilot.
The personal flying device had to meet very strict requirements: it had to be safe, quiet, extremely compact, and exhibit characteristics similar to a traditional VTOL aircraft. In addition, it was required to transport a person for at least 20 miles without the need for refueling or recharging. Figure 2.3 shows the appearance of the Hovera in 2020. The structure consists of two contra-rotating propellers enclosed within a duct, a landing gear with suspension, eight electric ducted fans for attitude control, a forward-facing electric ducted fan, and a seat for the dummy pilot.

Figure 2.1: GoFly 2018, ref [5].

Figure 2.2: GoFly 2019, ref [5].

Over the years, different teams and students have contributed to the Hovera project with small incremental developments.

In 2018, a design inspired by the Hiller Pawnee (1955) was proposed; however, this configuration proved to be unstable, and the design was rethought in subsequent years, Figure 2.1. In 2019, the project evolved from a single-fan design to a lower-risk quadrotor configuration using the well proven Pixhawk autopilot and open-source software, Figure 2.2.

By 2020, the current Hovera design was adopted, and a test rig was created to evaluate the main motor, measuring RPM, voltage, current, noise, and temperature at a height of 1 metre above the ground to avoid ground effect interference. In the following years, several improvements were made to the project, such as landing gear design, structural reinforcement, and power system upgrades; however, the overall structure has remained largely unchanged since 2020. Progress was significantly slowed by the COVID-19 pandemic, [5].

Figure 2.3: Hovera of RMIT, ref [5].

Over the years, however, no dedicated study on the ground effect has ever been carried out; on the contrary, efforts have generally aimed at operating away from such conditions. The purpose of this work is therefore to begin filling this gap by investigating the ground effect, starting with a single propeller equipped with a duct. Experimental testing will not be performed directly on the full Hovera, as this is currently challenging; instead, tests will be conducted on a simplified model. Nevertheless, a brief overview of the Hovera, which forms the basis of this project, is provided, with a description of the relevant drone components and their geometrical characteristics. CAD models of the craft and the test rig are included in the appendix, ref. [7].

2.0.1 Overview of the Hovera Drone Components

One of the main components of the Hovera aircraft is the duct, which is composed of several subassemblies, including the upper and lower airframe, the upper and lower central hub, and the side shroud. The duct dimensions are shown in Figure 2.4. The central hub is designed to house the motor at the core of the aircraft. The main rotors are responsible for generating thrust. The Hovera is equipped with two main rotors, positioned 145.12 mm apart. Their dimensions, together with those of the motor assembly, are illustrated in Figure 2.5.

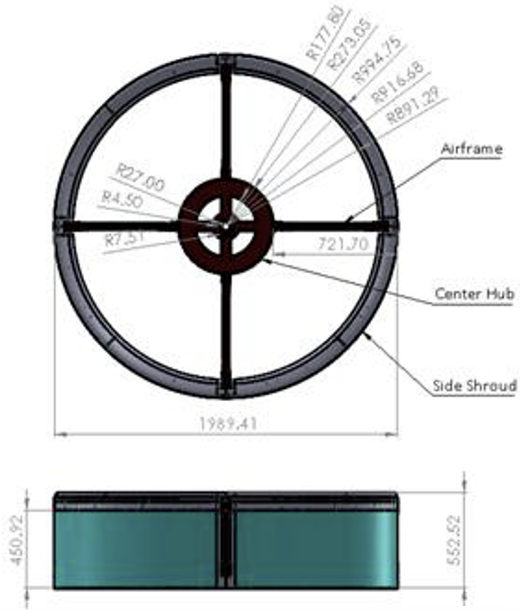

Figure 2.4: Duct dimensions, ref [7].

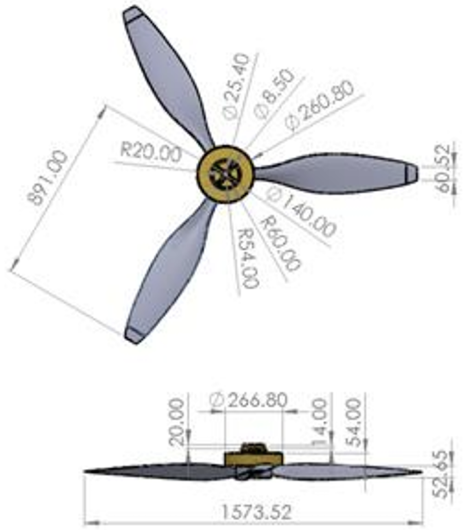

Figure 2.5: Main motor and rotor dimensions, ref [7].

2.1 Propeller Geometric Characteristics

To provide a clearer understanding and facilitate the reading of this text, it is useful to introduce the main geometric and aerodynamic characteristics of a propeller. This section is based on the work of G. Mangialomini [8].

A propeller generates thrust according to Newton's third law of motion and consists of two main components, the hub and the blades, with the latter responsible for producing the pulling force (thrust).
Propellers are often twisted, meaning they have a variable pitch, to ensure uniform lift along the blade span. The geometric pitch, β, represents the angle formed by the chord with the plane of the propeller disk, while the aerodynamic pitch, β_0, is measured relative to the zero lift line, as shown in Figure 2.6. Another important parameter is the pitch, $p = \pi D \cdot \tan\beta$, which represents the distance a propeller would theoretically advance along its axis after one complete rotation, also referred to as the geometric pitch. The actual distance traveled by the propeller is the true pitch or advance, and the difference between geometric and true pitch is known as slip.

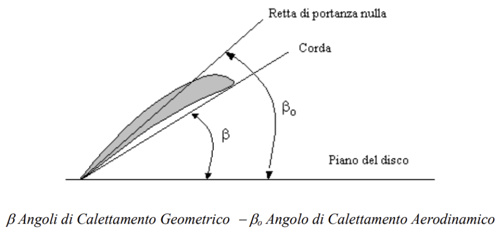

Figure 2.6: Geometric and Aerodynamic Pitch of the Propeller [8].

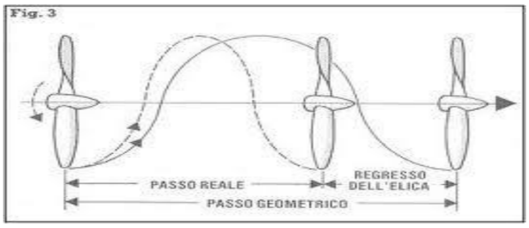

Figure 2.7: Propeller Forward Advance [8].

The forward motion of the propeller can be characterized by the advance ratio J, which is defined as

$$J = \frac{V_\infty}{nD}$$

where V_∞ is the forward speed of the vehicle, n is the rotational speed, and D is the propeller diameter. Efficient propellers have a small slip.
The propeller efficiency is evaluated as the ratio between the propulsive power produced and the power consumed.

$$\eta = \frac{TV_\infty}{\Omega Q} = \frac{C_T J}{2\pi C_Q}$$

where C_T and C_Q are the thrust and torque coefficients, respectively, defined as

$$C_T = \frac{T}{\rho n^2 D^4}$$

$$C_Q = \frac{Q}{\rho n^2 D^5}$$

Propellers can be classified based on their operation as fixed pitch, pulling, zero thrust, braking, and autorotating (windmilling) types. Each type has specific applications and aerodynamic characteristics. For example, in fixed-pitch propellers, the propeller generates thrust and absorbs power, but its efficiency is zero because the forward speed is zero ($J = 0$ and $\eta = 0$).

Propellers can have either fixed or variable pitch. In fixed pitch propellers, the blade pitch remains constant, so the forward speed of the propeller is determined only by the engine RPM. Maximum efficiency is reached at a specific forward speed. Variable pitch propellers, on the other hand, allow the blade pitch to be adjusted depending on flight conditions and operational requirements.

Chapter 3

Ground effect

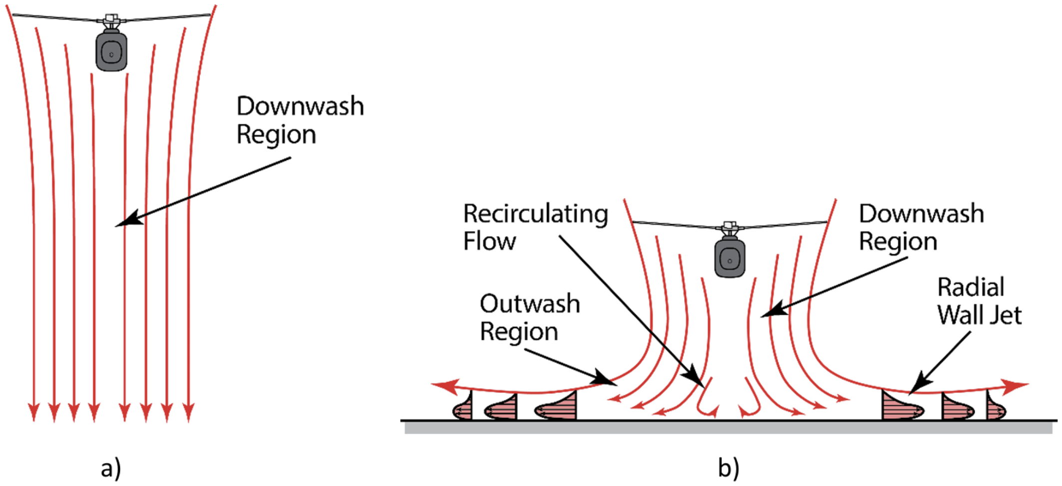

Figure 3.1: Wake visualization out of ground effect (OGE, a) and in ground effect (IGE, b) ref [9].

The ground effect is a phenomenon that affects rotor disks when they are at distances from the ground less than twice the rotor diameter [4], and it is characterized by an increase in lift near the ground (results using Chessman and Bennet show an increase in the ratio T_{IGE}/T_{OGE} between 5% and 15% [1]). This phenomenon has been extensively studied and was well documented in early helicopters, where it was of extreme importance because many of them did not have engines powerful enough for the hovering phase, and the ground effect provided a means to assist during this initial flight phase, even though the characteristics and effects of this phenomenon are still not fully understood [9].

The study of the ground effect, as mentioned in the introduction, plays a crucial role today, since interaction with the ground can cause instability by altering the vehicle's response to specific control inputs. Moreover, maintaining a constant rate of climb or descent becomes more challenging when approaching the ground due to variations in the power ratio. For this reason, it is essential to develop an advanced flight control system that integrates a model-based prediction of the ground effect, also taking into account the influence of obstacles such as walls and ceilings [4].

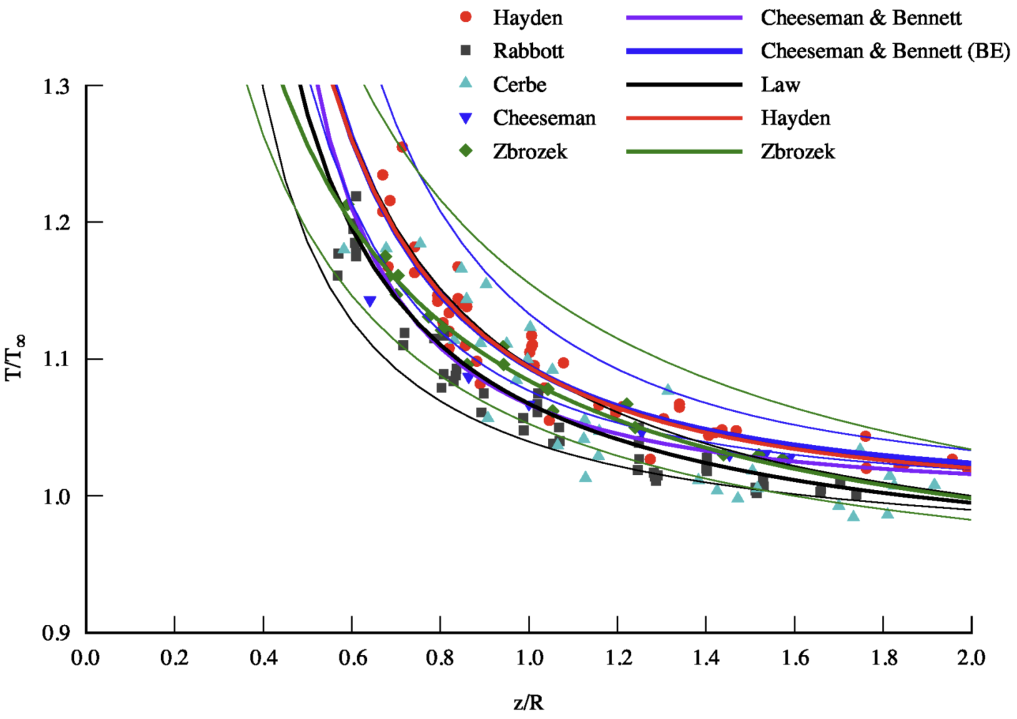

Figure 3.2: Ground effect model from work of Johnson ref [10].

When referring to hovering, this indicates stationary flight in which the vehicle remains fixed relative to the ground. Hovering is sustained by a downward airflow generated by the rotor, which supports the weight of the structure and requires induced power to maintain the downward flow [11]. Furthermore, hovering is a critical flight phase for vehicles such as the Hovera, which are VLoT (Vertical Lift of Takeoff) platforms equipped with rotor disks, enabling them to perform vertical takeoff and landing.

When a vehicle is hovering near the ground, the wake generated by the rotor is forced to expand, transitioning from an initially vertical flow to a radially outward horizontal flow (Outwash), which becomes a jet adhering to the ground (radial wall jet). This results in a modification of both the wake velocity and the induced velocity [4], which decreases and, as will be shown using Blade Element Theory, is inversely proportional to lift. This explains the apparent increase in lift and the reduction in power required to generate the thrust necessary for flight.

The different behavior of the wake is illustrated in Figure 3.1. The left image shows that far from the ground (OGE) the vertical flow is undisturbed and directed downward, exhibiting a normal wake contraction. In contrast, the right image shows the rotor hovering close to the ground (IGE).

It is also observed that in the central part of the wake, near the ground, a recirculation zone forms because the flow is unable to expand radially like the outer regions. This creates a low-pressure area that draws air upward.

Il also known that at low altitudes near the ground, the phenomenon known as Vortex Ring State (VRS) can occur. This flight condition arises during descent, when the downward velocity of the rotors approaches the induced velocity. In VRS, a significant upward recirculation of air develops, causing the aircraft to operate within its own wake, which results in unsteady loads and the performance losses, ref [4].

3.1 Thrust theory

Before analyzing the theories used to evaluate ground effect in detail, it is necessary to introduce the theories that describe thrust generation and its evaluation in a rotor disk. In the literature, a variety of models has been proposed, ranging from the simple actuator disk model to more complex formulations that better represent reality. In this part of the literature review, an approach similar to that adopted by Stephen A. Conyers et al. (see [4] and [12]) is followed.

3.1.1 Actuator disk theory or momentum theory

The first works to estimate the thrust generated by a propeller were those of Rankine in 1865, who developed the actuator disk theory (ADT, also known as momentum theory), which is based on the conservation of mass and momentum. The contribution of Froude from 1878 should also be acknowledged. (What follows is mainly derived from [12]).

This theory is important because it allows a simple estimation of the induced velocity imparted by the propeller to the airflow. The theory is based on the following assumptions:

- The propeller is approximated as a disk of diameter D and infinitesimal thickness, neglecting the resistance of the air passing through it.
- The airflow is accelerated uniformly across the entire disk.
- A control volume surrounding the flow separates it from the surroundings, and the external flow is not affected by the internal flow.
- In the far field, the incoming and outgoing flow from the disk follows parallel trajectories. Consequently, the static pressure of the jet, at a distance from the actuator disk, equals that of the surrounding environment.
- The propeller does not impart rotation to the flow.
- A steady, inviscid, and incompressible flow is assumed.

Essentially, the stationary propeller is situated in a flow moving with a velocity V_∞ upstream, which is then accelerated to a uniform velocity of $V_\infty + \omega$ far downstream of the propeller. The velocity varies continuously to satisfy the law of mass conservation.

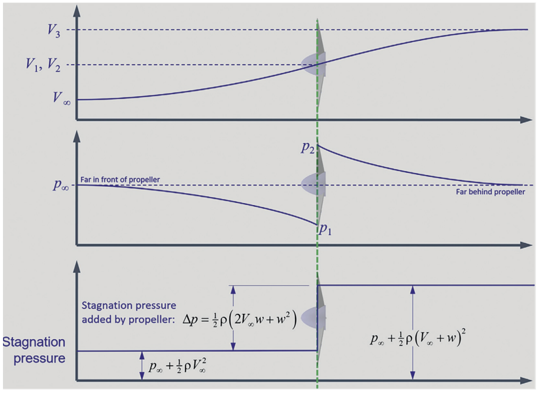

Figure 3.3: Flow properties inside control volume [12].

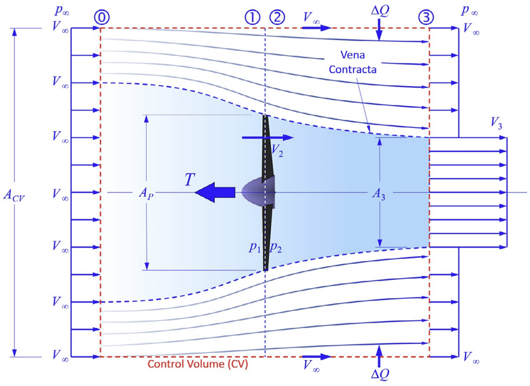

Figure 3.4: Idealized flow model for the Froude–Rankine momentum theory [12].

However, a discontinuous change in pressure occurs due to the presence of the propeller in the flow, which leads to the generation of thrust, figure 3.3.

As can be seen from Figure 3.4, the airflow originates from a control area A_{CV} is larger than that of the rotor disk A_P, and then contracts until reaching a section that is half of A_P (the diameter thus reduces to $\sqrt{1/2} \approx 0.701D$). This particular contraction section is called Vena Contracta, where, according to momentum theory, the flow velocity is twice the induced velocity. Since the mass flow rate must remain constant, the cross sectional area decreases accordingly.

Referring to Figure 3.4, V_2 denotes the velocity through the propeller, while V_3 represents the velocity far downstream.

$$V_2 = V_\infty + \omega \quad V_3 = V_\infty + 2\omega$$

The formulas required to evaluate thrust, power, and propulsive efficiency using this theory are introduced below.
The thrust is given by:

$$T = \dot{m}\omega = 2\rho A_P (V_\infty + \omega)\omega$$

From this, the induced velocity can be derived.
For our studies on the Ground Effect, we will consider $V_\infty = 0$, therefore:

$$\omega = \sqrt{\frac{T}{2\rho A}} = \frac{P_{req}}{T}$$

where P is the required power, given by:

$$P_{req} = T(V_\infty + \omega) = TV_\infty + \frac{T^{1.5}}{\sqrt{2\rho A_P}}$$

and the propulsive efficiency:

$$\eta_{prop} = \frac{Thrust\ Power}{Total\ Power\ required} = \frac{2}{(1 + \frac{V_3}{V_\infty})}$$

Thus, knowing the induced power (P_i) from the propeller motor, it is possible to evaluate the thrust by using the inverse of the definition of P_{req}. In many cases, as in our study, the desired thrust is used as a starting point because it must balance the gravitational force of the structure to hover in the air, therefore:

$$T = mg$$

From this, the induced velocity and the required power can then be evaluated.

Limitations of this theory: This very simple theory, however, has some limitations, including the fact that it does not take into account the geometry of the propeller nor the axial and angular components of the velocity induced by the propeller on the flow.

3.1.2 Momentum theory applicata al duct

The momentum theory can also be used to quantify the thrust contributions of the propeller and the duct under hovering conditions [13].

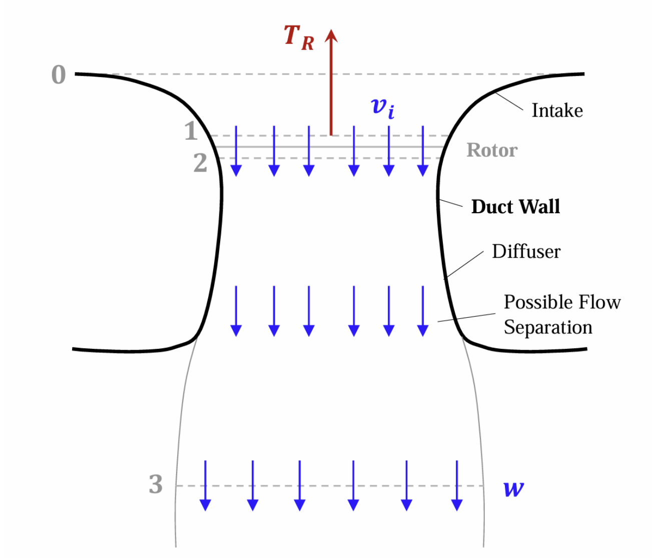

Figure 3.5: Momentum theory model applied to a non-ideal ducted rotor in hover, ref. [13].

Referring to Figure 3.5, and applying the conservation of mass flow rate, we obtain

$$\dot{m} = \rho A_R v_i = \rho A_3 \omega$$

This allows the expression of the area ratio as

$$a = \frac{A_3}{A_R} = \frac{v_i}{\omega}$$

Considering that the flow velocity increases from zero at station 0 to ω at station 3, and taking into account the relationships derived above, we have

$$T_{Total} = T_D + T_R = \dot{m}\omega = \frac{\rho v_i^2 A_R}{a}$$

The rotor thrust T_R can be defined as the pressure difference between stations 2 and 1 multiplied by the rotor area:

$$T_R = (p_2 - p_1) A_R$$

and, applying Bernoulli's equation,

$$p_2 + \frac{1}{2}\rho v_i^2 = p_0 + \frac{1}{2}\rho\omega^2$$

we obtain

$$T_R = (p_2 - p_1) A_R = \frac{1}{2}\rho\omega^2 A_R$$

By dividing the expression for T_R by that for T_{Total} and substituting $v_i = a\omega$, we find

$$\frac{T_R}{T_{Total}} = \frac{1}{2a}$$

Knowing the ratio a, it is then possible to evaluate the thrust contributions. In the case presented in the paper, with $a = 1.15$, this yields

$$T_R = 0.44 \cdot T_{Total}.$$

3.1.3 Blade Element Theory

The study of Blade Element Theory (BET), introduced by Stefan Drzewiecki and developed between 1892 and 1920, is presented. This theory, in addition to the previous one, allows a more detailed description of propeller performance, eventually leading to Blade Element Momentum Theory (BEMT). For the purposes of this work, the focus is first on the simple BET, which will later be combined with momentum theory for the calculation of the induced velocity.

BET consists of dividing the blade into small segments (blade elements) along its length. The underlying assumption is to consider each element as a 2D body and treat it independently. The aerodynamic forces (lift L and drag G) are then evaluated for each segment, and by integrating them along the blade length, the forces acting on the entire system are obtained.
Unlike the Actuator Disk Theory, BET takes into account the geometric characteristics of the blade. Another advantage is the ability to estimate the torque.
We now turn to the mathematical formulation, first defining the expressions to evaluate the aerodynamic quantities and then specifying the meaning of each element mentioned.

As can be seen in Figure 3.6, the rotor blade, of radius R_P and rotating with angular velocity Ω, is divided into numerous infinitesimal segments of length dr, with each segment assigned a value for the local chord $c(r)$. The differential lift dL and drag dD are then:

$$dL = \frac{1}{2}\rho V_E^2 \cdot c(r) \cdot C_l \cdot dr = \frac{1}{2}\rho V_E^2 \Delta S \cdot C_l$$

$$dD = \frac{1}{2}\rho V_E^2 \cdot c(r) \cdot C_d \cdot dr = \frac{1}{2}\rho V_E^2 \Delta S \cdot C_d$$

Where V_E is the effective resultant velocity, and C_l and C_d are the lift and drag coefficients, respectively, which are functions of the angle of attack (AOA) α, as shown in the figure 3.7.

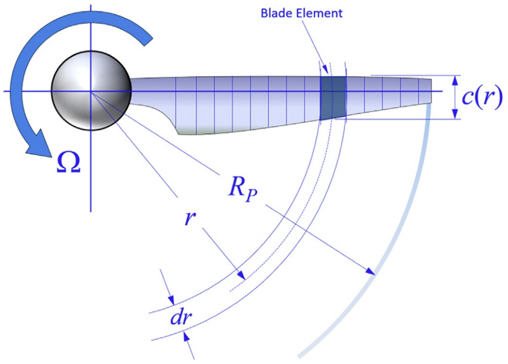

Figure 3.6: BET: Blade Segmentation, ref [12].

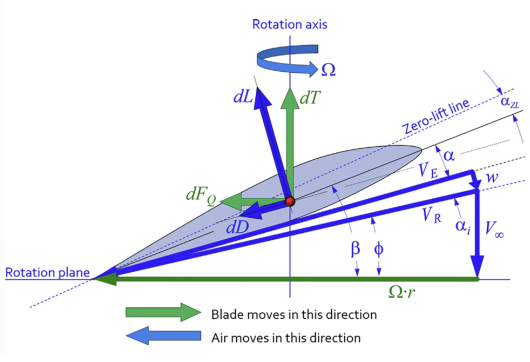

Figure 3.7: BET: Blade Angle Nomenclature, ref [12].

The focus is on the evaluation of thrust (T), torque (Q), and power (P). As shown in Figure 3.7, their differential expressions can be obtained as combinations of the lift and drag calculated above. These terms are then integrated from the hub radius to the tip radius of the rotor, R_P, taking into account the number of blades N_B.

$$dT = dLcos(\phi + \alpha_i) - dDsin(\phi + \alpha_i) \implies T = N_B \int_{R_{hub}}^{R_P} dT$$

$$dQ = rdF_Q = r[dLsin(\phi + \alpha_i) + dDcos(\phi + \alpha_i)] \implies Q = N_B \int_{R_{hub}}^{R_P} r \cdot dF_Q$$

$$dP = \Omega dQ = \Omega r \cdot dF_Q = \Omega r[dLsin(\phi+\alpha_i)+dDcos(\phi+\alpha_i)] \implies P = N_B \int_{R_{hub}}^{R_P} \Omega r dF_Q$$

Where the blade angle is ϕ, the induced angle of attack is α_i, and V_E is the effective velocity.

$$\phi = tan^{-1}\left(\frac{V_\infty}{\Omega r}\right)$$

$$\alpha_i = sin^{-1}\left(\frac{\omega}{\sqrt{V_\infty^2 + (\Omega r)^2}}\right)$$

$$V_E = \sqrt{(V_\infty + \omega)^2 + (\Omega r)^2}$$

The air passing through the flow tube has a higher velocity than that of the far field, which modifies the blade's angle of attack (AOA) and affects the thrust estimates.

Continuing from [12], the ADT and BET are combined to form the Blade Element Momentum Theory (BEMT), which is used to evaluate the induced velocity. The propeller is divided into several circular sections at a distance r from the center, as shown in the Figure 3.8, and the contributions to thrust and torque from each annular element are considered.

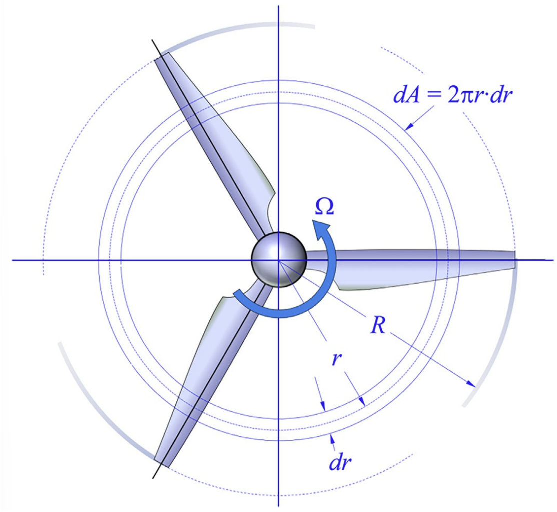

Figure 3.8: BEMT rapresentation of the disk [12].

By adapting the thrust expressions for the annular element, we obtain

$$ADT: \qquad dT = 2\rho(2\pi r \cdot dr)(V_\infty + \omega)\omega$$

$$BET: \quad dT = \frac{N_B}{2}\rho \cdot c(r) \cdot \sqrt{(V_\infty + \omega)^2 + \Omega^2 r^2} \cdot [C_l \cdot (\Omega r) - C_d \cdot (V_{\infty + \omega})] \cdot dr$$

Next, by equating the previously reported thrust expressions, we obtain the following expression as a function of the induced velocity ω

$$f(\omega) = \frac{8\pi r}{N_B \cdot c(r)}\omega - \sqrt{1 + \frac{\Omega^2 r^2}{(V_\infty + \omega)}}[C - l \cdot (\Omega r) - C_d \cdot (V_\infty + \omega)] \cdot dr$$

Starting from an initial value of ω, the expression is iterated until the induced velocity is obtained that satisfies the condition of nullifying the function of ω. Once the value of ω is known, all the necessary quantities to evaluate thrust, torque, and power are available.

This theory allows for the introduction of correction coefficients that account for compressibility effects, which are applied to the lift and thrust formulas, as well as coefficients that consider losses at the hub or at the tip of the propeller.

3.1.4 BEMT

This paragraph follows the BEMT approach by Faisal Mahmuddin in [14], where he also develops a computational method based on BEMT for wind turbine blades. From Momentum Theory, considering that thrust is obtained without rotation, the axial force is

$$dF = 4a(1-a)\rho V_3^2 \pi r dr \qquad a = \frac{V_3 - V_\infty}{V_3}$$

Where V_3 is the velocity far downstream and V_∞ the velocity far upstream, a is the axial induction factor.
Considering also the rotation, the following formula for the thrust is obtained

$$dT = 4a'(1-a)\rho V \Omega \pi r^3 dr \qquad a' = \frac{\omega}{2\Omega}$$

From BET is obtained

$$dF = \frac{1}{2}\rho N_B c V^2 dr[C_l cos\phi + C_d sin\phi]$$

$$dT = \frac{1}{2}\rho N_B c V^2 r dr[C_l sin\phi - C_d cos\phi]$$

where V is the resultant velocity. The BEMT is then obtained by equating the two expressions for F and T and substituting the value of V.

$$\frac{a}{(1-a)} = \frac{\sigma_r}{4}\frac{[C_l cos\phi + C_d sin\phi]}{sin^2\phi}$$

$$\frac{a'}{(1-a')} = \frac{\sigma_r}{4}\frac{[C_l sin\phi - C_d cos\phi]}{sin\phi cos\phi}$$

where σ_r is the local solidity ratio

$$\sigma_r = \frac{N_B c}{2\pi r}$$

3.1.5 Application of BEMT

In [14], a computational method is developed to optimize the design of wind turbine blades starting from a NACA 2415 airfoil. The computational results obtained using BEMT were then compared with those from the QBlade software, showing good agreement between the two.

An interesting study is presented by Z-Dai et al. in [15], where BEMT was adapted for use in the aerodynamic modeling of a coaxial rotor UAV. The theory allowed for the consideration of the interaction between the two rotors; in fact, the interference induced by the lower rotor on the upper one cannot be neglected when they are in close proximity. The model also accounts for tip losses and wake contraction, which are not known a priori. An iterative BEMT method is employed, removing the dependence on empirical constants, using the actual distance between the rotors, and not assuming uniform flow. 2D CFD simulations using ANSYS Fluent were employed to validate the aerodynamic properties of the propeller under study, with the appropriate information on the turbulence model and mesh provided in [15]. To analyze the load distribution in more detail, 3D simulations were also performed, both using the k–ω SST turbulence model. A comparison with experimental data reported in the literature was also conducted to validate the introduced theory. This method, however, presents some limitations; nonetheless, BEMT proved effective, significantly reducing analysis time compared to CFD.

In the section dedicated to the literature on numerical analyses, further examples of BEMT applications will be provided, focusing on ground effect modeling in aircraft.

3.1.6 Vortex Theory

The previous theories were not able to describe how the motion of the propeller influenced the fluid outside the wake. In the early 20th century, Joukowsky and Kutta linked the generation of lift to the presence of vortices, paving the way for the modeling of the flow fields around wings and propellers through vortex systems. This approach overcame the earlier limitation since, by analogy with electromagnetic induction, the effect of a vortex in an ideal fluid extends indefinitely. Moreover, the introduction of vortex theory made it possible to analyze not only time averaged flows, but also instantaneous ones. These are of great importance, because the vortex method has increasingly become an excellent tool for simulating unsteady flows in shorter times compared to CFD.

The description that follow has as sourse the work of W. Z. Skepniewski [16]. The vortex system generated by a propeller consists of bound vortices, attached to the blades and parallel to their longitudinal axis, and free vortices that constitute the wake. The latter include the shed vortices and the trailing vortices, among which the tip vortices dominate the flow field. The collection of free vortices may form a vorticity surface (vortex sheet). If the wake remained invariant in time, the perturbations induced in the fluid could be computed by means of the Biot–Savart law; however, in real fluids it is also necessary to account for the effects of viscosity, which lead to the dissipation of vortices downstream. Some first order corrections can be introduced by suitably modifying the classical Biot–Savart relations.

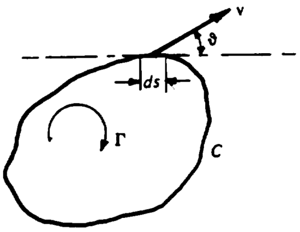

Figure 3.9: Circulation Γ, ref [16].

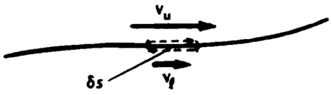

Figure 3.10: Circulation of a vortex sheet, ref [16].

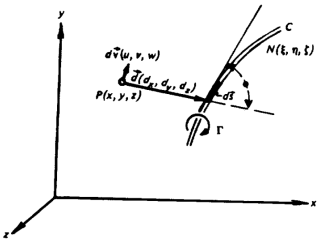

Figure 3.11: Induction of the v velocity, ref [16].

The basic laws of vortex theory concern those related to single vortex filaments and to the vortex surface. The first assumes the fluid to be incompressible, and each vortex filament can be regarded as a small tube rotating about itself. The flow inside the filament can be interpreted as rotational, whereas the flow outside is irrotational. The circulation Γ around the vortex is evaluated as $\Gamma = 2\pi r v_{tg}$, where v_{tg} is the tangential velocity at a point of radius r. More generally, circulation can be expressed as

$$\Gamma = \oint_C v \cdot \cos\theta \cdot ds,$$

see Figure 3.9. When many vortex filaments are very close to each other, they can be considered as forming a vorticity surface (vortex sheet). The circulation per unit length of the surface is defined as $\gamma = \frac{\delta\Gamma}{\delta s}$ and can be computed as the difference between the tangential velocities above and below the surface,

$$\gamma = v_u - v_l,$$

where v_u and v_l are the tangential velocities above and below the vortex sheet, see Figure 3.10. In the case of three dimensional vortices, the Biot–Savart law represents one of the fundamental tools to calculate the velocity field generated by a system of vortex filaments. The total induced velocity $\mathbf{v}$ at a point P by an element belonging to a vortex filament C of intensity Γ is

$$\mathbf{v} = \frac{\Gamma}{4\pi} \oint \frac{d\mathbf{s} \times \mathbf{r}}{|\mathbf{r}|^3} \tag{3.1}$$

According to Prandtl, the velocity $\mathbf{v}$ is obtained by summing the contributions of the infinitesimal filament elements $d\mathbf{s}$, whose effects are perpendicular to both $d\mathbf{s}$ and the vector $\mathbf{r}$, and inversely proportional to the square of the distance r from the considered point. This law is analogous to the Biot–Savart law in electrodynamics, see equation 3.1. An interesting aspect not to be overlooked is that vortices not only induce velocities in the fluid but are also convected by the fluid itself. The classical Biot–Savart law is therefore capable of evaluating both the induced velocity field generated by a system of vortices and the resulting motion of the vortices themselves.

In addition to the Biot–Savart law, the Kutta–Joukowsky law also represents a fundamental principle of vortex theory, as it relates the aerodynamic loads on the blades to the intensity of the bound vortices Γ. The lift L per unit span is given by

$$L = \rho U_\infty \Gamma$$

where U_∞ is the air velocity perpendicular to the vortex filament. Here, Γ is defined as $\Gamma = 2 c_l U_\infty c$, where c is the blade chord and c_l is the lift coefficient. If the circulation along the blade were constant, the bound vortices would be shed only at the blade tips, forming in hover an approximately helical line beneath the rotor. Still under the assumption of constant circulation, it is possible to write a new expression for the circulation that links it to the thrust coefficient C_T:

$$\Gamma_b = \frac{2T}{b\,\rho\,V_{\text{tip}} R} = \frac{2 C_T R V_{\text{tip}}}{b} \tag{3.2}$$

where R is the rotor radius and V_{tip} the tip speed.

Now we proceed in more detail to examine how the expressions for velocity and circulation vary in cases referring to hovering, since the objective is to determine the velocities induced by the wake of a rotor in hover:

Rotor with a single cylindrical wake

It is assumed that the rotor has an infinite number of blades, resulting in a wake filled with vorticity that can be considered as a cylindrical vorticity distribution of radius R.

It can be shown that the induced velocity at a point P is

$$v_p = -\tfrac{1}{2}\frac{d\Gamma}{dy} = \text{const},$$

and that the downwash velocity far below the rotor is

$$v_\infty = -\frac{d\Gamma}{dy}.$$

Using equation (3.2), the total induced velocity becomes

$$v = \sqrt{\frac{T}{2\pi R^2 \rho}}.$$

Variable circulation along the blade surface

In general, it is more realistic to consider that the vorticity of the vortices along the blade radius is variable. However, when a vortex is shed from a given point of the propeller, it does not affect the downwash velocities of the blade elements located further outboard.
The following expression gives the total circulation at a radial position r of the propeller with b blades:

$$\Gamma_r = \tfrac{1}{2} a_r b c_r \left[\theta_r - \left(\tfrac{v_r}{\Omega r}\right)\right] \Omega r$$

where a_r is the sectional lift curve slope, θ_r is the blade pitch angle, and Ω is the angular velocity of the propeller.
As with BEMT, examples of applications of Vortex Theory are also presented in section 4.3.

3.2 Theories for Evaluating Ground Effect

After this introduction to the various methods adopted for thrust calculation, the existing models in the literature are presented to describe and evaluate how proximity to the ground influences propeller performance. The models considered are the Cheeseman-Bennett model, based on the studies of A. Betz from 1937, and the Lighthill model, which employs a modified actuator disk theory.

To allow easy reference to the figures presented in the reviewed articles, different letters are used in the following text to indicate the height above the ground.

3.2.1 Prediction of the Ground Effect with Cheeseman-Bennet

In the paper by Cheeseman-Bennett [17], the method of images is used, where the rotor is replaced by a source (with strength $AV_i/4\pi$) and the ground is represented by introducing another source of the same strength positioned below the rotor. Among the proposed approaches, we are interested in the case where the forward speed is considered zero, allowing the power equation for a helicopter to be written as:

$$(EP - PR)\sqrt{\sigma} = TV_i$$

where the values in parentheses represent the effective power of the rotor. The power is considered constant, therefore:

$$\frac{T_{IGE}}{T_{OGE}} = \frac{V_{i,OGE}}{V_{i,IGE}}$$

It should be noted that IGE refers to in ground effect conditions, while OGE refers to out of ground effect conditions.

Using the method of images, it can be expressed as $V_{i,IGE} = V_i - \delta V_i$. Cheeseman-Bennett assume that the induced velocity V_i of the rotor and the velocity induced at the rotor center by its image, that is, $\delta V_i = \frac{AV_i}{16\pi z^2}$, remain constant. With this assumption, one arrives at:

$$\frac{T_{IGE}}{T_{OGE}} = \frac{1}{1 - \left(\frac{R}{4z}\right)^2} \tag{3.3}$$

where z is the distance from the ground and r is the rotor radius.

In [4], a boundary condition $z/R > 0.25$ is added to this expression, in some cases, it is considered valid above 0.5 due to the size of a manned helicopter fuselage [18].

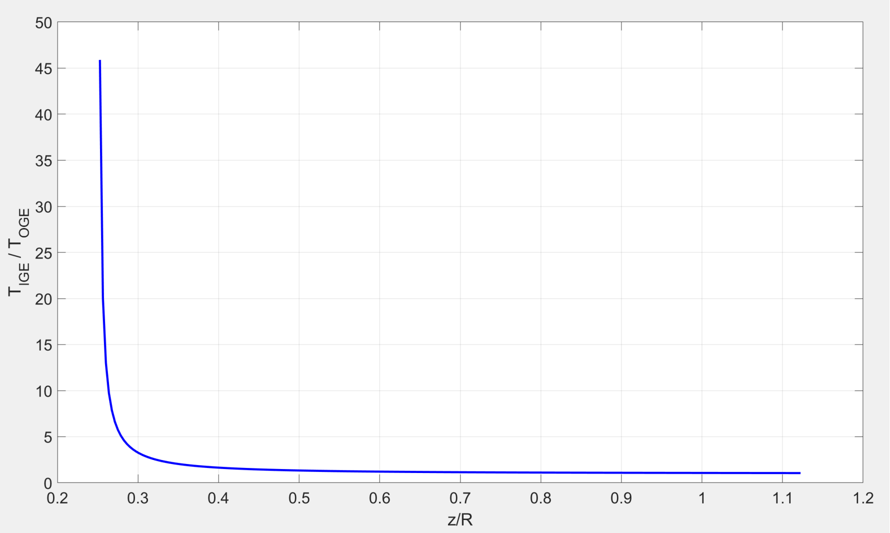

Figure 3.12: Thrust performance in function of z/R, derived from the equation 3.3.

This equation, due to the assumptions made regarding power and velocity, is not accurate when applied to multirotor systems, are valid only for conventional helicopters and do not account for the interactions between the wakes generated by separate rotors. Moreover, Cheeseman-Bennett's theory does not consider the number of blades or the lift distribution, which leads to an overestimation of T_{IGE} for large rotors and an underestimation for smaller scales. An important limitation of this method is that it does not allow the description of what occurs in Extreme Ground Effect (EGE), for $z/R < 0.5$. A similar relation was proposed by Hayden by the all flight test data for different type of helicopters in ground effect, [19], for $z/R > 0.5$:

$$\frac{T_{IGE}}{T_{OGE}} = \frac{1}{A + \left(\frac{2R}{z}\right)^2}$$

con A=0.9926 and B=0.0379.

In many studies using this theory, $T_{IGE} = mg$.
In [4] an alternative expression is proposed that involves power and does not impose the constraints of constant power and velocity, but instead assumes a constant thrust.

$$\Delta HP = \frac{T v_{IGE}}{500}\left[1 - \left(\frac{\omega_{IGE}}{\omega_{OGE}}\right)\right]$$

$$P_{IGE} = P_{OGE} \left(\frac{\omega_{IGE}}{\omega_{OGE}} \right)^2 \tag{3.4}$$

where all the presented quantities can be easily measured or estimated using the theories discussed so far.
s3

3.2.2 Lighthill Theory

Another model for evaluating the ground effect is introduced by J. Lighthill. The goal of [11] is to write a relation similar to (3.4), explicitly defining the induced power coefficient $C_P = P_{IGE}/P_{OGE}$ and expressing it as a function of the ratio z/R.
To achieve this, J. Lighthill started from actuator disk theory, introducing some modifications. The actuator disk is a source of momentum flow but not of mass flow. This implies that the flow must be irrotational and, at large distances from the disk, it assumes the characteristics of a “sink-type” flow directed inward. In this theory, there is an inconsistency (the external fluid must be excluded), which is resolved by introducing an artificial boundary in the form of a vertical cylinder. Inside this cylinder, the flow is bounded by a free stream surface on which the fluid velocity has a constant value U.
The vertical boundary cannot transmit any vertical force to the fluid. In this way, the actuator disk model becomes aerodynamically consistent.

A further simplification is made: the flow is considered two dimensional. The shape of the free streamlines in the two dimensional model is shown for different ratios h/s, where s is the semi-span. This two-dimensional simplification does not affect the absolute value of P/W, defined from the actuator disk theory as:

$$P_i/W = (\frac{W}{2\rho S})^{\frac{1}{2}} \propto \sqrt{W/S}$$

Figure 3.14 shows the experimental points from a test on helicopters by Zbrozek (1950) for different values of the thrust coefficient to solidity ratio: Δ 0.025; x 0.05; O 0.1. At the end of the discussion, J. Lighthill arrives at:

$$C_P = \frac{(c-1)^{\frac{3}{2}}}{c^{\frac{3}{2}} + 2c - 1} \tag{3.5}$$

$$\frac{z}{R} = \frac{1}{\pi} \left\{ \log\left[c^{\frac{1}{2}} + (c-1)^{\frac{1}{2}} \right] + \frac{(c-1)^{\frac{3}{2}}}{c^{\frac{3}{2}} + 2c - 1} \left(\frac{\pi}{2} - \frac{c^{\frac{1}{2}}}{c^{\frac{1}{2}} - 1} \right) \right\} \tag{3.6}$$

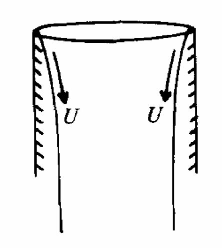

Figure 3.13: An axisymmetric actuator disk model designed to satisfy aerodynamic consistency, ref [11].

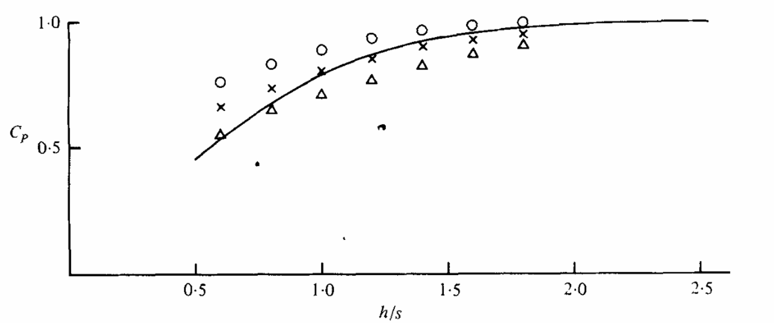

Figure 3.14: Induced power coefficient as a function of h/s, ref [11].

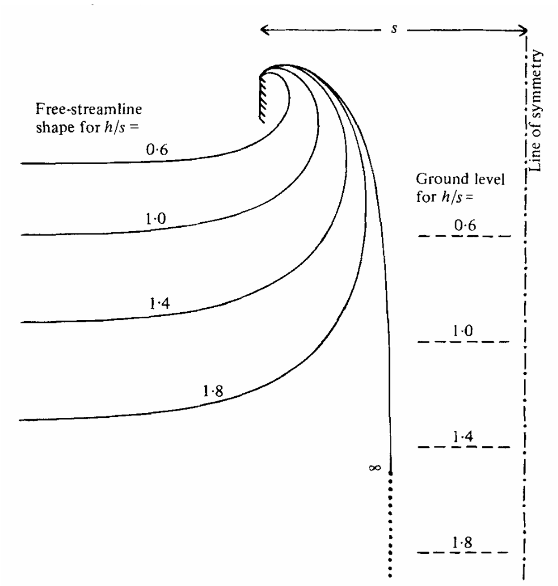

Figure 3.15: Flow representation at different h/s ratios in a 2D model, ref [11].

From (3.6), knowing z/R, it is possible to determine the value of c to substitute into (3.5), thus evaluating the induced power coefficient as a function of the ratio between height above the ground and rotor radius.
By assigning a specific range of z/R, the behavior of C_P can be obtained.

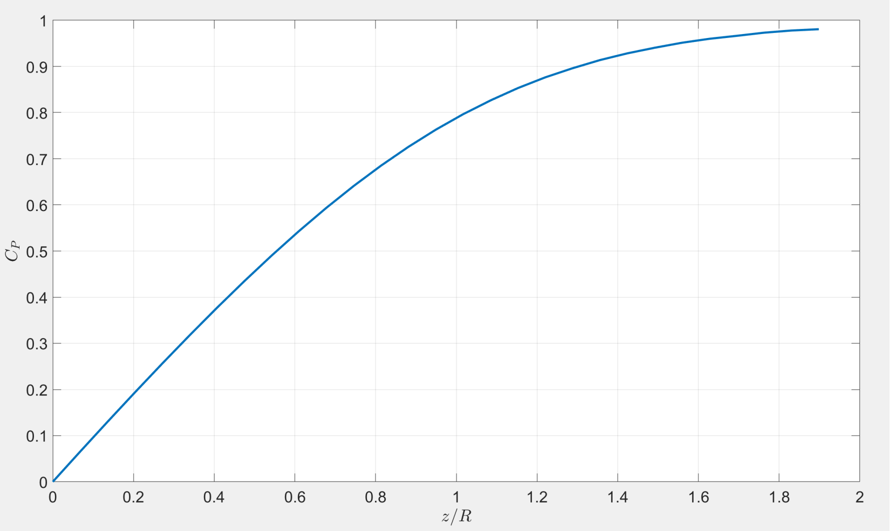

Figure 3.16: C_P in funzione di z/R, obtained by plotting the solution of the system of equations 3.5 and 3.6.

As already mentioned, there are currently no mathematical theories capable of accurately modeling the ground effect. Existing approaches are mostly semi-empirical models, such as the Cheeseman-Bennett model, which is valid only within a limited range and performs well primarily for rotor blades similar to those used in helicopters, with low twist angles. The following sections will therefore focus on reviewing experimental and computational studies on the ground effect.

Chapter 4

Literature Review

In this chapter, a literature review is presented on studies that investigate the ground effect from both experimental and computational perspectives. However, before investigating this phenomenon, attention is first given to the effects that the duct itself has on the propeller in free-air conditions. For this reason, it is essential to conduct a literature review to gain an understanding of these effects, including the potential benefits of using coaxial rotors, which are particularly relevant in the context of the HOVERA project.

4.1 Coaxial and Ducted Propeller Configurations

In aircraft such as conventional helicopters, when a single rotor supports the structure, a yawing moment is generated that makes the vehicle unstable. To address this issue, a tail rotor is added to produce an opposing torque with respect to the main rotor. However, this solution requires between 5% and 20% of the total power [20], without providing useful thrust. By contrast, coaxial counter-rotating rotors inherently achieve torque balance without the need for an additional rotor.

Li et al. [21] conducted experimental tests to investigate how, in a Small Unmanned Aerial Vehicle (SUAV), design parameters such as rotor spacing, rotor position, and tip clearance affect aerodynamic and propulsive performance namely thrust, torque, and power in order to identify the optimal configuration.
These studies were carried out on four different configurations: single rotor, single rotor with duct, coaxial counter-rotating rotors, and coaxial counter-rotating rotors with duct.
To this end, a dedicated test rig was developed, allowing for an easy transition between configurations and for the free adjustment of design parameters.

To evaluate the performance, the following ratios were introduced: the system efficiency, the figure of merit η, and the Power Loading.

$$\eta = \frac{Effective\ Power\ Output}{Input\ Power\ to\ the\ System} = \frac{C_T^{\frac{3}{2}}}{\sqrt{2}C_P} = \frac{T^{\frac{3}{2}}}{P\sqrt{2}\rho A}$$

where C_T is the thrust coefficient and C_P is the power coefficient.

$$PL = \frac{T}{P} = \frac{C_T}{\left(\frac{2\pi}{60}R\Omega\right) C_P} = \frac{30C_T}{\pi R\Omega C_P}$$

From the experimental data, it was observed that coaxial counter-rotating rotors, compared to the single-rotor configuration, provide greater thrust as well as higher specific power (power loading T/P).

In coaxial rotors, it was also observed that the spacing between the two propellers has a significant impact on performance. As will be discussed in more detail in the section dedicated to thrust theories, according to the actuator disk theory, the upper rotor generates a downward jet flow that contracts as it descends and increases in velocity. This accelerated flow interacts with the lower rotor, leading to a reduction in thrust, since the lower rotor operates in an already accelerated flow, unlike the upper rotor which is assumed to be unaffected by the motion of the lower one. This phenomenon is referred to as aerodynamic interference.
In general, aerodynamic interference results in a thrust loss of approximately 14% to 16%, meaning that the total thrust produced by the coaxial counter-rotating rotors is lower than the sum of the thrusts generated individually by the upper and lower rotors. However, a 5.8% increase in propulsive efficiency is observed, due to a partial power recovery made possible by the mutual interaction between the rotors. It was also noted that the thrust contributions of the two rotors at the same rotational speed are not identical. The same applies to the torques generated: overall, the system exhibits a non-zero net torque. This issue can be easily addressed by increasing the rotational speed of the lower rotor, which, does not affect the upper rotor, thereby generating a torque capable of reducing the yawing moment.

Vortices form at the tips of the propellers and tend to remain around the rotor, disturbing the airflow. These are particularly noticeable at low Reynolds numbers, when viscous effects become more pronounced. Such vortices lead to a reduction in the aerodynamic performance of the propeller. The introduction of the duct is crucial here, as it helps reduce tip vortices and minimizes thrust loss.

Xingzhu He et al., cited in [21], conducted CFD studies on coaxial counter-rotating rotors with a duct, demonstrating that the duct leads to an increase in lift.

In the work by Li et al. on the four configurations, a thrust increase of up to 20% was observed when comparing the isolated single rotor case with the single rotor equipped with a duct. The presence of the duct increases the amount of incoming airflow and reduces the contraction of the wake, partially offloading the rotor blades. Moreover, the pressure gradient near the leading edge of the duct contributes to generating additional thrust for the entire system. Additionally, the rotor positions were shown to impact the overall aerodynamic performance. Another factor affecting performance is the gap between the blade tip and the duct, known as tip clearance. The most advantageous clearance is approximately 1.5% of the propeller radius [21].

As mentioned, the duct provides numerous benefits. Furthermore, by adjusting the spacing between the rotors in this configuration, it is possible to identify a spacing that increases the power loading by up to nearly 9% compared to other spacings. For completeness, this optimal spacing corresponds to 25% of the rotor radius (S_1). As can be seen from Figure 4.2, the figure of merit η reaches a maximum of 0.61, representing an increase of about 12% compared to the axial configuration without a duct. This provides further evidence of the efficiency improvement due to the presence of the duct.

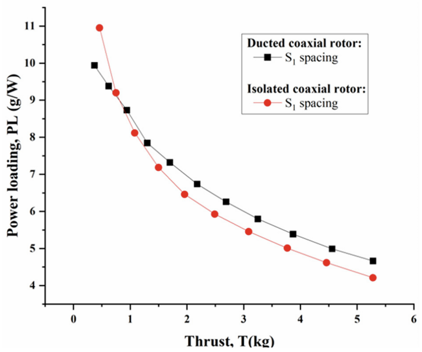

Figure 4.1: Power Loading of Coaxial System with and without Duct, ref [20].

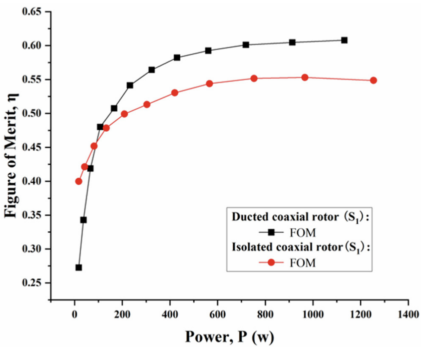

Figure 4.2: Figura of merit η, ref [20].

In addition to the previously mentioned benefits, the duct reduces noise and ensures greater safety in an urban environment, a factor of fundamental importance for this study.

In addition to the experimental study presented so far, CFD analyses were also conducted to investigate the advantages of using a duct. In particular, Jagan Raj R. et al. [22] analyzed the thrust effects produced by a propeller in three different configurations: a single propeller, a single propeller with a rotating duct, and a single propeller with a fixed duct. For the numerical analyses, a TAROT 650 propeller (15 mm × 5.5 mm) was used, tested in free configuration, with a fixed duct, and with a rotating duct, at angular velocities of 2,500 rpm, 4,000 rpm, 5,500 rpm, and 7,000 rpm.

The results indicate that adding a duct around the propeller modifies the tip vortex flow, reducing its intensity and the associated aerodynamic energy losses. By directing the airflow downward and limiting lateral expansion, the duct enhances thrust efficiency through a slight increase in downward air velocity. It was also observed that a fixed duct performs better than a rotating one, as rotation reduces pressure recovery, resulting in slightly lower thrust. For the ducted models, thrust increased by 6.4% in the case of the rotating duct and by 12.9% in the case of the fixed duct, compared to the single-rotor configuration. The numerical results were also experimentally validated, showing a discrepancy of only 2.6%, figure 4.3.

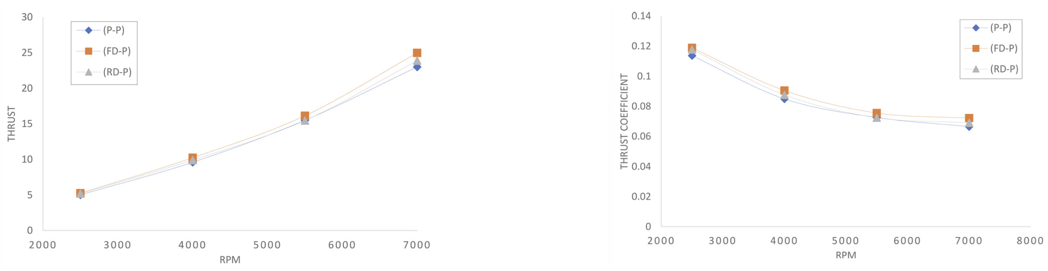

(a) Thrust

(b) Thrust coefficient

Figure 4.3: Trend of Thrust (a) and Thrust Coefficient (b) between the open propeller (P-P), the propeller with fixed duct (FD-P), and the propeller with rotating duct (RD-P), ref [22].

In the paper by Wei Wei et al. [23], the influence of the tip gap and the position of the propeller relative to the rotor on aerodynamic performance is investigated. The study is conducted first through an experimental phase and then via CFD analysis, applying the Response Surface Methodology (RSM) to develop a model capable of predicting the aerodynamic performance of ducted propellers. The rotor under investigation is a 5-bladed rotor with a diameter of 0.8 m, fitted with a duct of 0.25 m chord, tested over a rotational speed range of 1500 to 3000 RPM. The experimental test bench is designed to measure the thrust and torque of the entire system, the isolated rotor, and the duct. In Figure 4.5, the experimental and numerical results are graphically presented, showing the contributions to the thrust provided by each component as a function of RPM.

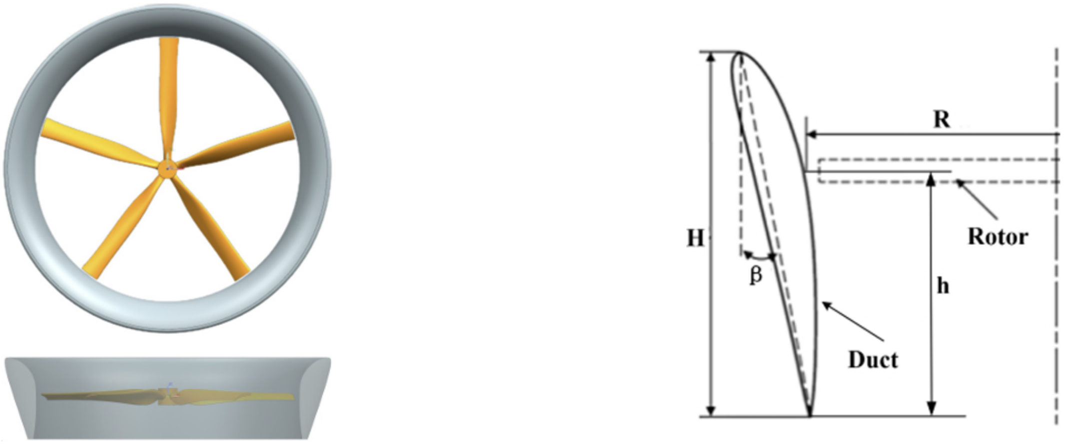

(a) Detail of the duct (b) Ducted propeller

Figure 4.4: Duct–rotor system of [23].

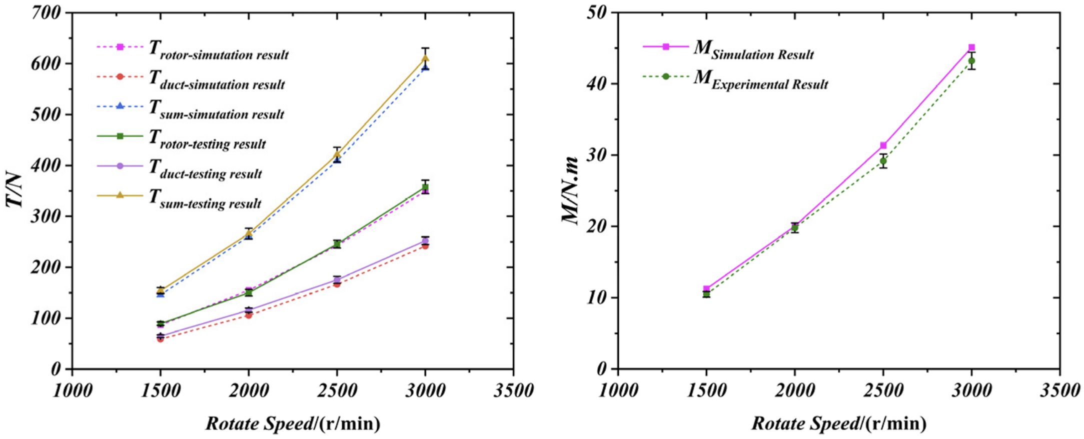

Figure 4.5: Confronto tra risultati sperimentali e numerici ref [23].

Of interest for this thesis work is the comparison between the open propeller and the shrouded rotor, where it can be observed that the addition of the duct leads to a reduction in the propeller's thrust, an increase in the rotor's thrust, and an increase in both the system's thrust and torque. It is concluded in the study that for a tip gap smaller than 3% of the duct's radius, the benefits of the duct outweigh the loss in rotor performance, while above this value the performance deteriorates until it stabilizes for tip gaps greater than 7% of the duct's radius. The rotor's position does not have a significant influence, although it is preferable to place it near the leading edge.

An interesting study is that of Zawodny et al. [13], in which the aerodynamic and acoustic performance of a small four bladed rotor was evaluated with and without a duct. The duct has an inner diameter of 10 inches and a chord of 6.67 inches. The axisymmetric duct was shaped by combining a NACA 0018 airfoil, straight sections, and a geometry suitable for the leading edge, as shown in Figure 4.6.

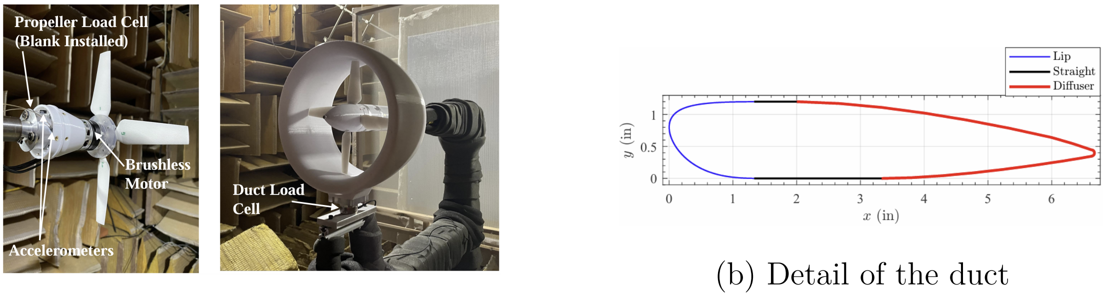

(a) Ducted propeller

(b) Detail of the duct

Figure 4.6: Duct–rotor system of [13].

The work consists of experimental tests on open and ducted propellers, complemented by predictions using the DFDC, ANOPP-PAS, and ANOPP-ROTONET codes. The results obtained by comparing the loads on the isolated propeller and the ducted system in hover are shown in Figure 4.7 as a function of M_{tip}, which can be simply interpreted as different rotation speeds. From the figure, it can be seen that the performance of the open rotor is higher, with the gap between the open propeller (OP) and the shrouded rotor (SR) increasing as the tip speed rises. However, it is also evident that the ducted propeller provides more thrust per unit of power compared to the isolated propeller, as shown in Figure 4.8 (a). Finally, Figure 4.8 (b) shows that the thrust contributions of the propeller and the duct are very similar. This behavior is explained as follows: "the induced flow generated by rotation of the propeller blades yields a pressure differential along the duct surface that results in thrust generation by the duct itself." [13].

Despite the clear advantages of the ducted configuration, it also presents some drawbacks. A poorly designed or geometrically suboptimal duct can reduce these benefits; moreover, for large drones, manufacturing ducts with very tight tolerances can lead to a significant weight increase, partially offsetting the gained advantages. Excessive limitations on propeller diameter can also decrease overall vehicle efficiency, since larger propellers generally tend to be more efficient.

Another important consideration, particularly for high-performance or high-speed drones, concerns potential instability during acrobatic maneuvers: ducts may capture lateral wind flows, causing deviations from the intended trajectory [22].

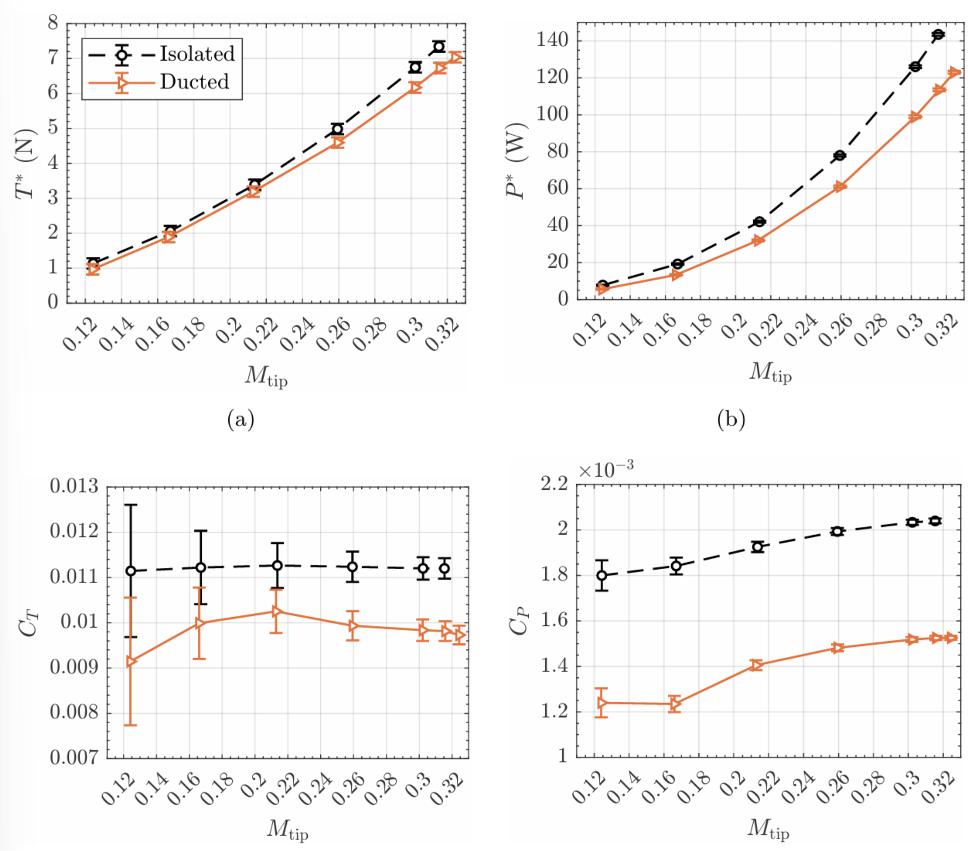

Figure 4.7: Comparison of thrust, power, and coefficients as a function of tip Mach number between open and ducted propellers, ref [13].

Negative interference may also occur between the rotors themselves or between the rotors and the duct, further reducing overall efficiency.

It is important to highlight that, in the context of the present work, it was observed that the duct can generate undesired lift (or downforce) when operating in ground effect, directly influencing the aerodynamic behavior of the drone. This aspect will be further analyzed in the section dedicated to the numerical study of the ground effect [24].

Yilmaz et al. [25] experimentally studied the effect of the duct on the performance of a propeller in hover and axial flight by testing five different NACA duct profiles, including a NACA0018.

The contributions of the various components to the thrust were measured separately to allow better comparison with those of the open propeller. In addition to forces, the velocity field, rotor speed and torque were also measured.

The propeller under investigation is an APC 16×8E operating at 7000 RPM and at various advance ratios.
Only the results for axial flight are reported in the text, and it is observed that the open propeller produces slightly higher thrust than the ducted propeller, although the duct geometry influences its value. However, ducted propellers require less power and achieve higher efficiency for advance ratios lower than 0.3. Results indicate that the thrust produced by the duct originates from the suction effect induced by the propeller in the converging part.

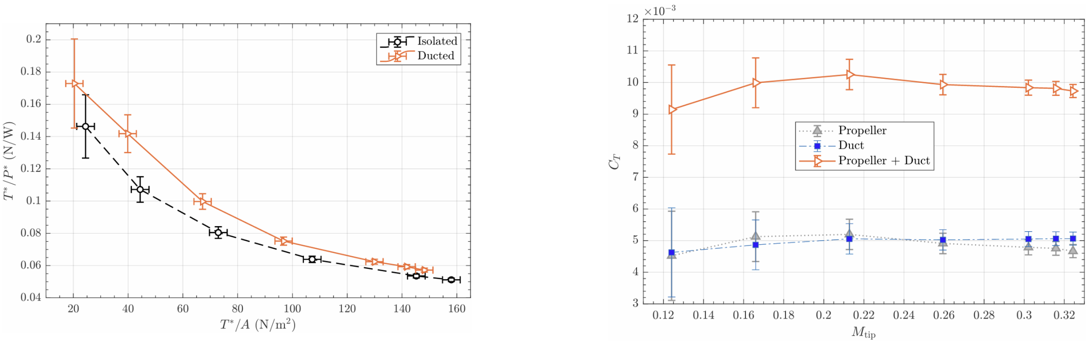

(a) PL with Prop disk Loading

(b) Thrust coefficient

Figure 4.8: (a) Variations of power loading with propulsor disk loading for isolated and ducted propellers (b) Contributions of the duct and propeller to the overall thrust coefficient, ref [13].

Abrego et al. [26] conducted a study on an axially symmetric duct with a diameter of 38 inches, a chord of 10 inches, and a five-bladed fixed-pitch propeller, both in axial and forward flight. Of particular interest from this study is the following observation, which is reported here: "In static conditions, the lift generated by the rotor acts vertically. Air is drawn into the duct and splits at a stagnation point. The cross-section of the duct behaves like an airfoil, where the resulting lift vectors are inclined toward the center of the duct. The vertical components of these vectors provide additional lift to the duct."

Gong et al. [27] conducted a CFD analysis of six propeller configurations, both ducted and non ducted, with different blade numbers, in order to clarify the interactions between blades and duct as well as among the blades themselves. Although the study was carried out in the marine field and the propeller geometry differs from those typically used in drones, it is nevertheless relevant for the present work to examine the considerations made regarding the propeller–duct interaction, as they provide insight into the causes of thrust reduction in ducted propellers. As shown in Figure 4.9, the authors analyzed several configurations with one, two, and four blades, investigating how the addition of a duct, specifically a Wageningen 19A duct, affects the flow characteristics and propeller performance.

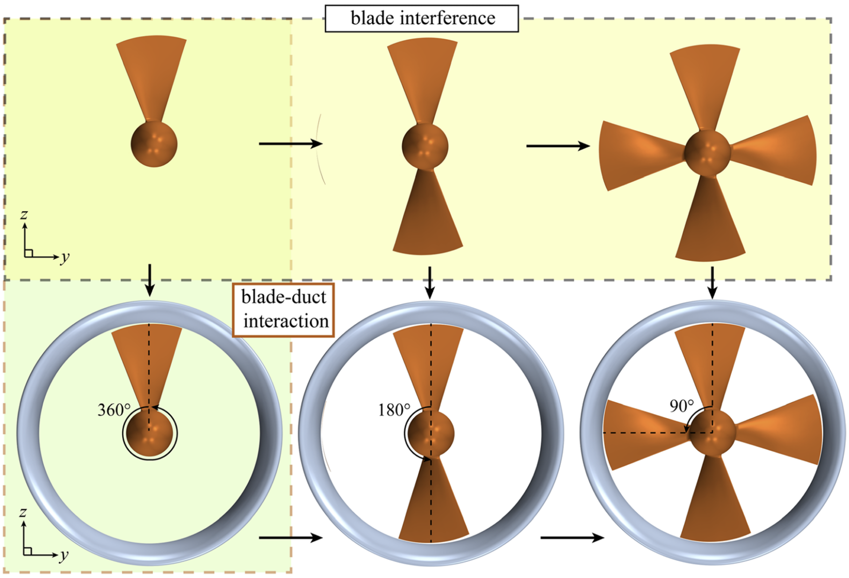

Figure 4.9: Blade and Duct configuration in ref [27].

When multiple blades are present, the flow generated by the upstream blade affects that of the downstream one, altering the angle of attack (AoA). This phenomenon becomes more pronounced when a duct is introduced. In general, a rotating blade generates a helical vortex field composed of tip vortices, root vortices, and a trailing vortex sheet that extends downstream from the blade. The tip vortices consist of two main components: the tip-leakage vortex (TLV), identified by its helical configuration, and the tip-separation vortices (TSV), which are formed due to flow separation beneath the blade tip. As the number of blades increases, the tip vortices interact more strongly with each other. The interaction between the tip vortices and the duct shear layer leads to the formation of secondary vortices, which generate local vorticity fluctuations around the main vortex, adding turbulence and reducing the tip performance. The interaction among these vortices results in greater energy dissipation near the blade tip.

Another study in the naval field that can help in understanding the phenomenon is that of Posa et al. [28]. It presents a CFD analysis using LES of a four-bladed propeller, both with and without a duct (Figure 4.11).
Among the main observations are the high vorticity values in the blade-tip region for the OP compared to the SR (Figure 4.12). In addition, the flow downstream of

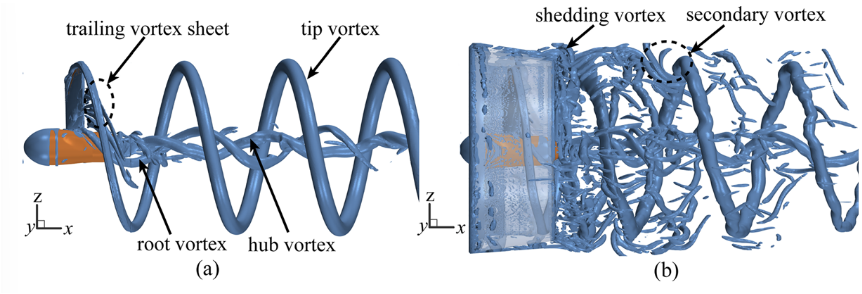

Figure 4.10: Wake vortex structures of one-bladed configuration: (a) non-ducted condition and (b) ducted condition., ref [27].

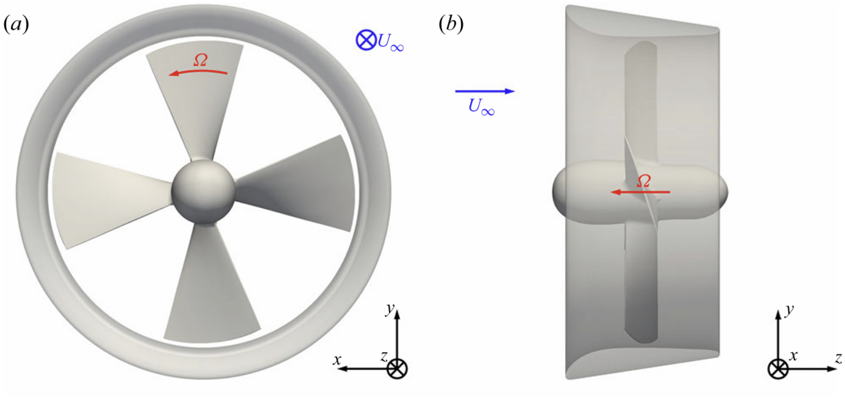

Figure 4.11: Ducted propeller, ref [28].

the shrouded propeller exhibits a lower acceleration than that of the conventional propeller, resulting in reduced velocities along the flow direction in the wake and a less pronounced wake contraction (Figure 4.13).
Overall, a lower loading was observed on the ducted propellers, which can be attributed to the acceleration of the incoming flow induced by the nozzle. Indeed, a faster inflow reduces the effective angles of attack experienced by the propeller, resulting in a lower thrust generation.

For the last two studies analyzed [27] and [28], useful insights were drawn to better understand how the presence of a duct affects propeller performance. However, it should be noted that the naval propellers considered differ significantly from the small propellers studied in this work, so a direct comparison is not always possible.

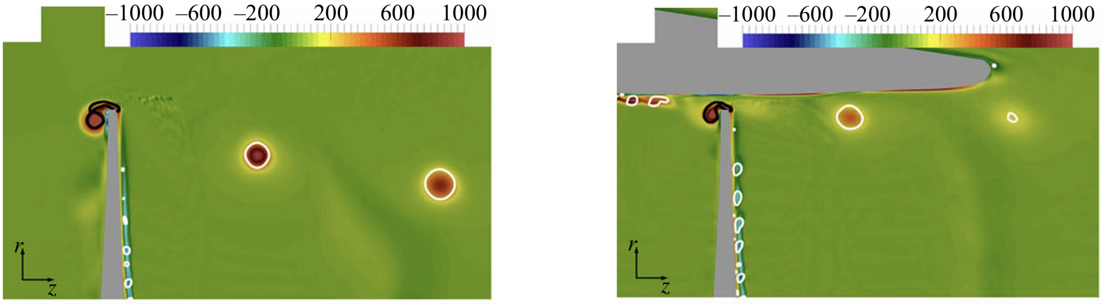

(a) Open propeller

(b) Ducted propeller

Figure 4.12: Comparison of contours of phase-averaged azimuthal vorticity, scaled by U_∞/D for Open propeller (a) and ducted propeller(b), ref [28].

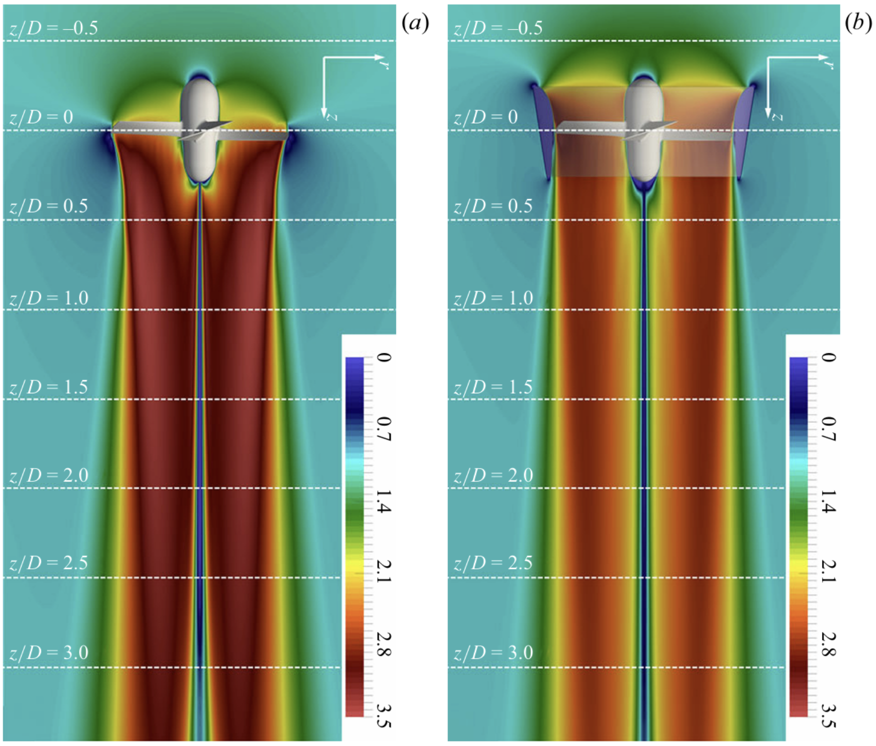

Figure 4.13: Time averaged streamwise velocity contours on a meridian plane, normalized by U_∞, for (a) the ducted propeller and (b) the conventional propeller, ref [28].

4.2 Review of Experimental Work on Ground Effect

In addition to a mathematical approach, the ground effect has been studied in the literature through various experimental tests, such as the one intended to be carried out in the chapter 6. For this reason, it is useful to provide an overview of the findings available in the literature, in order to understand the expected results and to enable a comparison with the outcomes obtained.

G. Georgiev et al. in [1] adapted a test bench, previously used to measure the characteristics of helicopter rotors, to carry out their experimental tests. The test bench is equipped with a foam wall that can be moved to different heights relative to the rotor to simulate the presence of the ground. The setup allows the adjustment of the blade pitch angle and enables the motor to operate at different rotational speeds. The rotor tested is a three-bladed, rectangular, untwisted rotor with a Goettingen 417a airfoil and a diameter of $D = 0.532$ m. Thrust and torque were measured at various rotational speeds (from 750 to 1150 RPM) and at pitch angles ranging from 9° to 21°, repeated at different distances from the ground.
The experimental results showed that thrust increases both with the rotational speed and as the rotor approaches the ground. Torque, on the other hand, also increases with rotational speed but, unlike thrust, it decreases as the distance to the ground is reduced.

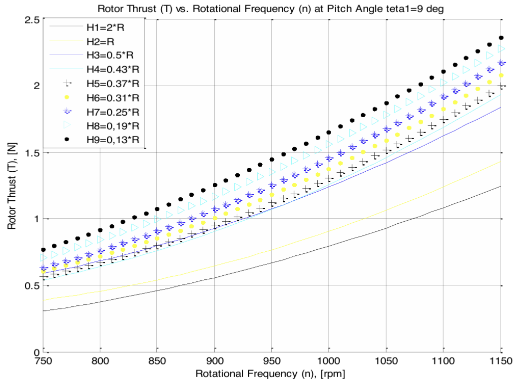

Figure 4.14: Thrust as a function of RPM at different heights above the ground, ref [1].

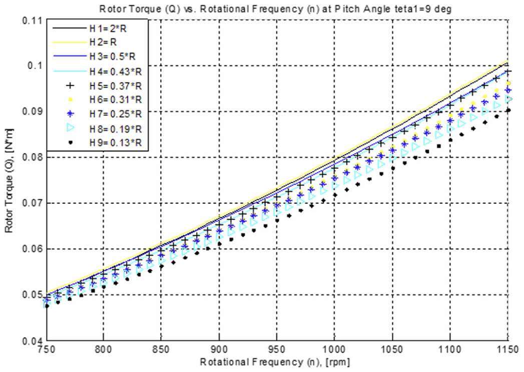

Figure 4.15: Torque as a function of RPM at different heights above the ground, ref [1].

Moreover, it was observed that increasing the blade pitch angle leads to an increase in both thrust and torque. Thrust reaches convergence when the ratio between the distance and the rotor radius is equal to 1, whereas torque stabilizes at a relatively shorter distance. Conversely, the relative thrust coefficient C_{TIGE}/C_{TOGE} exhibits lower values as the pitch angle increases.

In the study by E. Tanner et al. [9], experimental tests were conducted on a transport aircraft equipped with a relatively large rotor, aimed at improving the understanding of rotor outwash in IGE conditions. A four-bladed rotor ($R = 1.69$ m, 1150 RPM) was used, coupled with a generic NASA ROBIN-Mod7 fuselage. The test facility (Rotor Test Cell) allowed simulation of various rotor heights ($0.872 \leq z/R \leq 2.093$) and thrust conditions.
The experimental results confirmed an increase in thrust near the ground. At low rotor heights, maximum outwash velocities reach nearly twice the mean induced velocity ($\sim 2V_h$), while the wall jet develops with higher velocities concentrated near the ground. As the rotor height increases, the high velocity region expands and becomes more diffuse.
For all rotor heights, the lateral outwash velocities are similar at about $0.15R$ above the ground. As the rotor thrust increases, these velocities become higher and spread farther from the rotor. This shows that both rotor height and thrust strongly affect the flow near the ground, which is important for design and operational safety in IGE conditions.

Similar experiments to those proposed in this study were also conducted by D. Chen et al. [29]. The study initially involved the design of an experimental system for force measurement. Subsequently, numerous tests were carried out with rotors of different sizes, varying the hovering height to analyze the aerodynamic characteristics of the rotors and assess the influence of ground effect on their performance. The rotor models used had diameters of 20.3 cm, 25.4 cm, and 28.2 cm, respectively.
Analysis of the experimental results shows that when the rotor is approximately 0.6 times its diameter (H=0.6D) above the ground, the slope of the lift versus height curve is very steep. For heights between 0.6D and about 1.2D, the curve gradually flattens, and for heights greater than 1.2D, the ground effect becomes negligible, confirming theoretical predictions.
Observations using smoke visualization indicate that near the ground, the downward flow generated by the rotor is deflected by the surface, moving both laterally and upward, forming a characteristic fountain like flow beneath the rotor. This upward flow increases the pressure on the rotor's lower surface, contributing to the lift enhancement.

Another interesting experiment is the one conducted by A. Conyers et al. [4] which objective is to demonstrate that it is not possible to accurately evaluate the ground effect using classical theories (Cheeseman-Bennett) developed for conventional rotors when applied to non-conventional ones. Experimental tests were conducted on a quadrotor, demonstrating the accuracy of the experiment after first performing tests on a single-scale rotor. The propellers used are Gemfan 9 × 4.7, and the setup is equipped with force, torque, and speed sensors. The experiments were conducted at different RPMs and by varying the distance between the propellers and the ground. For comparison with theory, Figure 4.16 shows the application of the Cheeseman-Bennett model multiplied by the number of rotors. However, according to actuator disk theory, the flow of each rotor reduces in diameter near the ground and does not merge into a single flow.

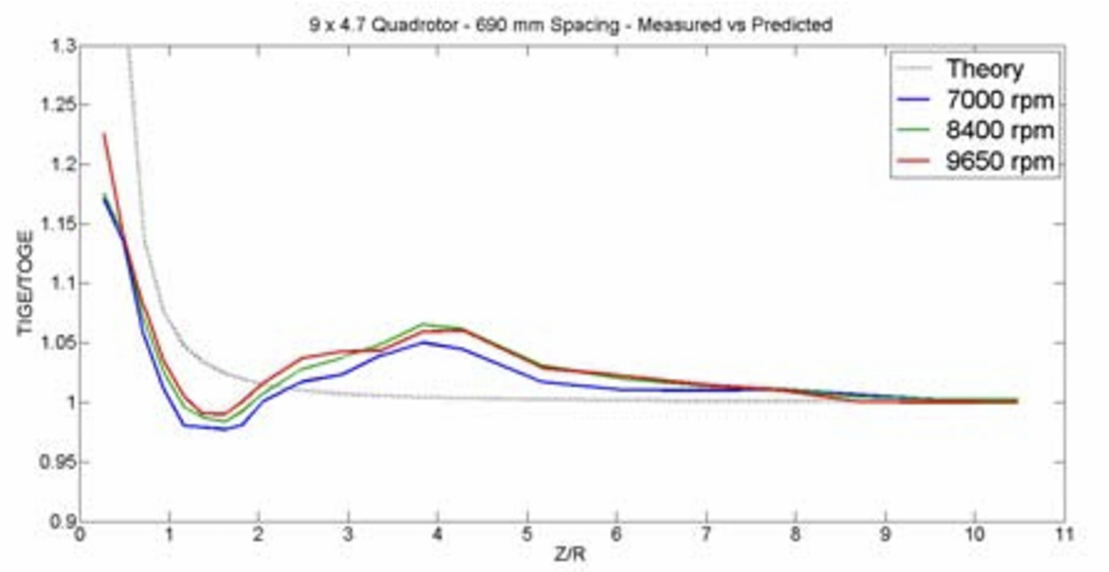

Figure 4.16: Thrust performance curves due to ground effect for 690 mm quadrotor configuration ref [4]

Moreover, an increase in thrust performance is observed not only near the ground but also at $z \approx 4R$, a height at which the ground effect would already be negligible according to Cheeseman-Bennett.

Around $z \approx 1.5 - 2R$, a decrease in thrust is observed, which can be explained by considering the collisions of discrete flows near the ground. When adjacent flows collide, part of the flow is forced to curve away from the surface. This creates a Vortex Ring, which, circulating around the moving rotor, can cause a loss of thrust that cannot be corrected by increasing power; this is known as the Vortex Ring State (VRS).

At higher altitudes, the flow is sufficiently high to recirculate as described, so far

from the ground this issue does not occur.
The authors suggest performing future experiments similar to the one proposed, varying different test parameters to eventually develop a mathematical evaluation of ground effect on multirotors, a prediction that is currently not possible.

One of the objectives of this thesis is to follow the recommendations of A. Conyers et al. on a three-bladed propeller enclosed within a duct, while also attempting to address the gaps concerning phenomena related to Extreme Ground Effect (EGE).

4.3 Litterary review numerical analisys Ground Effect

In the literature, the ground effect has been studied using various numerical simulation methods, ranging from BEMT to CFD analysis.

Application BEMT for ground effect

G.M.Eberhart et al. [18] conducted a study on the ground effect in a small sUAS rotor operating at high angles of attack and low Reynolds numbers, using a modified version of the classical BEMT. As noted in the section on BEMT, this approach was selected here because it is computationally less demanding than traditional CFD methods. The propeller analyzed was a small twisted and tapered APC 11x7 inch propeller, representative of those typically used in multi rotor sUAS.

The article also details the procedure for measuring the required propeller data.

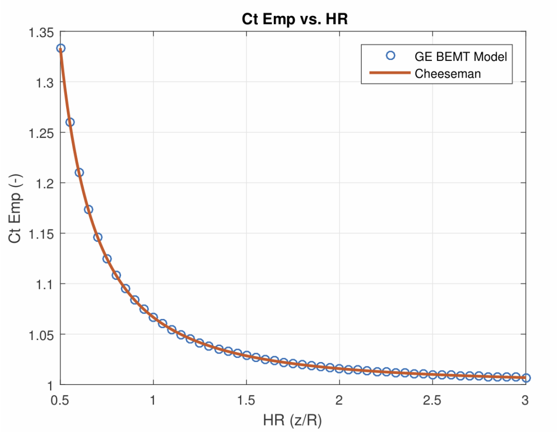

Figure 4.17: Comparison of the thrust ratio from BEMT and Cheeseman for h/R>0.5, ref [30].

The propeller was tested at 5000 RPM and a Reynolds number of 100,000. The thrust results obtained from the BEMT analysis were then compared with Cheeseman's empirical results for $h/R > 0.5$, showing excellent agreement between the two, as illustrated in Figure 4.17. The authors suggest incorporating modifications into the presented model to account for height ratios below 0.5.

The recent work of G. Georgiev [30] introduces the application of a coupled empirical-BEMT algorithm to evaluate the velocity distribution in the rotational plane of a helicopter rotor hovering close to the ground. This algorithm is termed empirical because the inflow ratio distribution (λ) is empirically corrected. In particular, λ is initially evaluated out of ground effect (OGE) at different collective pitch angles and relative distances to the ground (H/R), then used to compute the thrust coefficient (C_T), and subsequently corrected to account for the ground effect. An interesting aspect of this study is that several empirical coefficients, developed in the literature to correct λ, are presented. It was observed, however, that some of these coefficients are accurate only for certain pitch angles (θ) and not for others. In this paper, therefore, the Hayden model is applied for $\theta \leq 18°$ and the Cheeseman-Bennett model for $\theta > 18°$. The choice of coefficients was made by comparing experimental data with the behavior of the relative thrust coefficient (C_{TIGE}/C_{TOGE}) at different H/R values and different θ, all at a fixed rotational speed of 950 RPM for the various models. An example is illustrated in the Figures 4.18 and 4.19.

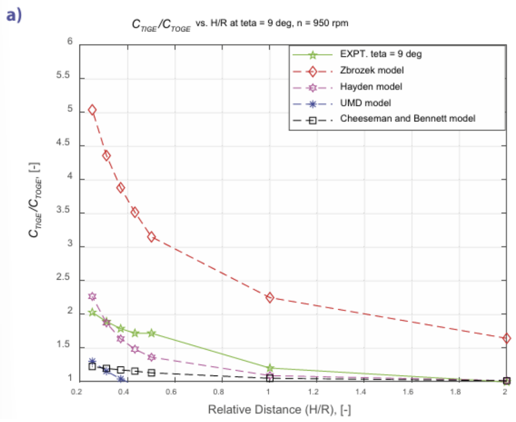

Figure 4.18: Relative thrust coefficient as function of H/R at $RPM = 950$ and $\theta = 9°$, ref [30].

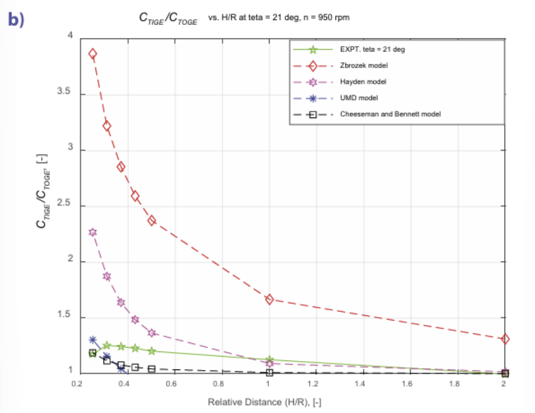

Figure 4.19: Relative thrust coefficient as function of H/R at $RPM = 950$ and $\theta = 21°$, ref [30].

The variation of the inflow ratio (λ) along the blade radius is then presented, both as a function of H/R and of the collective pitch angle (θ), Figure 4.20 and 4.21. It is observed that at a fixed distance from the ground, the inflow ratio (λ) increases with increasing θ, and that decreasing H/R leads to a reduction of λ values at each fixed radial coordinate (r/R).

The evaluation of the normalized thrust coefficient (C_T/σ) was then carried out, showing that decreasing the distance to the ground and increasing θ results in a corresponding increase in generated thrust. The obtained data are in good agreement with experimental results, with a maximum deviation of 5% for pitch angles $\theta > 9°$. The largest deviations occur very close to the ground due to the limited accuracy of the numerical methods in these conditions, where high pitch angles can also lead to stall.

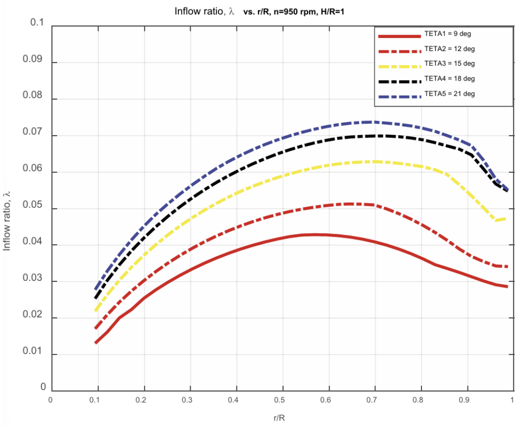

Figure 4.20: Inflow distribution varying the collective pitch angle θ for H/R=1, ref [30].

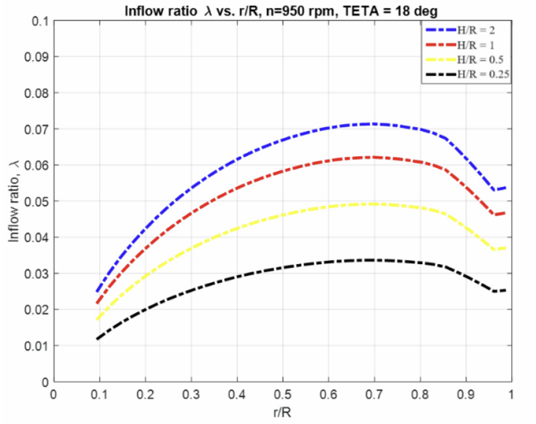

Figure 4.21: Inflow distribution varying the relative distance H/R at $\theta = 18°$, ref [30].

Application vortex theory for ground effect

Some studies on ground effect have been carried out using vortex theory. The first work considered is that of Griffiths et al. in [31], in which the ground effect of helicopter rotors is analyzed using a vortex-singularity-based model. In general, a generic three bladed rotor is employed, except in cases where experimental data were obtained with a specific rotor configuration.

For the wake evolution, the free-vortex model was adopted, with the governing equations solved using both the relaxation and the time-marching approaches.

To simulate ground effect, both the method of images and a surface singularity method are used.

The method of images consists of placing, beneath the rotor under study, an identical and mirrored rotor so that the normal component of the induced velocity between the two is canceled out, thereby simulating the tangency condition of the flow near the ground, Figure 4.22. The advantage of this method lies in its simplicity and low computational cost, since no additional geometries need to be stored, using the same geometry for both the rotor and its mirror.

The surface singularity method consists of placing quadrilateral panels on the ground, with unknown circulation strengths Γ assigned at their edges, Figure 4.23. These circulation strengths are determined by enforcing the flow tangency condition at the ground, Figure 4.22. The computational cost of this method increases with the square of the number of panels, which can make it difficult to implement with limited computing resources. However, it offers the advantage of being highly flexible, allowing for the simulation of finite surfaces of various types.

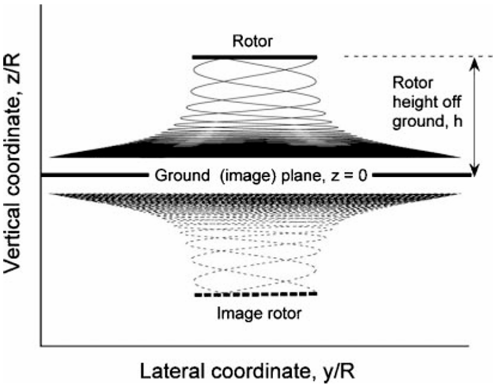

Figure 4.22: Example of rotor in IGE with the method of images, ref. [31].

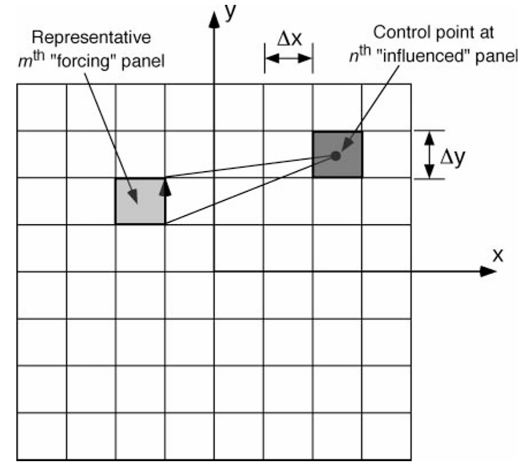

Figure 4.23: Representation of surface singularity panels on the ground plane, ref. [31].

The application of the free-vortex model yields results very similar to those obtained experimentally, making this model reliable for studying IGE. A comparison between the relaxation and time-marching solutions shows that, in many situations, the ground effect phenomenon is inherently aperiodic. Furthermore, the method of images also proved to be reliable for modeling the rotor in IGE, although in this work the ground effect for h/R <0.5 was not investigated.

In this context, the work of Z. Wu et al. in [19] is of particular interest, where both experimental and numerical analyses were conducted in Extreme Ground Effect (EGE), that is, for distances from the ground less than half of the rotor radius. To experimentally investigate the flow in the near ground region, the PIV technique was employed, while the numerical analysis was carried out using the Detached Eddy Simulation (DES) method.
The rotor under study is a two bladed rotor with a radius of 560 mm and a rotational speed ranging approximately from 21 to 262 RPM. The paper provides a detailed description of the experimental setup, which can be integrated with the setups presented in the previous section.
Regarding the simulation, the CFD analysis was performed using ANSYS FLUENT, employing a DES model that incorporates both RANS, with the SST $k - \omega$ turbulence model, and LES. Additionally, the Improved Delayed DES (IDDES) formulation by Shur et al. was used to address certain numerical challenges.

To provide a further estimation of the wake at a lower computational cost compared to DES, the Prescribed Wake Model (PWM) was employed, which has proven capable of accurately predicting the tip vortex trajectories in EGE.
The comparison between experimental and CFD results showed that, except at low rotational speeds, the deviations remain within a relative error of 10% (see Figure 4.24).

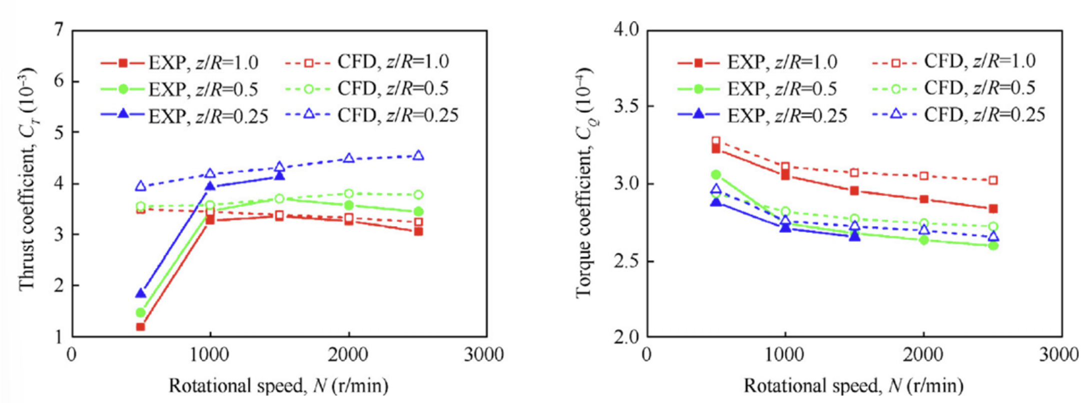

Figure 4.24: Comparison of rotor thrust (C_T) and torque (C_Q) coefficients obtained from experimental measurements and CFD simulations, ref [19].

Figure 4.25 shows the visualization of the rotor wake at a rotational speed of 200 r/min for different heights above the ground. It can be observed that, as z/R decreases, the intensity of the tip vortices increases and the boundary layer between the tip vortices and the ground becomes thinner. It is worth noting that tip vortices are vortices shed from the rotor blade tips and move away from them.

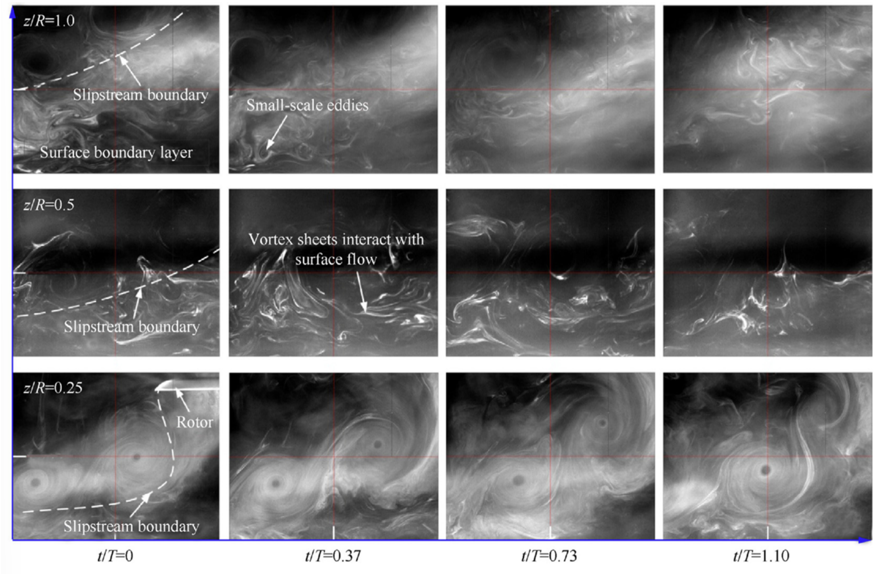

Figure 4.25: Visualization of the rotor wake at various rotor heights above the ground at N = 200 r/min, ref [19].

The wall jet flow under EGE conditions exhibits clearly distinct characteristics compared to the IGE case, with the flow separation near the ground being the most notable difference, Figure 4.26.

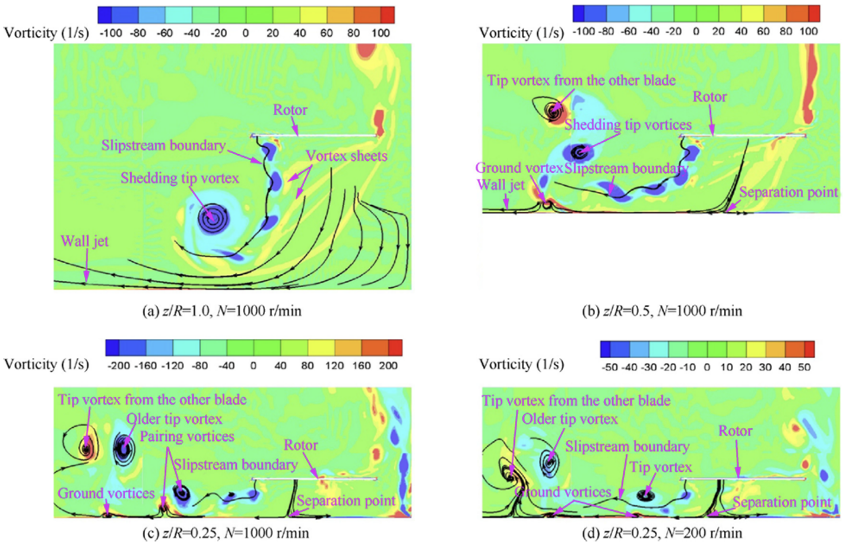

Figure 4.26: Computational visualization of the interaction between the rotor wake flow and the ground using vorticity and streamlines [19].

M.P. Kinzel et al. in [32] focused on the study of descent and ground effect in coaxial rotors, with particular attention to the vortex ring state (VRS) during descent and how the presence of coaxial rotors can mitigate this phenomenon, which is detrimental to the aircraft. The study was conducted using CFD analysis. The geometries considered in this work are two: a pair of counter rotating rotors, and a single four bladed rotor, both featuring a radial twist of 14.78°. The analysis was carried out under Titan's atmospheric conditions (a moon of Saturn), using an incompressible and turbulent flow model, with rotor rotational speeds ranging from 500 to 600 RPM. The simulations were performed using STAR-CCM+, employing a Reynolds Averaged Navier-Stokes (RANS) solver with the Spalart-Allmaras (SA) turbulence model. In the simulations, two types of approaches integrated with CFD to reduce computational cost are discussed: the Blade Element Method (BEM) and the Mixing Plane Model (MPM). The latter is a model that uses multiple reference frames, one for the rotating parts and one for the stationary parts, and applies a mixing plane condition at the interfaces, which results in an azimuthal averaging while conserving the flow of each quantity. The type of mesh used for each method and case study is described in detail. In general, the hub boundary layers are captured with sufficient resolution. For the rotor blades and wake, the mesh is generated differently depending on the specific scenario. The grid used to simulate ground effect is finer compared to the out of ground effect (OGE) meshes, with a minimum of 25 million cells for the MPM model, in order to resolve the rotor vortex down to the ground, figure 4.27. However, the vortical wake is not averaged.

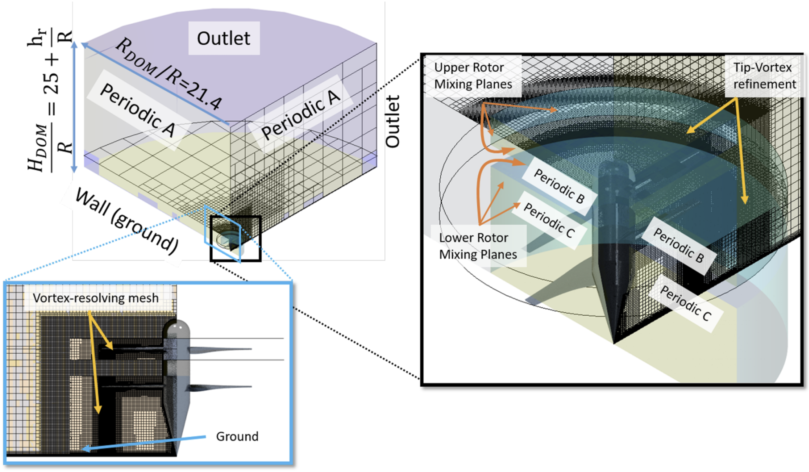

Figure 4.27: Mesh for the MPM applied for ground effect, ref [32].

For descent, simulations were performed on both single and coaxial rotors, and results suggest that in counter rotating coaxial configurations the onset of VRS is delayed. The evaluation employed both the BEM and MPM approaches, with the authors noting that rotor descent remains a phenomenon requiring more detailed investigation. In the case of counter rotating rotors operating in ground effect, only the MPM method was applied, proving to be effective.

4.3.1 Additional studies with more focus on ground effect with the duct

Y. Zhao et al. in [24] studied the aerodynamic characteristics of a ducted fan for VLOT aircraft in hovering and in ground effect through CFD analysis. The authors focused on this problem since many V/STOL vehicles have been observed to experience adverse ground effect during take-off and landing. The ducted fan considered in the study has 8 blades with a diameter of 0.646 m and a pitch angle of 39° at three-quarters of the radius. It generates up to 84 kgf of static thrust at 3500 RPM and represents a 5/8 scale model of one mounted on an eVLOT aircraft of up to 3000 kg.
To simulate fan rotation, the Multi Reference Frame (MRF) method was used together with a Realizable $k-\epsilon$ turbulence model. The numerical method was first validated on a configuration with available experimental data, by comparing the results and verifying that discrepancies were reduced, also using the more accurate sliding mesh method.
The authors note that, at the time of publication (2022), no experimental data on the ground effect of ducted fans were available to validate numerical methods, due to the difficulty of precisely replicating the geometric models employed in experiments.

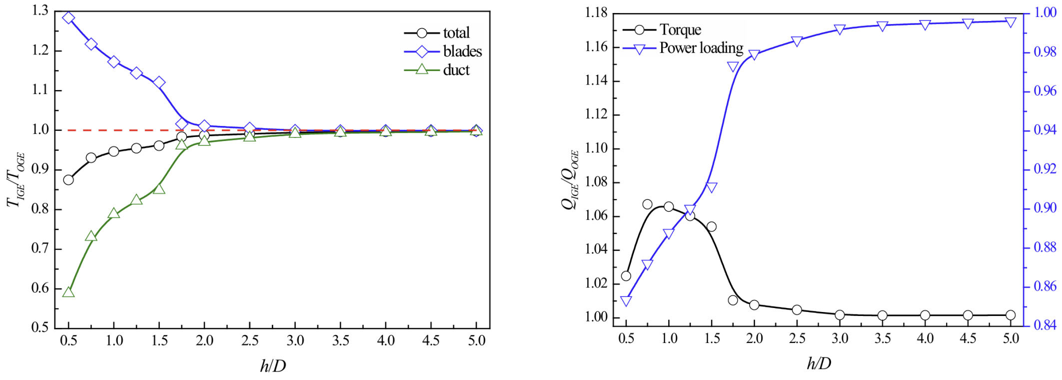

(a) **(b)**

Figure 4.28: Changes in ducted fan performance with height: comparison of (a) thrust ratios and (b) torque and power loading ratios, ref [24].

It was observed (Figure 4.28) that, when the ducted fan operates close to the ground, the thrust produced by the blades increases, while the thrust from the duct decreases compared to the hovering condition. This behavior is caused by the increased internal surface area of the duct, particularly near the lip. The effects become negligible for $h > 3D$ and significant for $h < 1.5D$. At a height of 0.5D, an overall reduction in total thrust of 12.5% and a decrease in power loading of 14.6% are observed due to ground effect. As shown in Figure 4.29, as the ducted fan approaches the ground, the pressure at the bottom increases, and this, combined with the increment in the effective angle of attack, leads to a higher blade thrust.

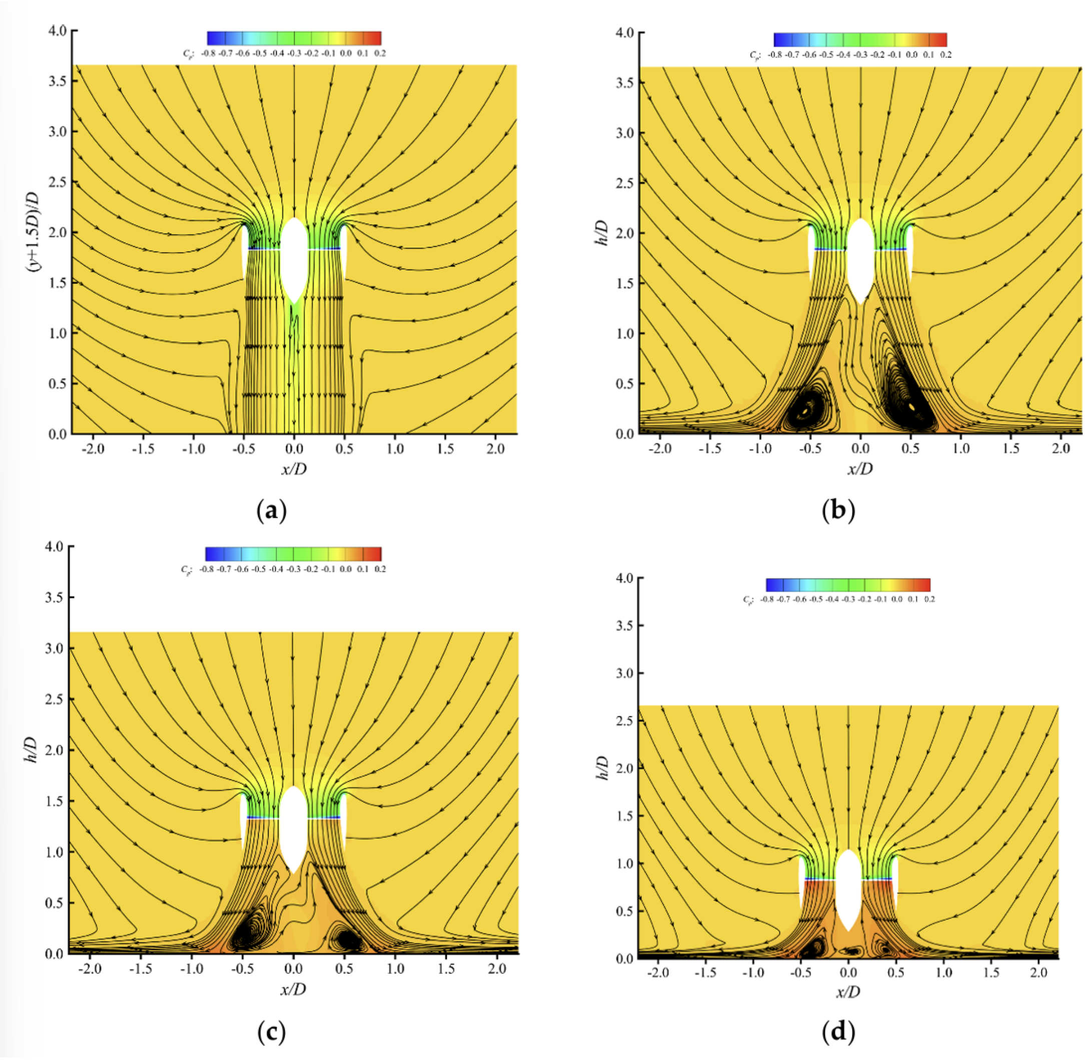

(a) (b) (c) (d)

Figure 4.29: Pressure coefficient in a) OGE; b) h/D=1.5; c) h/D=1.0; d) h/D=0.5, ref [24].

The study then analyzed the aerodynamic characteristics of the ducted fan during transition in ground effect, considering different advance ratios J and angles of attack α. It was observed that stall is delayed in ground effect for certain advance ratios. Furthermore, the different positions and influence regions of the ground vortex at varying advance ratios lead to different trends in the performance of the ducted fan, making the aerodynamic analysis more complex.

The work of Han et al. [33] focused on investigating the ground effect for shrouded rotors both from an experimental and a numerical point of view using ANSYS/FLUENT CFD.
The rotor used is a 5-blade rotor with a radius of 0.165 m, surrounded by a shroud designed based on a CLARK Y airfoil, as shown in Figure 4.30. The system is equipped with two load cells, one for the propeller and the other for the shroud, in order to measure the loads separately.

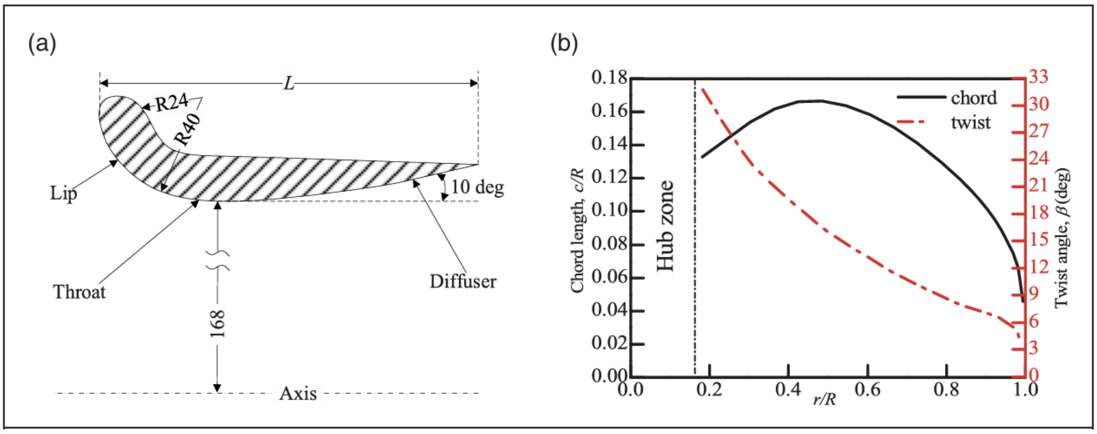

Figure 4.30: Duct and rotor details: (a) Duct configuration scheme; (b) Chord and twist distribution of the propeller blade, ref [33].

The numerical simulations were carried out using an MRF model, with a rotating domain around the ducted propeller and a fixed external cubic domain with a side length of 20R. The SST $k-\omega$ model was chosen for turbulence, and simulations were performed for rotational speeds ranging from 3,000 to 6,000 RPM.

The experimental test results showed that both the open rotor and the shrouded rotor experience an increase in thrust near the ground, with the latter being more sensitive, as shown in Figure 4.31 (a). The IGE conditions for the SR start at $h/R < 1.5$, whereas for the OP they start at $h/R < 2.2$, which is also evident in Figure 4.31 (b), where the ratio T_{SR}/T_{OP} begins to increase for $h/R < 1.5$. Figure

4.32 illustrates how the various performance coefficients behave as a function of rotational speed for different h/R values.

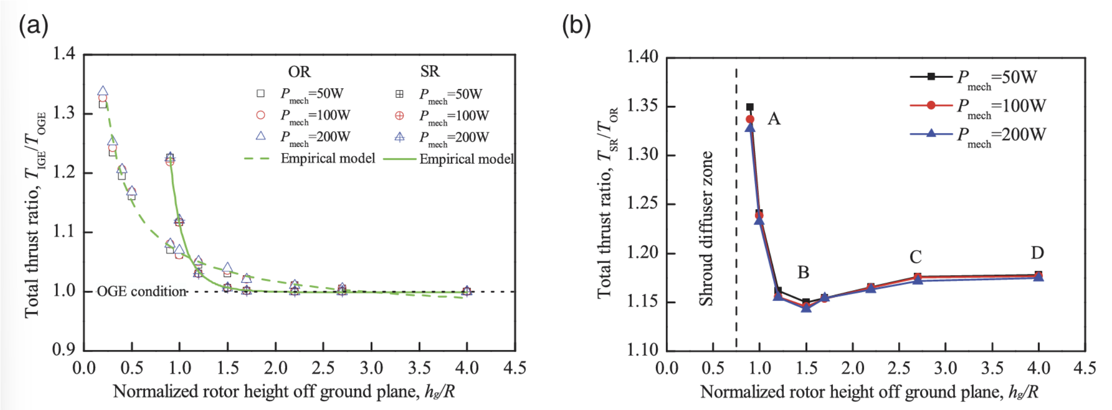

Figure 4.31: Experimental results at three power values (a) Total thrust ratio of IGE to OGE, (b) Total thrust ratio of SR to OR, ref [33].

Moving on to the numerical results, it is reported that for the OR at $h/R = 0.2$, the rotor thrust in IGE increases by 40% and the torque by 13%. For the SR at $h/R = 0.9$, the total thrust increases by 33.5% and the torque by 21.8%.
And from Figure 4.33, it can be observed that the wake formed beneath the blades for the SR is larger than that of the OP, where lower velocities are also present. This leads to higher static pressure and, consequently, an improvement in aerodynamic efficiency.

LUO et al. [34] focused their attention on the unsteady characteristics of a ducted fan in ground effect, which was studied through CFD analysis using Ansys and validated experimentally.
The propeller used is a three-bladed propeller with a diameter of 206 mm and a pitch ranging from 40.63° at the hub to 20.35° at the tip, values very similar to those of the APC propeller considered in this thesis. The duct is designed to provide a tip clearance of 0.91 mm, with an outer diameter of 292 mm and a length of 50 mm. The duct and the blade geometric parameters are shown in Figure 4.34. For the CFD simulations, the domain was divided into a fixed and a rotating part; in the latter region, the mesh was generated using NUMECA AutoGrid5, ensuring a high grid accuracy. For the stationary simulations, the MRF method was employed, while for those in ground effect the sliding mesh technique was used. The simulations were performed at a rotational speed of 4000 RPM for the height ratios h/R = 0.2, 0.3, 0.5, 0.8, 1.0, 1.5, 2.0, 3.0, 4.0, 5.0, using the SST $k - \omega$ turbulence model. Overall, the results shown in Figure 4.35 confirm the findings of [24]: the propeller thrust increases as the fan approaches the ground, the duct

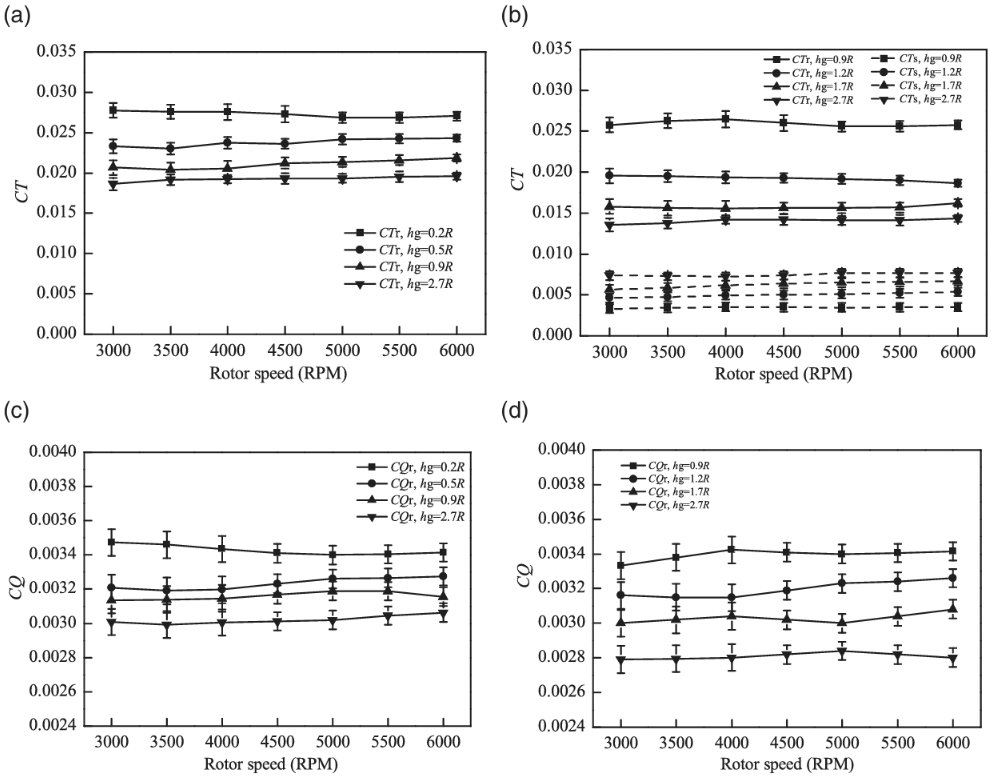

Figure 4.32: Experimental results(a) Rotor thrust coefficient C_T versus RPM for OR, (b) Rotor thrust coefficient C_T versus RPM for SR, (c) Rotor torque coefficient C_Q versus RPM for OR, (d) Rotor torque coefficient C_Q versus RPM for SR, ref [33].

thrust decreases, as well as the total system thrust. On the right side of the figure, the standard deviations for the different heights above the ground are also reported, showing that they increase as the height decreases. For instance, for h/R = 0.2, the fluctuations are 17% for the rotor, 89% for the duct, and 37% for the total. The effects of the duct at different rotational speeds also confirm the results of [23]: the thrust becomes higher as the RPM rises, while the fluctuations of the duct remain smaller than those of the rotor. The authors also introduced an empirical formula to describe the behavior of the T_{IGE}/T_{OGE} ratio for the entire system

$$\frac{T_{IGE}}{T_{OGE}} = -2.346 \cdot exp\left(-8.155\frac{h}{R}\right) + 0.9821, \quad R^2 = 0.9926 \tag{4.1}$$

In general, the ground effect for a ducted propeller can extend up to h/R = 4, which is higher than the typical h/R = 2 observed for helicopters.

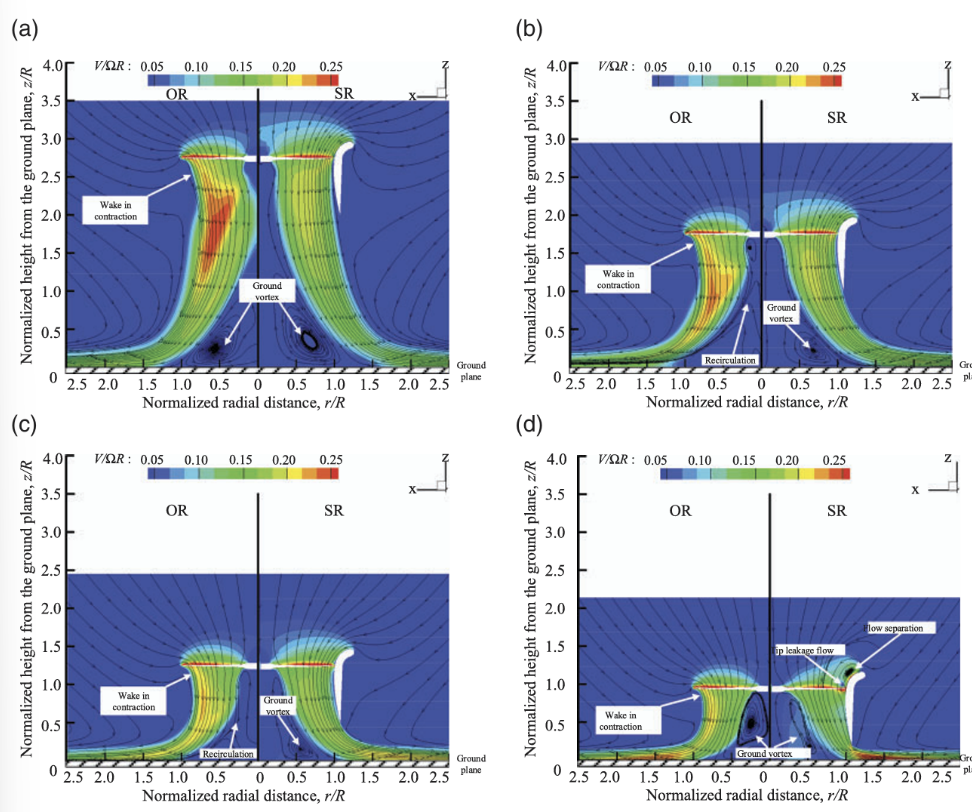

Figure 4.33: Numerical results: time-averaged velocity distributions close to the ground plane for various rotor to ground heights. (a) r/R = 0.8; (b) r/R = 1.0; (c) r/R = 1.25; (d) r/R = 1.5; (e) r/R = 1.75; (f) r/R = 2.0, ref [33].

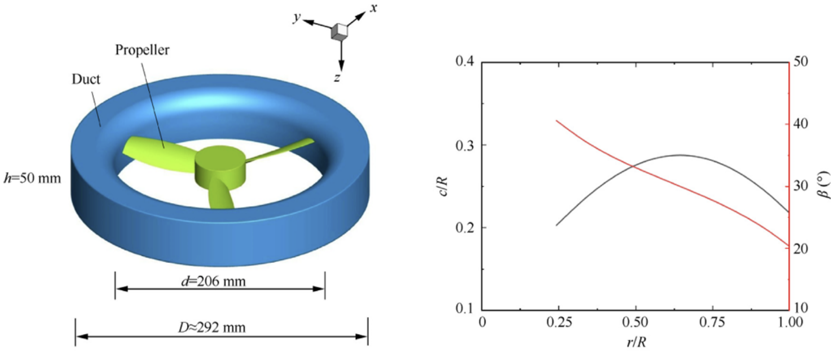

(a) Ducted fan

(b) Blade parameters

Figure 4.34: Ducted fan (a) and geometric parameters of the blade (b), ref [34].

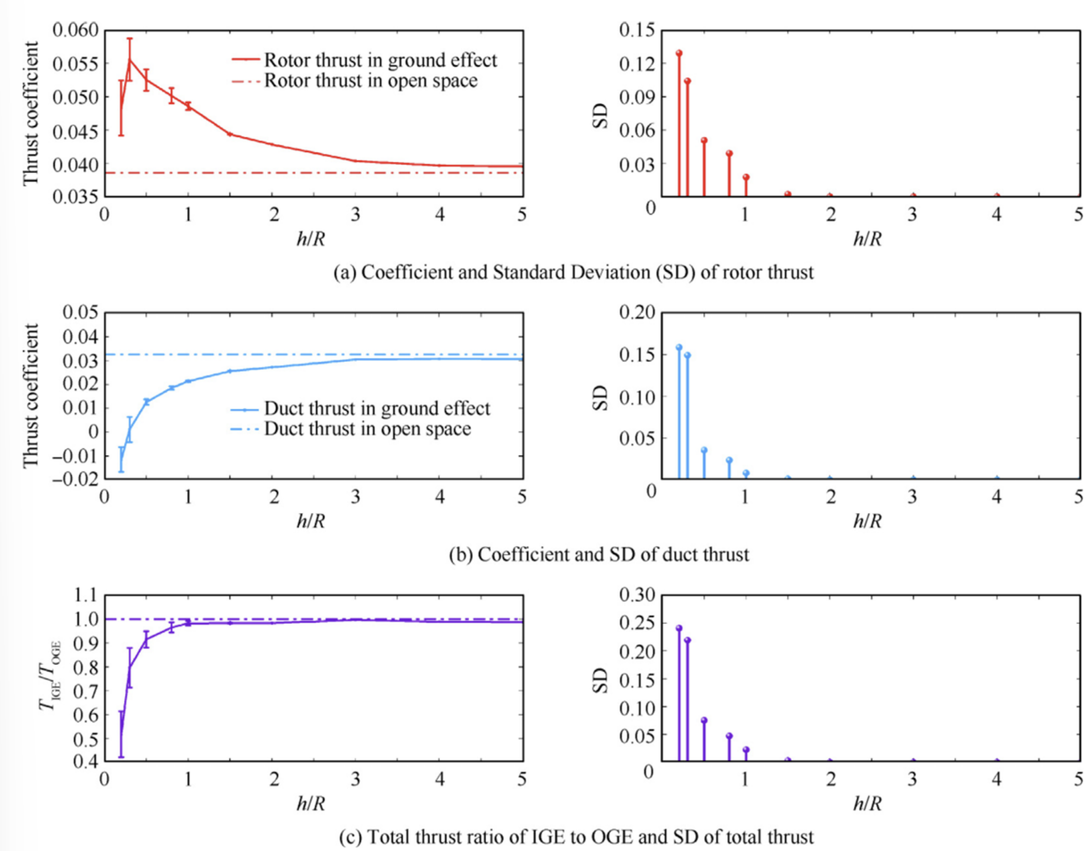

(a) Coefficient and Standard Deviation (SD) of rotor thrust

(b) Coefficient and SD of duct thrust

(c) Total thrust ratio of IGE to OGE and SD of total thrust

Figure 4.35: Variation of ducted fan thrust with ground clearance and corresponding standard deviations near the ground, ref [34].

The thrust fluctuations are caused by the fact that, as the fan approaches the ground, the downward flow is forced to deviate laterally, generating a low pressure region along the inner wall of the duct. At the same time, in the central region, the portion of the flow that cannot exit recirculates in an unsteady manner, contributing to the overall thrust instability.
The increase in propeller thrust is due to the rise in the angle of attack as the fan nears the ground, caused by the lateral displacement of the air.
Particularly interesting is the study of the pressure coefficient along the duct to explain the thrust reduction at lower heights. Figure 4.36 shows that, as the fan gets closer to the ground, the pressure in the C-D section becomes lower than in the B-C section, where the flow decelerates. This effect leads to a reduction of the duct thrust, which can even become negative at very low heights. Conversely, no significant variations were observed for the torque.

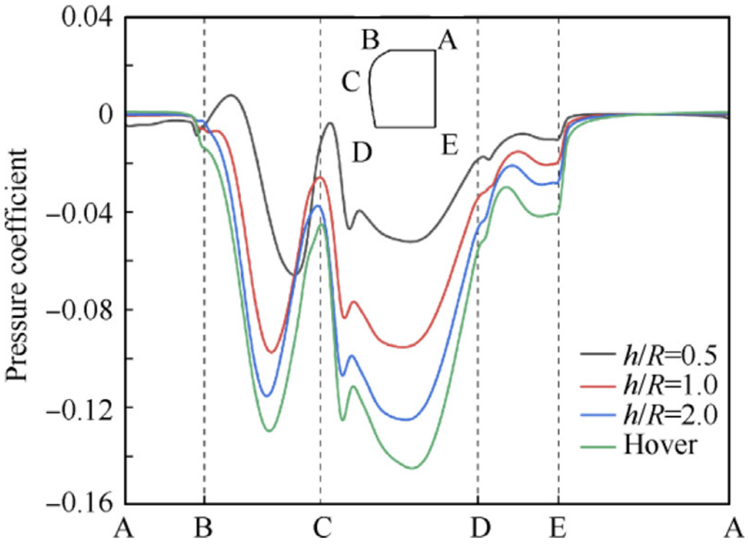

Figure 4.36: Pressure coefficient distribution on the duct section for multiple ground clearance levels, ref [34].

Normally, a tip leakage vortex is present at the blade tip, while a wall corner vortex occurs near the hub. For $h/R < 2$, stall cells are formed, which are vortices that periodically transfer motion circumferentially between adjacent blade passages, generating strong unsteady effects. Here, blade passage refers to the lateral transfer of the vortices from one passage to the next. These stall cells intensify as the height decreases, eventually forming very large structures for $h/R = 0.2$.

Chapter 5

Numerical analisys

In this chapter, we present the numerical study conducted on a scaled three-bladed 15-inch propeller enclosed in a duct, analyzing variations in thrust and torque both during hovering out of ground effect (OGE) and near the ground (IGE). The analysis was carried out using DUST, a mid-fidelity aerodynamic solver that reduces computational cost compared to full CFD simulations, while the ground effect was modeled using the image method. The aim of this chapter is to provide a detailed explanation of the methodology employed and the results obtained, comparing them with available data in the literature. The chapter is structured as follows: first, an introduction to the DUST software is provided; then, after a brief reference to previous work, the preprocessing, solver setup, and postprocessing procedures are described. Finally, the results are presented, divided into OGE and IGE conditions. The code implementation was carried out following the guidelines of the DUST user manual [35].

5.1 DUST

DUST is an open-source, medium-fidelity aerodynamic software developed at Politecnico di Milano that allows the simulation of vertical take-off and landing (VTOL) aircraft with computational times significantly lower than high-fidelity CFD, while providing comparable accuracy, except in cases of strong flow separation.

The code is written in modern Fortran with an object-oriented approach and allows combining different modeling techniques within the same simulation, such as surface panels and vortex particles, without losing mathematical consistency.

The Helmholtz decomposition of the velocity field is employed in the mathematical formulation, splitting the flow into a potential part and a vortical part, the latter being modeled with a mixed panel–vortex particle approach in a Lagrangian description.

The code contains three main files: a pre-processing file, which reads the geometry and mesh of all bodies involved; a solver file, which requires geometric data, reference frame information, simulation conditions, and solver parameters; and a post-processing file, which allows obtaining different types of results. The solver advances the simulation according to the prescribed time step. The Kutta condition is applied to ensure wake detachment from the trailing edges of solid bodies. The flow is modeled as inviscid, with compressibility effects accounted for using C81 airfoil tables dependent on the Mach number. The logical sequence of operations is illustrated in the figure 5.1

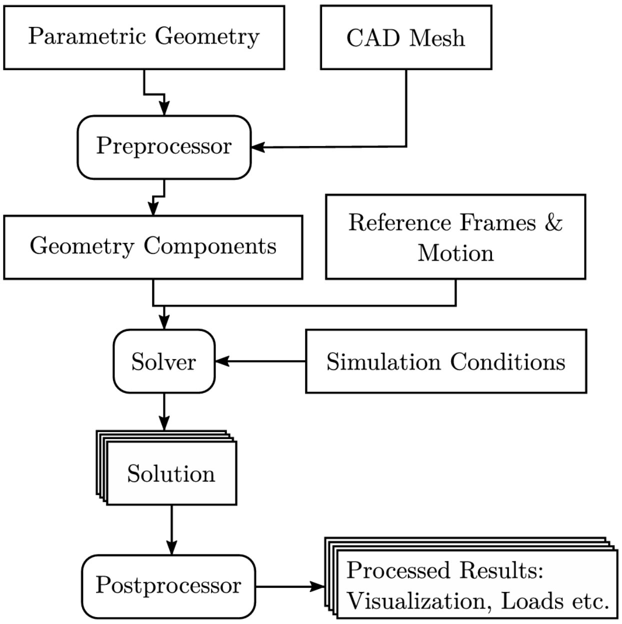

Figure 5.1: Workflow DUST, ref [6].

Individual elements are modeled as follows: surface panels are used to represent solid bodies with thickness at low angles of attack, although they cannot accurately capture stall and flow separation. A lifting line is a one-dimensional model for thin, slender lifting bodies, providing a more accurate representation than surface panels. The wake is modeled with vortex particles, which do not exhibit numerical instabilities.

5.2 Overview of Previous Work

In the previous study the blade geometry was defined based on the manufacturer-provided data, detailed in the chapter 6 on the experimental tests. The propeller was modeled using 18 spanwise and 5 chordwise elements (90 elements per blade) with a CLARK Y airfoil. The chord length tapers from 0.027 m at the hub to 0.006 m at the tip, while the geometric twist decreases from 42° to 15°, as summarized in Table 5.1. To account for compressibility effects, C81 files were generated based on the airfoil polars.

Table 5.1: Propeller parameters, ref previous work.

Parameter	**Symbol**	**Value**
Propeller diameter	D_p	15 in (0.381 m)
Number of blades	N_b	3
Airfoil	-	CLARKY
Chord range	$c_{\text{hub}} - c_{\text{tip}}$	0.027–0.006 m
Twist range	$\theta_{\text{root}} - \theta_{\text{tip}}$	42°–15°
Spanwise elements per blade	N_{span}	18
Chordwise elements per section	N_{chord}	5
Total elements per blade	$N_{\text{el,blade}}$	90

The thrust and torque were evaluated for different rotational speeds, ranging from 4000 to 6000 RPM, under OGE conditions, and the results were compared with the supplier's data for validation. Subsequently, simulations in IGE were performed. Here, to simulate the interaction between the propeller and the ground, the method of images was employed. This involves placing a mirrored, co-rotating propeller below the original one, which allows the correct capture of the interaction between the rotor and the surface without explicitly modeling the ground, while ensuring the impermeability condition at the ground. Simulations were then carried out at various heights above the ground, covering h/R values from 0.27 to 1.6 (Figure 5.2).
The results showed that for $h/R < 0.8$, the thrust ratio $T_{\text{IGE}}/T_{\text{OGE}}$ decreases, while for higher h/R values, it aligns with the Cheeseman-Bennett model, as shown in Figure 5.3(a).

Within the work, an additional study was conducted at a fixed rotational speed of 4000 RPM, varying the propeller twist in the geometry. Three configurations were analyzed: the baseline propeller, the halved-twist propeller, and the helicopter rotor with zero twist, as shown in Figure 5.3(b). The results show a roughly linear increasing trend of the thrust ratio as the propeller approaches the ground for

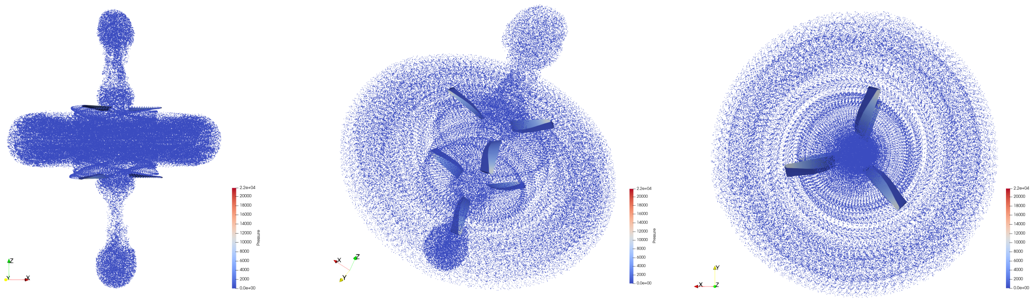

(a) Overall wake (b) Close-up view (c) Top view–circular wake

Figure 5.2: Wake visualizations from ParaView: (a) overall wake development, (b) close-up view of the blades, and (c) top view highlighting circular symmetry of the wake, ref previous work.

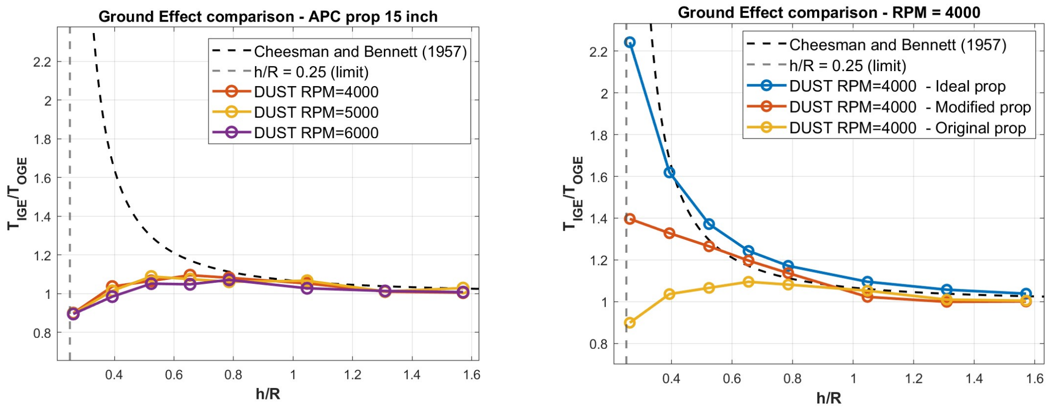

(a) Variation with rotational speed (b) Influence of blade twist

Figure 5.3: Comparison between DUST numerical predictions and the Cheeseman–Bennett model. (a) Thrust ratio variation at different rotational speeds; (b) influence of twist distribution on near-ground behavior, ref previous work.

$h/R \lesssim 1$, while for the zero-twist propeller the trend is close to that predicted by the Cheeseman-Bennett model. This can be justified by the fact that the Cheeseman-Bennett equation was originally developed to model ground effect for helicopter rotors, which typically have limited twist angles [17].

These results serve as a continuation of the previous study, providing a reference baseline to evaluate the effects of the ducted propeller in the subsequent analysis.

5.3 Geometry, Mesh and Preprocessing

5.3.1 Duct

The duct under study is axisymmetric and is generated by revolving a NACA 0018 airfoil with a chord of 0.1 m. This size allows the ducted propeller system to be positioned as close as possible to the ground without any contact between the duct and the surface. The duct diameter was chosen to provide a clearance equal to 2.9% of the propeller radius, slightly higher than the optimal 1.5% suggested by [20], to facilitate assembly. Consequently, the internal diameter is 390.9 mm, while the external diameter measures 427 mm. In addition, the propeller was positioned at a distance of 0.03 m from the leading edge.
The duct geometry and the corresponding surface mesh were generated using a MATLAB script, which took as input the NACA 0018 profile data and the number of points to distribute along the trailing edge circumference to construct the surface grid.

Table 5.2: Grid Convergence

Mesh type	Coarse	Medium	Fine
Number of points	10	30	60
Thrust total [N]	39.027	46.849	49.448

To select the appropriate number of points, a grid convergence study was performed, comparing a coarse, an intermediate, and a fine mesh, Table 5.2. The coarse mesh exhibits an error of 21% compared to the fine mesh, while the intermediate mesh shows an error of approximately 5%. The intermediate mesh was therefore chosen as it offers a good balance between accuracy and computational cost.As a result, there will be 1050 surface panels.

The MATLAB code generates two ASCII .dat files as output. The first file contains the positional coordinates (x, y, z) of each grid point in the local reference system, while the second file defines the connectivity between these points. These files are used as input for constructing the basic mesh in DUST and are designed for straightforward implementation, Figure 5.5. The relevant geometric parameters are summarized in Table 5.3.

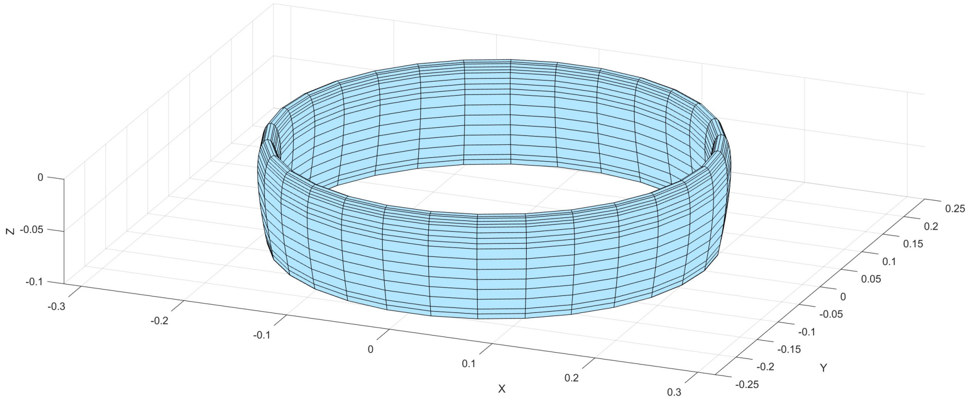

Figure 5.4: Three-Dimensional Duct Geometry and Mesh Generation

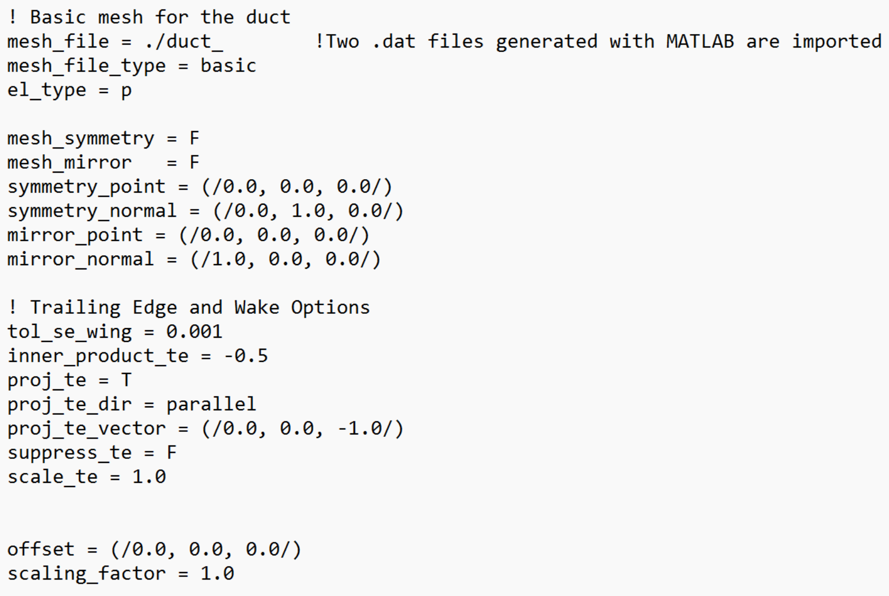

```
! Basic mesh for the duct
mesh_file = ./duct_        !Two .dat files generated with MATLAB are imported
mesh_file_type = basic
el_type = p

mesh_symmetry = F
mesh_mirror   = F
symmetry_point = (/0.0, 0.0, 0.0/)
symmetry_normal = (/0.0, 1.0, 0.0/)
mirror_point = (/0.0, 0.0, 0.0/)
mirror_normal = (/1.0, 0.0, 0.0/)

! Trailing Edge and Wake Options
tol_se_wing = 0.001
inner_product_te = -0.5
proj_te = T
proj_te_dir = parallel
proj_te_vector = (/0.0, 0.0, -1.0/)
suppress_te = F
scale_te = 1.0


offset = (/0.0, 0.0, 0.0/)
scaling_factor = 1.0
```

Figure 5.5: Basic mesh code

Table 5.3: Duct parameters

Parameter	**Symbol**	**Value**
Blade–duct tip clearance	δ	10.9 mm
Duct chord	c_D	0.10 m
Internal duct diameter	D_{Di}	0.3909 m
Duct mesh elements	N_{duct}	1050 panels

To simulate the ground effect, a mirrored co-rotating propeller was placed below the primary one. The same procedure was applied to the duct by generating a separate mirrored file, ensuring that the duct geometry also reflects the ground influence in the simulation.

5.3.2 Preprocessing

The preprocessing phase in DUST is used to define all the components of the simulation and to prepare the geometric data for the solver. In the 'dust_pre' file, each component is specified by its name, such as rotor or propeller. Mirrored files for the components are also included when required. Additionally, a reference is provided to distinguish the different components within the simulation, and a file containing the preprocessing results is loaded, which will later be used by the solver to perform the simulations.

During preprocessing, a key consideration for the duct is maintaining physical consistency. In particular, the software must correctly identify the trailing edges to ensure proper wake detachment.

5.4 Solver and numerical procedures

The solver requires, in addition to the geometry, information regarding the Reference Frames and Motion, which includes the positioning coordinates of the various components, their orientation, and their rotational velocity with respect to the z-axis. For the OGE (Out of Ground Effect) conditions, the propeller rotational speed was varied from 1500 to 6000 RPM in steps of 500 RPM, with some intermediate values added to enable a proper comparison with the experimental data. The duct, on the other hand, was kept stationary and properly aligned with respect to the propeller.

Simulations with the mirrored propeller were performed at the following distances from the ground: $h = [0.1, 0.15, 0.2, 0.3, 0.4, 0.6, 0.9]$ m, corresponding to $h/R = [0.52, 0.79, 1.05, 1.57, 2.10, 3.15, 4.72]$, and at rotational speeds of 1500, 2000, 2500, 3000, 3500, and 4000 RPM.

The simulation conditions were defined so that the propeller completed five full revolutions around the z-axis for each rotational speed. The total simulation time was computed as:

$$t_{end} = \frac{2\pi}{\omega} \cdot 5$$

where ω is the angular velocity corresponding to the prescribed RPM. A constant timestep dt was chosen to ensure that each revolution was discretized into 100 iterations, providing adequate temporal resolution.

5.5 Postprocessing

The solver provides solutions at regular time intervals, which must be processed through postprocessing to derive the quantities of interest. The types of postprocessing from DUST that we will use are as follows:

- **Visualization**, which outputs .vtu files for each saved time step and allows the temporal evolution of the simulation to be visualized using ParaView.
- **Integral loads**, which generates for each component a .dat file containing the three components of forces (F_x, F_y, F_z) and moments (M_x, M_y, M_z).
- **Sectional loads**, which produces four .dat files containing the loads and moments for each section of the blade along its span.
- **Flow Field**, which outputs a .vtu file for each saved time step and provides the instantaneous velocity and pressure fields, allowing the visualization of the flow induced by the solution of the singular elements.

The .dat files are then analyzed using a MATLAB script to extract the quantities of interest and observe their variation over time.

5.6 Results

The following section presents the results of the numerical simulations, distinguishing between IGE and OGE conditions, which were performed for the parameters reported in Table 5.4.

Case	**RPM**	**h**	h/R
OGE	[1500-6000]	-	-
IGE	[1500- 4000]	0.1 - 0.9	0.53- 4.73

Table 5.4: Simulation contitions for OGE and IGE ducted propeller.

In the following, the terms Open Propeller (OP) and Shrouded Rotor (SR) are used for convenience to distinguish between the bare propeller and the propeller with duct configurations. These terms do not imply that the studied propellers are helicopter rotors; they are adopted solely to improve readability and avoid repeating long expressions throughout the text.

5.6.1 OGE

Figure 5.6 shows the ducted propeller in ParaView and the wake correctly generated outside the ground effect, leaving the duct from the trailing edge.

(a) (b) (c)

Figure 5.6: Wake visualizations from ParaView: (a) and (b) Ducted propeller, (c) Wake .

The results data were collected using MATLAB to generate the time histories of thrust and torque, ensuring that steady-state values were extracted after the initial transients had decayed and numerical convergence was achieved, as shown in Figure 5.7.

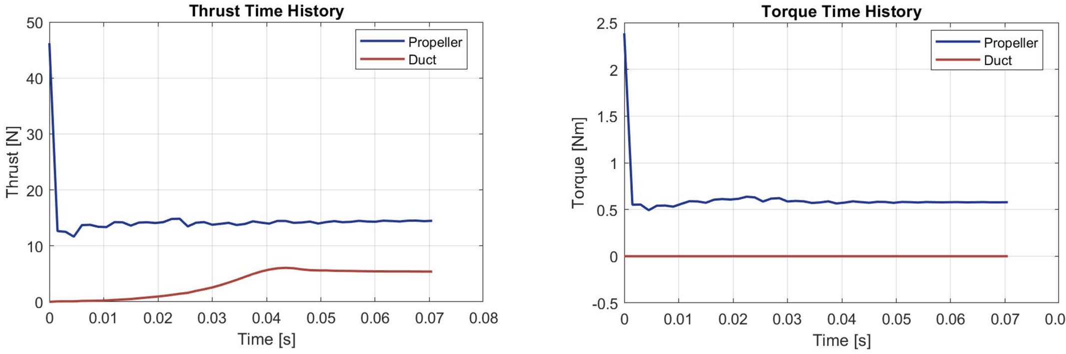

Figure 5.7: Example of thrust and torque time histories obtained at 4000 RPM and h = 0.1 m, showing convergence to steady periodic behavior.

The simulations of the propeller with the duct were carried out for each of the three types of propellers studied in the previous work: the baseline propeller, the halved propeller, and the helicopter-type rotor. For each configuration, thrust and torque are presented for the shrouded rotor (SR), showing separately the contributions of the propeller and the duct, along with the total SR system. In addition, the open propeller (OP) results are included for comparison, providing a clear reference to evaluate how the presence of the duct affects the performance of each propeller configuration across the entire range of rotational speeds considered, Figures 5.8, 5.9 and 5.10.

For the baseline propeller the results show, Figure 5.8(a), that the propeller thrust remains almost unchanged between the Open Propeller (OP) and Shrouded Rotor (SR) configurations for nearly all the rotational speeds considered. Overall, the total thrust of the propeller-duct system increases by 30–52%, with the duct contributing up to 26.9% of the total. For the propeller torque in the SR configuration, an increase is observed compared to the OP case, which grows progressively with the rotational speed, ranging from 1.16 to 18.55%, Table 5.5. On the other hand, the duct, not being in motion, exhibits zero torque at all times, Figure 5.8(b).

The behavior of the halved propeller, Figure 5.9, is slightly different, as it is observed that the performance of the propeller with the duct decreases compared to the isolated rotor, but resulting in an overall increase in total performance ranging from 10.81 to 20.07%, which is very close to the approximately 20% measured by Li et al. [21]. On the other hand, the duct increases its performance, contributing up

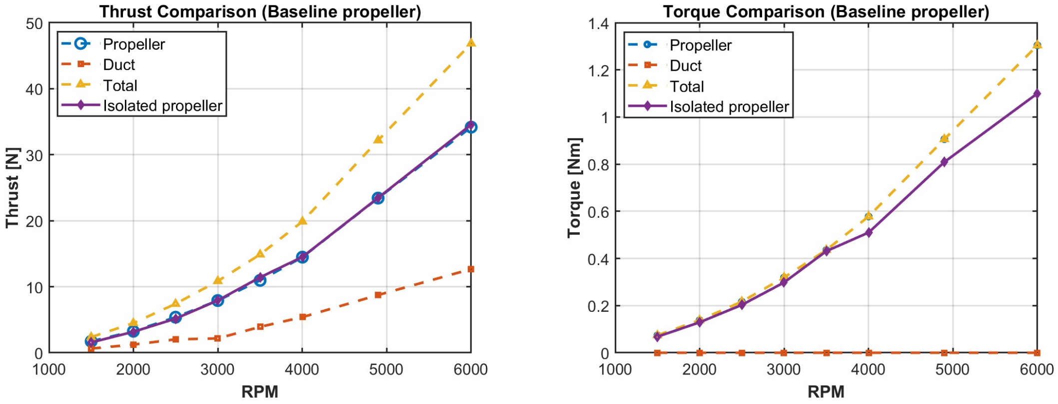

(a) Thrust - Baseline Prop (b) Torque - Baseline Prop

Figure 5.8: Thrust and Torque for Baseline Propeller With/Without Duct.

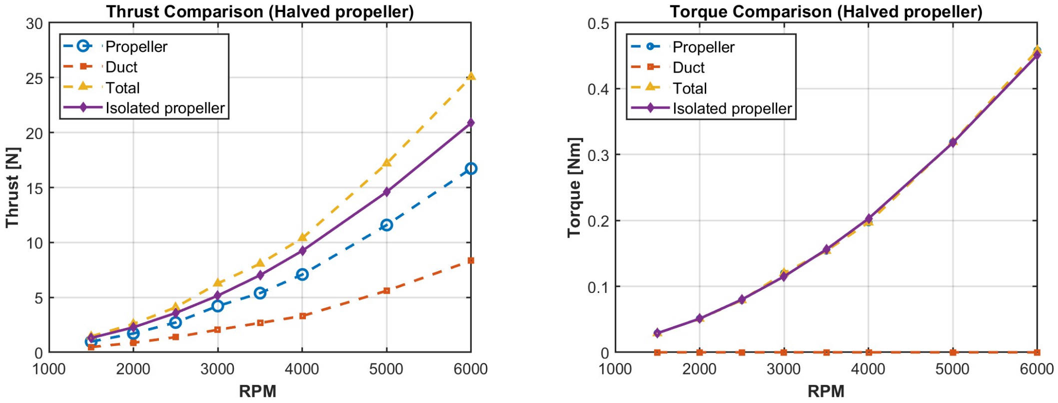

(a) Thrust - Halved Prop (b) Torque - Halved Prop

Figure 5.9: Thrust and Torque for Halved Propeller With/Without Duct.

to 33.7% of the total, Table 5.6. The torque does not show significant differences between OP and SR configurations.

For the blade type associated with the helicopter rotor with zero twist, thrust does not exhibit a monotonic trend with rotational speed, as shown in Figure 5.10 (a). Unlike the halved propeller, the isolated propeller produces less thrust than the ducted one, resulting in a total thrust increase of up to 125.81%. This trend continues up to 5000 RPM, after which the behavior changes, with the open propeller outperforming the ducted configuration.

Regarding the duct, its contribution is consistent with previous cases up to

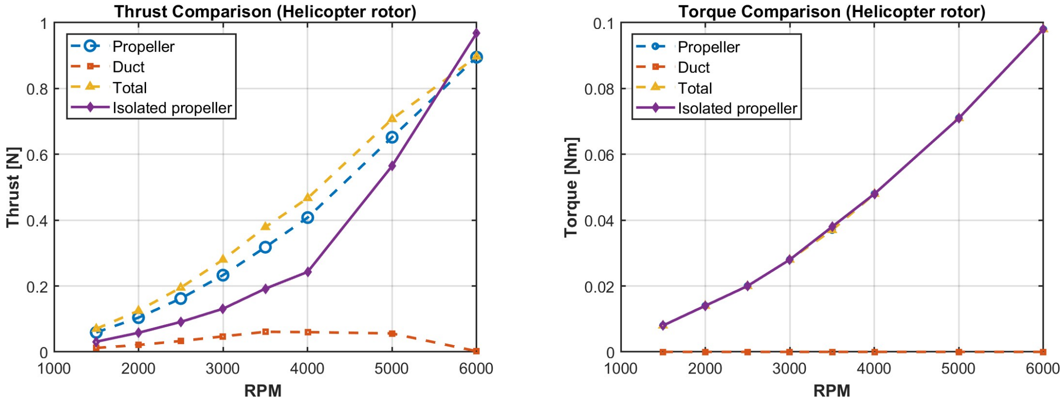

(a) Thrust - Helicopter rotor (b) Torque - Helicopter rotor

Figure 5.10: Thrust and Torque for Helicopter rotorWith/Without Duct.

3000 RPM, remaining limited and reaching a maximum of 16.9% (see Table 5.7). Beyond 3000 RPM, its performance decreases almost to zero at 6000 RPM. The propeller torque, however, is barely affected by the presence of the duct (see Figure 5.10 and Table 5.7).

Table 5.5: Percentage increases in thrust and torque, and individual component contributions for the Baseline Propeller.

RPM	T Incr [%]	Q Incr [%]	Prop Contr [%]	Duct Contr [%]
1500	51.67	8.82	73.1	26.9
2000	41.49	6.98	72.5	27.5
2500	43.45	6.90	72.7	27.3
3000	36.93	7.05	72.8	27.2
3500	30.28	1.16	73.6	26.4
4000	36.95	13.33	72.8	27.2
5000	37.11	11.99	72.8	27.2
6000	35.56	18.55	72.9	27.1

Note: The increases are relative to the OP, while the contributions of the duct and propeller are calculated with respect to the total thrust of the SR.

Figure 5.11 (a) compares the T_{OP}/T_{SR} ratio as a function of rotational speed for all three configurations. It can be observed that the addition of the duct leads to a reduction in the propeller's performance for the halved propeller (blue line), only minor changes for the baseline propeller (red line), and an opposite trend for the helicopter-type rotor (yellow line). However, as previously discussed, a decrease

Table 5.6: Percentage increases in thrust and torque, and individual component contributions for the Halved Propeller.

RPM	T Incr [%]	Q Incr [%]	Prop Contr [%]	Duct Contr [%]
1500	10.81	0.00	67.0	33.0
2000	13.63	0.00	66.4	33.6
2500	14.44	-1.25	66.3	33.7
3000	21.56	4.35	67.3	32.7
3500	14.84	-1.28	66.8	33.2
4000	12.41	-2.96	68.2	31.8
5000	17.76	0.31	67.4	32.6
6000	20.07	1.55	66.7	33.3

Note: The increases are relative to the OP, while the contributions of the duct and propeller are calculated with respect to the total thrust of the SR.

Table 5.7: Percentage increases in thrust and torque, and individual component contributions for the Helicopter Rotor.

RPM	T Incr [%]	Q Incr [%]	Prop Contr [%]	Duct Contr [%]
1500	125.81	0.00	84.3	15.7
2000	115.52	0.00	83.2	16.8
2500	114.29	0.00	83.1	16.9
3000	113.74	0.00	83.2	16.8
3500	97.40	-2.63	83.9	16.1
4000	92.18	0.00	87.2	12.8
5000	25.13	0.00	92.1	7.9
6000	-7.33	0.00	99.8	0.2

Note: The increases are relative to the OP, while the contributions of the duct and propeller are calculated with respect to the total thrust of the SR.

in propeller thrust does not necessarily imply a lower overall thrust of the entire system.
In Figure 5.11 (b), comparatively smaller variations in torque can be noticed among the different configurations.

In general, the duct has led to an increase in thrust in all the cases studied, with a trend as a function of RPM fully consistent with the findings of Wei et al. [23], except for the highest RPM of the helicopter rotor. The thrust generated by the duct can be explained by the fact that the rotation of the blades induces a flow, creating pressure variations along the inner surface of the duct and thus producing an additional thrust component contributed by the duct itself, Figure 5.12, as also highlighted by Zawodny et al. [13], but in general also by other studies in the

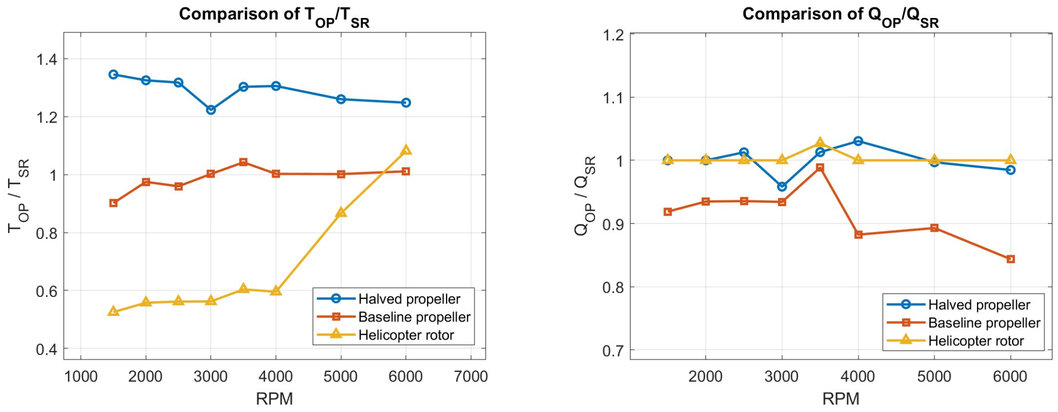

(a) Thrust

(b) Torque - Helicopter rotor

Figure 5.11: Comparison of the T_{OP}/T_{SR} ratio (a) and Q_{OP}/Q_{SR} ratio (b) for the three configurations: baseline propeller, halved propeller, and helicopter rotor.

literature presented in Section 4.1. In [13], it was also shown that the open propeller produces higher thrust compared to the ducted configuration, albeit at the cost of increased power consumption. However, in this thesis it is observed that the addition of the duct leaves the performance of the single propeller unchanged for the baseline configuration or reduces it for the halved propeller, as also highlighted in [22], [23], and [25]. Furthermore, the torque is less affected by the addition of the duct.

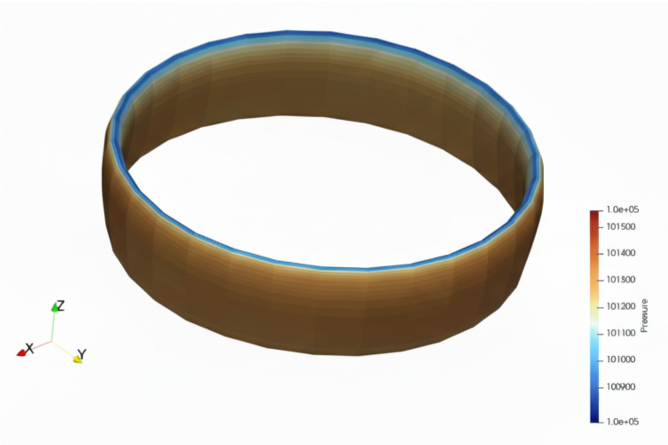

Figure 5.12: Pressure distribution along the duct from ParaView

Wake and Velocity Field Visualizations

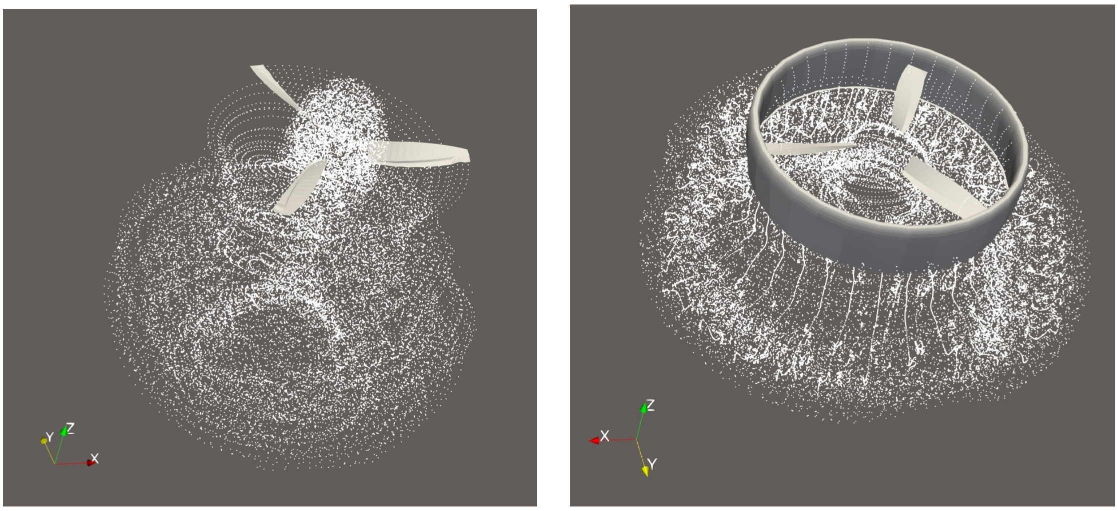

(a) Open Propeller (b) Ducted propeller

Figure 5.13: Comparison between the wake of the Open Propeller (a) and the Ducted Propeller (b).

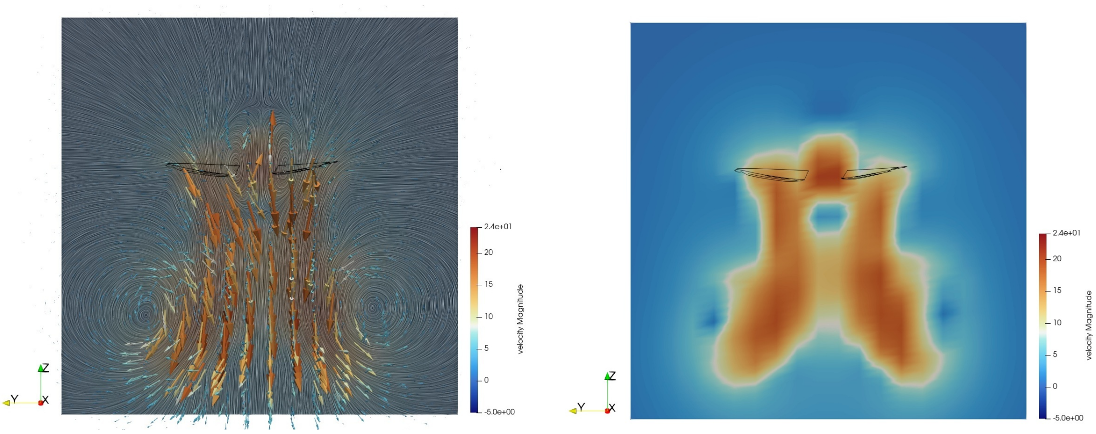

(a) (b)

Figure 5.14: Representation of the velocity field in the open propeller baseline, using arrows (a) or surfaces (b).

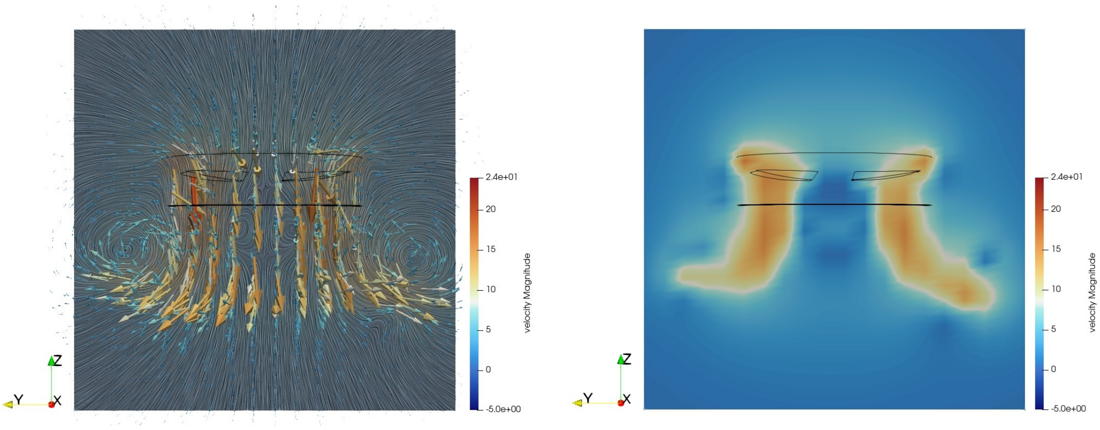

(a) (b)

Figure 5.15: Representation of the velocity field in the baseline ducted propeller, using arrows (a) or surfaces (b).

The wakes of the propeller and the ducted system are visualized using particles in Figure 5.13, highlighting particle motion around the rotor and flow detachment from the duct's trailing edge. Flow field postprocessing for the baseline propeller is shown in Figures 5.14 and 5.15, indicating that velocities in the OP are generally higher and the wake more contracted, as expected from actuator disk theory [28]. The z-component of velocity, shown in Figure 5.16, exhibits negative values consistent with the downward motion of the flow.

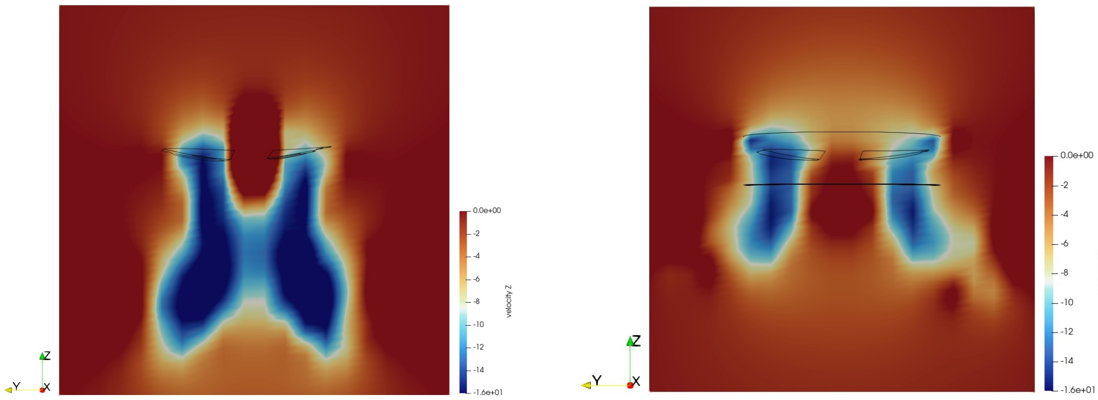

(a) (b)

Figure 5.16: Representation of the velocity z field in the baseline open (a) and ducted (b) propeller.

Distribution of Thrust and Torque Along the Blade

After analyzing the global effect of the duct on the propeller, this section focuses on the distribution of thrust and torque along each blade section, in order to highlight how the addition of the duct modifies the local performance for the baseline propeller, the halved propeller, and the helicopter rotor.
The loads were obtained by performing the sectional loads in the post-processing, and it was verified that the total thrust and torque values, obtained by summing the contributions of each section, matched those calculated using the integral load.

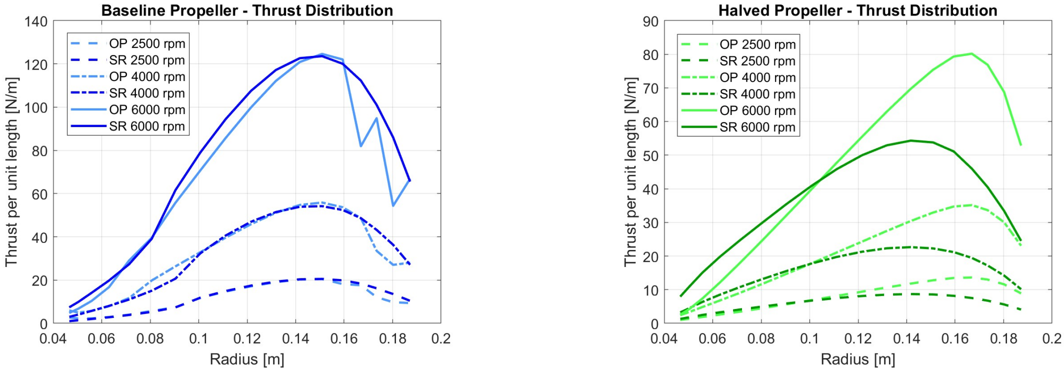

(a) Baseline prop (b) Halved prop

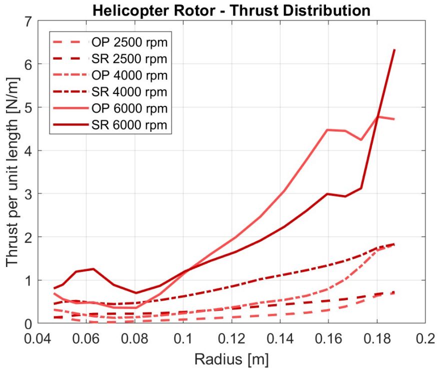

(c) Helicopter rotor

Figure 5.17: Thrust Distribution along the Blade in OP and SR Configurations at Different RPMs.

Figure 5.17 shows the thrust distribution per unit length along the blade radius at different rotational speeds for the three types of blades in OP and SR. For the baseline propeller, as observed in Figure 5.11(a) (red line), there are no significant thrust variations between OP and SR; therefore, it is interesting to focus on the different thrust distribution per unit length along the blade. Figure 5.17(a) shows that the addition of the duct produces higher thrust toward the tip, as expected, since the duct reduces the effects of tip vortices on the propeller, and a decrease in thrust in the region between 0.07 and 0.1 m.

For the halved propeller (fig. 5.17(b)), it is clearly observed that the area under the OP curves is larger than that of the SR. Moreover, the lift distribution is shifted more toward the center of the blade rather than the tip, in contrast to what is observed for the baseline propeller. However, it should be noted that this does not represent a real propeller, but rather a geometry created solely to visualize the effects of the twist.

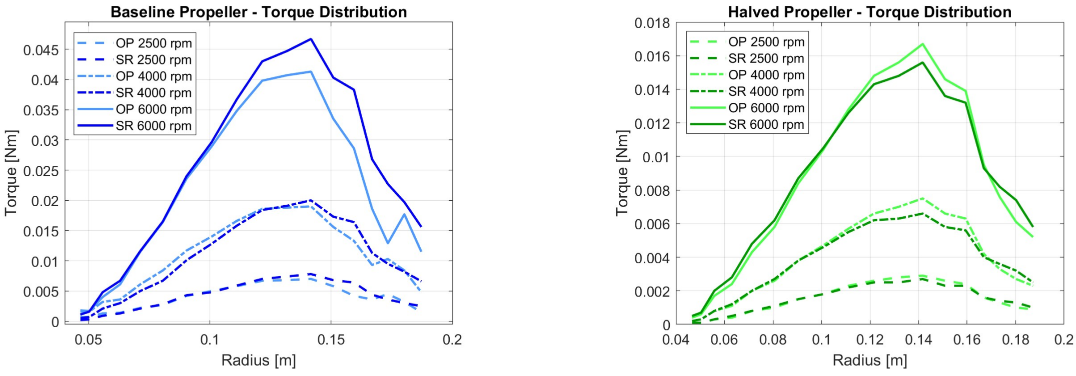

(a) Baseline prop (b) Halved prop

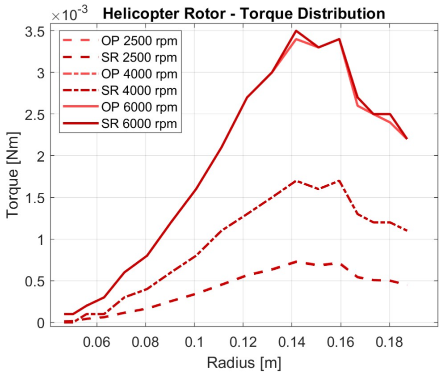

(c) Helicopter rotor

Figure 5.18: Torque Distribution along the Blade in OP and SR Configurations at Different RPMs.

In the zero twist propeller (fig. 5.17(c)), similarly to the baseline propeller, an increase in sectional thrust towards the blade tip is observed for the SR, mainly at high rotational speeds.

Figure 5.18 reports the torque distribution along the blade for different RPMs. For the baseline propeller (fig. 5.18(a)), the addition of the duct leads to an increase in torque while reducing local peaks.
In the halved propeller (fig. 5.18(b)), a decrease in torque is observed in the central region for the SR, while an increase occurs near the blade tip.
For the helicopter rotor (fig. 5.18(c)), no significant changes are observed, except for the last part of the blade at 6000 RPM, where the OP curve is slightly lower than the SR.

To better highlight the differences among the various configurations, Figure 5.19 presents all cases together, allowing a direct comparison of thrust (fig. 5.19(a)) and torque (fig. 5.19(b)).

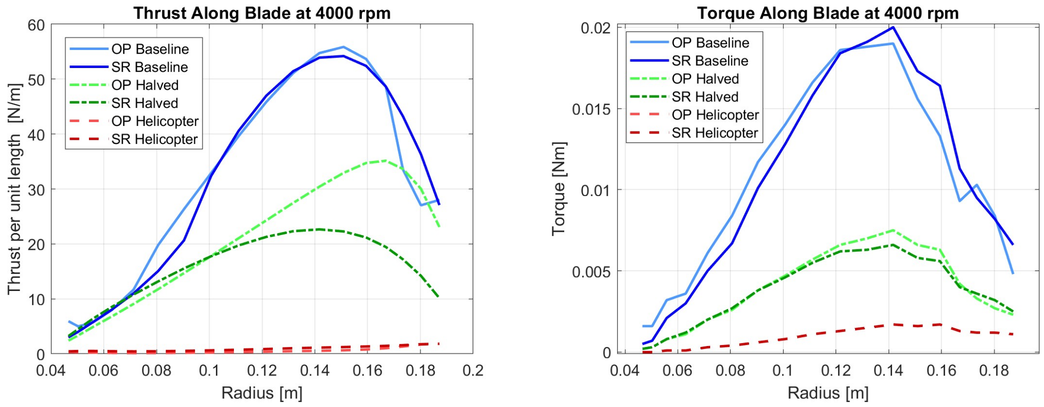

(a) Thrust (b) Torque

Figure 5.19: Comparison of Thrust (a) and Torque (b) for All Three Configurations With and Without Duct.

5.7 IGE

Figure 5.20 shows the wake generated by bringing two ducted propellers close together, thus simulating the ground effect. In the top view (5.20(c)), the wakes appear practically identical. Moreover, in Figure 5.20(a) a horizontal region forms between the two ducts, consistent with the non-penetration condition.

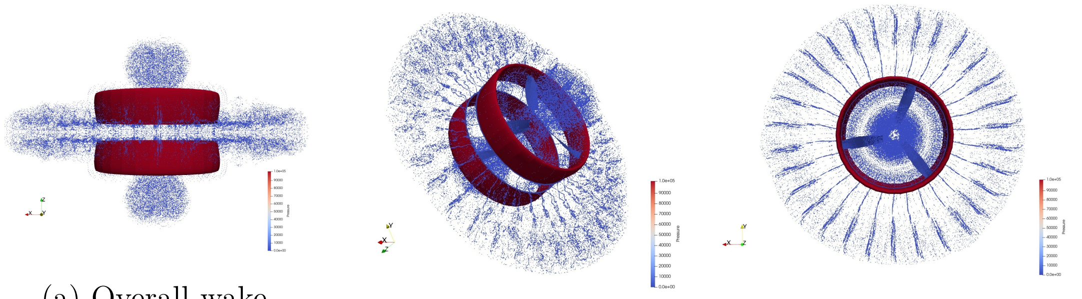

(a) Overall wake

(b) Close-up view

(c) Top view–circular wake

Figure 5.20: Wake visualizations from ParaView: (a) overall wake development, (b) close-up view of the blades, and (c) top view highlighting circular symmetry of the wake.

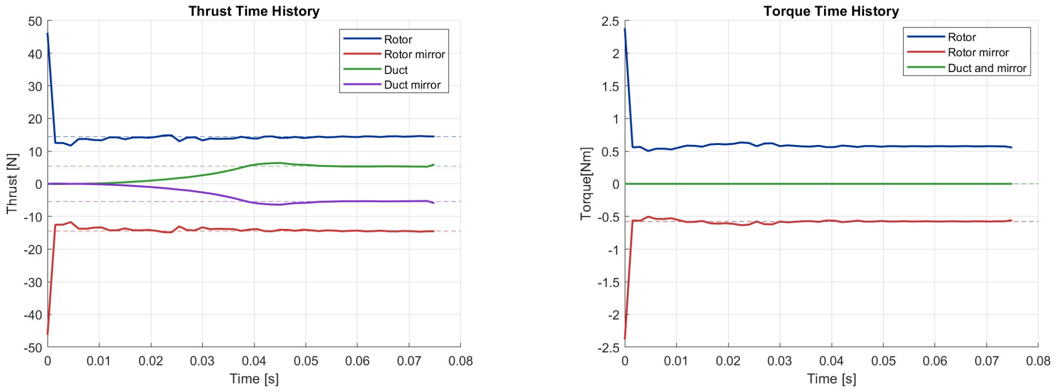

Figure 5.21: Example of thrust and torque time histories obtained at 4000 RPM and h/R = 2.1 m.

With the presence of the duct, significant instabilities are observed during the simulations with the mirrored system, mainly at very close distances, phenomenon also observed by LUO et al. [34]. For this reason, the initial transient period was discarded, and the mean values were considered. The thrust and torque time

histories for the mirrored components show a perfectly symmetric behavior, see Figure 5.21.
To facilitate comparison among the three configurations, all simulations were first conducted at 4000 RPM. The resulting thrust and torque are shown with the contributions of the propeller, the duct, and the total system, providing a clear picture of how each component behaves as the rotor approaches the ground, Figures 5.22, 5.23 and 5.24.

The behavior of the baseline propeller in IGE is shown in Figure 5.22(a), which illustrates how proximity to the ground affects the contributions of the propeller (blue line) and the duct (red line), as well as the overall system behavior (yellow line). It can be observed that for rotor to ground distances $h/R < 1$, the rotor experiences a reduction in thrust compared to the out of ground effect (OGE) condition; a similar trend is also observed for the duct for $h/R < 2$. The decrease in duct effectiveness in ground effect has also been reported by Zhao et al. [7] and LUO et al.[34], along with an overall reduction in thrust. However, this conclusion contrasts with the results of Han et al. [8], who report an increase in total thrust as the rotor approaches the ground. In general, for the case under study, the ground effect becomes negligible for $h/R > 2$.
Regarding torque, the ratio Q_{IGE}/Q_{OGE} remains nearly constant up to $h/R = 1$; for smaller values it increases, implying that more power at the same RPM is required to maintain hovering at those heights, as shown in Figure 5.22(b).

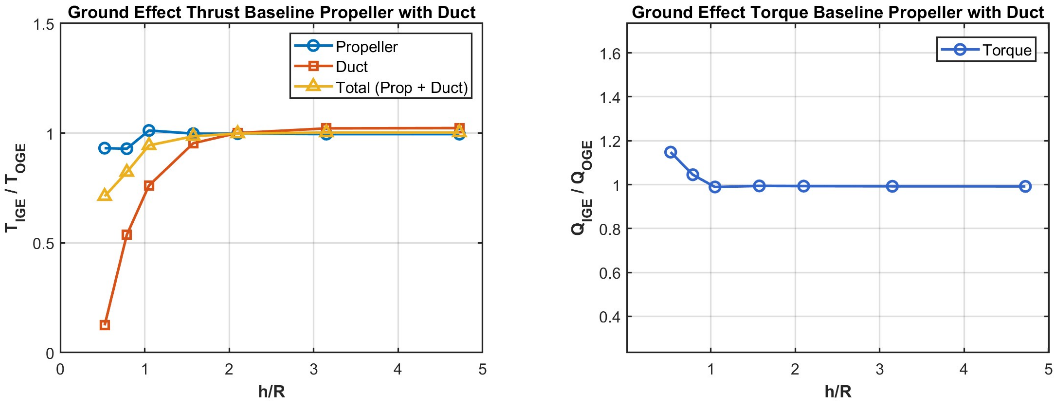

(a) Thrust - Baseline Prop

(b) Torque - Baseline Prop

Figure 5.22: Comparison of thrust and torque with duct, Baseline Prop 4000 RPM.

The halved propeller, shown in Figure 5.23(a), exhibits a thrust ratio trend

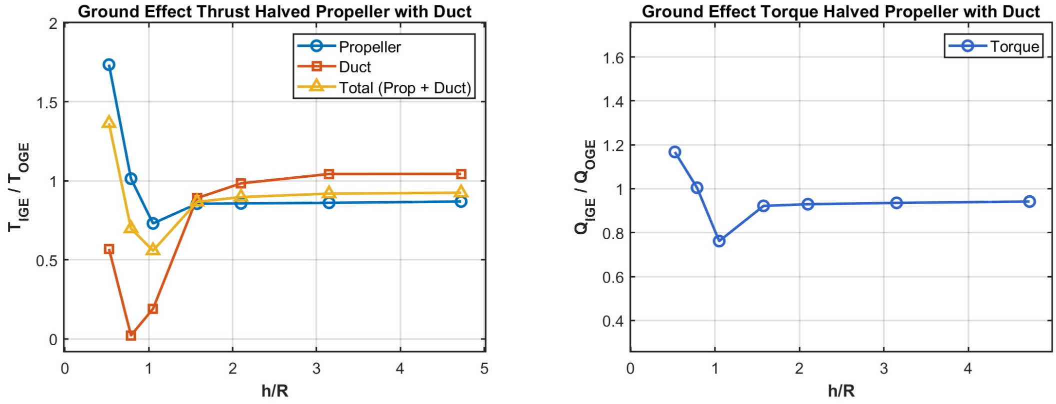

(a) Thrust - Halved Prop (b) Torque - Halved Prop

Figure 5.23: Comparison of thrust and torque with duct, Halved Prop 4000 RPM.

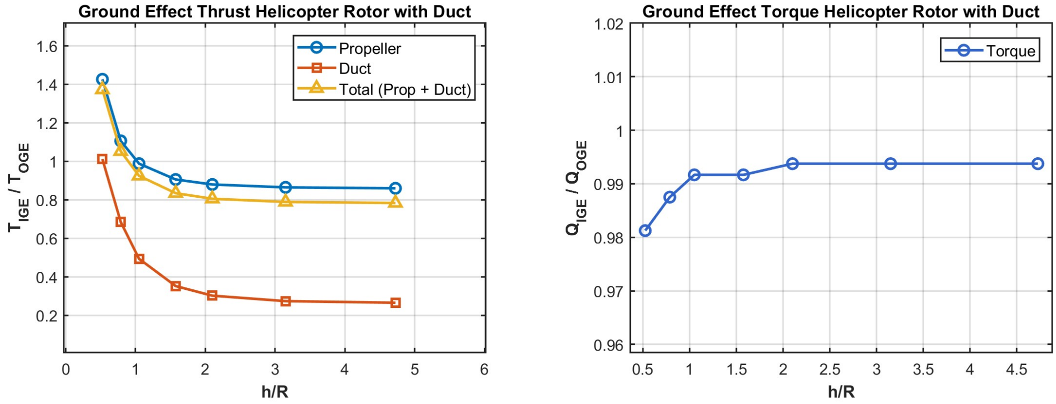

(a) Thrust - Helicopter rotor (b) Torque - Helicopter rotor

Figure 5.24: Comparison of thrust and torque with duct, Helicopt rotor 4000RPM.

similar to that of the baseline propeller for $h/R > 2$. In this region, however, the curves do not perfectly align at 1 on the ordinate, as would be expected under OGE conditions, likely due to slight numerical errors caused by oscillations between the loads on the duct and the mirrored propeller during the simulation, or it may not be due to an error at all. In fact, according to LUO et al. [34], the presence of the duct extends the ground effect influence up to $h/R = 4$.

For $h/R < 2$, the IGE thrust initially decreases and then increases for both the propeller and the duct; this increase near the ground was also observed by Han et al. in their experiments [33]. The torque, on the other hand, does not show significant differences compared to the baseline propeller, as highlighted in Figure 5.23(b).

The behavior of the helicopter rotor, shown in Figure 5.24(a), indicates that the propeller thrust increases as it approaches the ground, more significantly than for the SR, as also observed by Han et al. [33]. The thrust ratio of the duct, as expected, remains below 1 but exhibits a rising trend when approaching the ground and never reaches OGE conditions at larger distances. Regarding torque, shown in Figure 5.24(b), no significant variations are observed, although the Q_{IGE}/Q_{OGE} ratio decreases for small h/R values, indicating a reduced power demand from the engine.

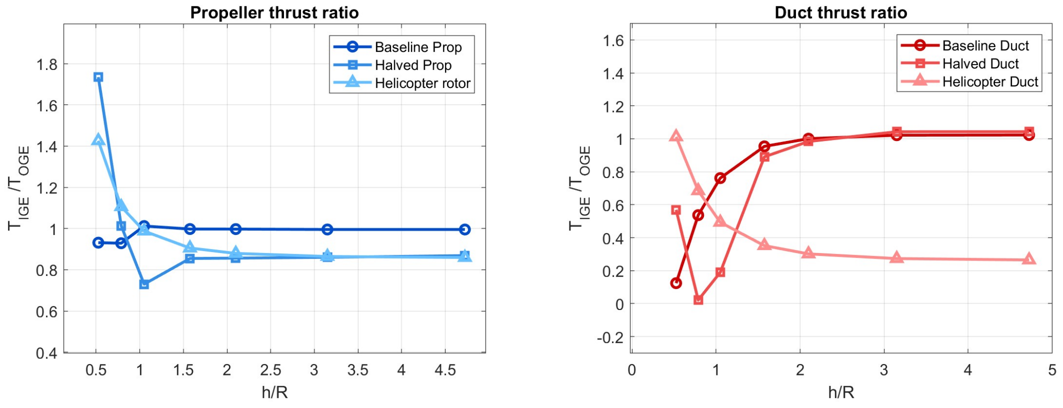

(a) Propeller (b) Duct

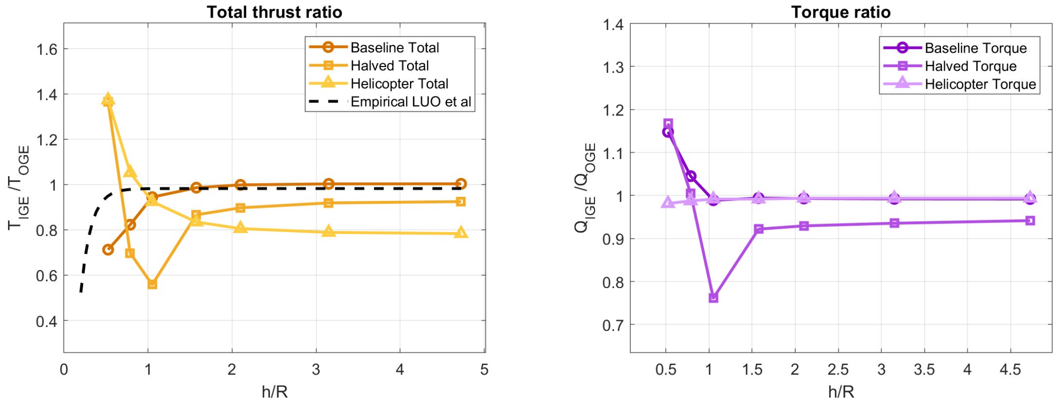

(c) Total (d) Torque

Figure 5.25: Comparison of individual contributions to the thrust ratio for the three configurations (a), (b), (c) and of the torque ratio (d).

Figure 5.26 provides an immediate comparison of the three configurations, showing the thrust ratio of the propeller, the duct, the total thrust, and the torque ratio in four distinct plots. In plot 5.26 (c), the empirical relation 4.1 from Luo et al. [34] has been added, which describes how the total thrust decreases near the ground, with a trend similar to that observed for the baseline propeller (dark orange line).

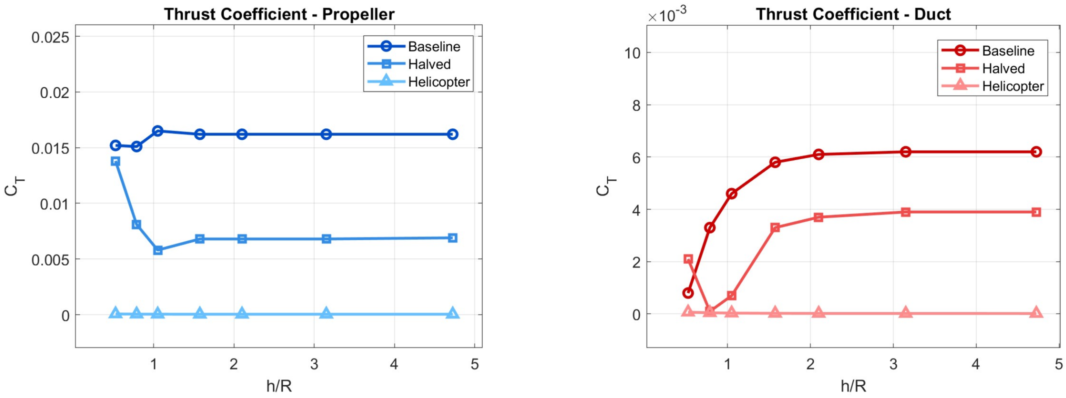

(a) C_T Propeller

(b) C_T Duct

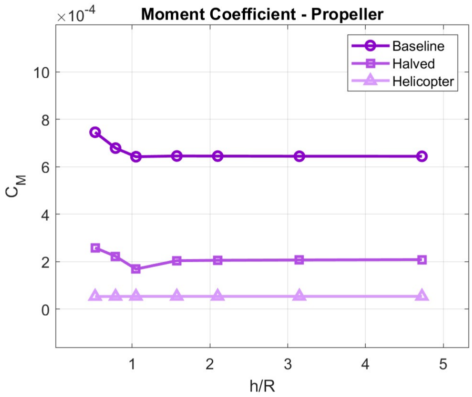

(c) C_M

Figure 5.26: Comparison of thrust coefficients in the propeller (a) and in the duct (b), and of torque coefficients (c) at 4000 RPM.

In general, most of the changes are observed for $h/R < 2$, and their highly divergent trends may also be due to the generation of stall cells along the blade [34], which are not easily captured by DUST. In fact, one of its limitations was the inability to accurately capture stall and flow separation. Overall, it is observed, except for the helicopter rotor, that the reduction in duct thrust is due to a decrease in thrust in the portion of the duct downstream of the propeller [34].
Zhao et al. [24] highlighted that the behavior of the total thrust in IGE conditions is strongly influenced by the relative contributions of the duct and the blades. This

implies that the variations of total thrust observed in IGE can be interpreted based on the relative contributions measured in OGE. In the present study, however, this effect is less relevant, since the duct consistently contributes less than 50% of the total thrust, in agreement with the findings of Han et al. [33].

A study was conducted not only at 4000 rpm but also for different rpm numbers to see how they affected performance, Figure 5.27. It has been found that in general, higher RPM values result in greater thrust generation and higher T_{IGE}/T_{OGE} values, for all system components. However, for torque there is an opposite trend, Figure 5.27(d).

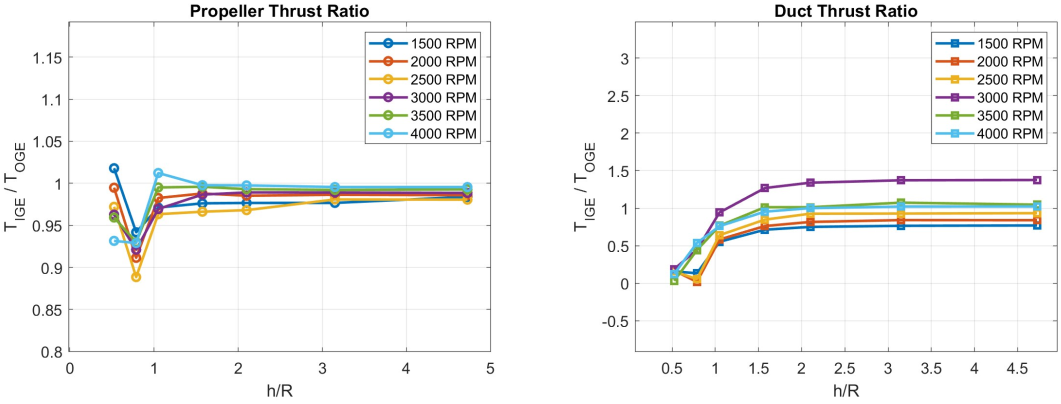

(a) Propeller (b) Duct

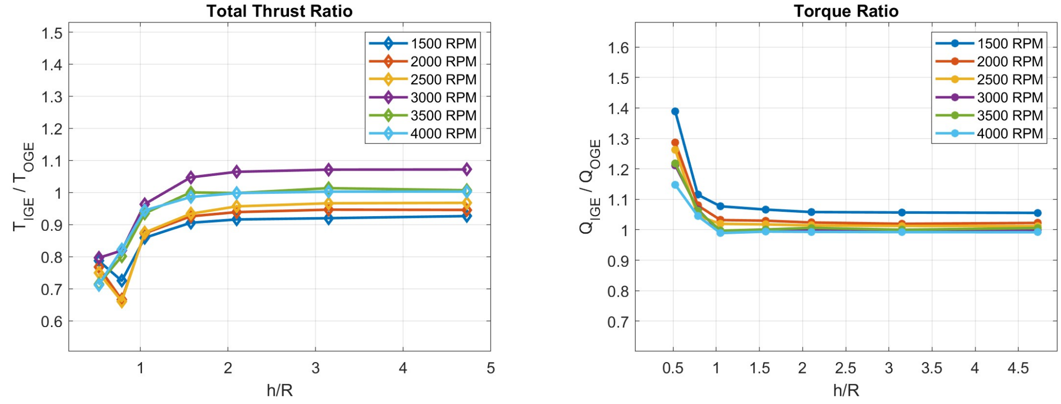

(c) Total (d) Torque

Figure 5.27: Comparison of individual contributions to the thrust ratio for the three configurations (a), (b), (c) and of the torque ratio (d) for different RPM.

Standard Deviation

The standard deviation (SD) represents a measure of the variability of the data with respect to the mean value and allows quantifying the uncertainty of the results obtained from the simulations. In this study, the simulations exhibit significant instability, especially for small values of h/R, making it necessary to adopt a careful approach to estimate the accuracy of the results.

The calculation of the standard deviations was performed separately for the propeller and the duct under ground effect conditions. The total deviation was obtained as

$$SD_{\text{total}} = \sqrt{SD^2_{\text{propeller}} + SD^2_{\text{duct}}}$$

Due to the strong instability of the mirrored system results, particularly for low h/R values, it was necessary to use the mean values while discarding the initial transient portion; these values deviate slightly from those corresponding to fully stationary conditions.

Table 5.8: Thrust Propeller Data with Standard Deviations and Percentage Errors

h/R	T_{IGE}	T_{OGE}	SD_{IGE}	SD_{OGE}	err$\%_{\text{IGE}}$	err$\%_{\text{OGE}}$
0.52	13.490	14.482	1.090	0.100	8.08	0.69
0.79	13.453	14.482	0.560	0.100	4.16	0.69
1.05	14.659	14.482	0.660	0.100	4.50	0.69
1.57	14.448	14.482	0.310	0.100	2.15	0.69
2.10	14.445	14.482	0.260	0.100	1.80	0.69
3.15	14.417	14.482	0.220	0.100	1.53	0.69
4.72	14.416	14.482	0.220	0.100	1.53	0.69

Table 5.9: Thrust Duct Data with Standard Deviations and Percentage Errors

h/R	T_{IGE}	T_{OGE}	SD_{IGE}	SD_{OGE}	err$\%_{\text{IGE}}$	err$\%_{\text{OGE}}$
0.52	0.670	5.398	3.530	0.060	526.87	1.11
0.79	2.897	5.398	3.490	0.060	120.47	1.11
1.05	4.111	5.398	0.950	0.060	23.11	1.11
1.57	5.150	5.398	0.870	0.060	16.89	1.11
2.10	5.402	5.398	0.780	0.060	14.44	1.11
3.15	5.515	5.398	0.770	0.060	13.96	1.11
4.72	5.522	5.398	0.770	0.060	13.94	1.11

Observing the standard deviation at 4000 for the propeller, Figure 5.28(a) shows that the values are higher near the ground and progressively decrease as the system

Table 5.10: Thrust Total System Data with Standard Deviations and Percentage Errors

h/R	T_{IGE}	T_{OGE}	SD_{IGE}	SD_{OGE}	err$\%_{\text{IGE}}$	err$\%_{\text{OGE}}$
0.52	14.160	19.880	3.694	0.117	26.09	0.59
0.79	16.350	19.880	3.535	0.117	21.62	0.59
1.05	18.769	19.880	1.157	0.117	6.16	0.59
1.57	19.599	19.880	0.924	0.117	4.71	0.59
2.10	19.847	19.880	0.822	0.117	4.14	0.59
3.15	19.932	19.880	0.801	0.117	4.02	0.59
4.72	19.938	19.880	0.801	0.117	4.02	0.59

Table 5.11: Torque Total System Data with Standard Deviations and Percentage Errors

h/R	Q_{IGE}	Q_{OGE}	SD_{IGE}	SD_{OGE}	err$\%_{\text{IGE}}$	err$\%_{\text{OGE}}$
0.52	0.663	0.578	0.040	0.000	6.03	0.00
0.79	0.604	0.578	0.020	0.000	3.31	0.00
1.05	0.572	0.578	0.000	0.000	0.00	0.00
1.57	0.575	0.578	0.000	0.000	0.00	0.00
2.10	0.574	0.578	0.000	0.000	0.00	0.00
3.15	0.574	0.578	0.000	0.000	0.00	0.00
4.72	0.573	0.578	0.000	0.000	0.00	0.00

approaches OGE conditions, indicating a greater stability of the measurements, as also confirmed by the percentage errors reported in Table 5.8.

For the isolated duct, Figure 5.28(b), which represents the most unstable component of the system, high standard deviation values are observed mainly for small h/R values, while for larger h/R the deviations are smaller, yet still higher than those of the propeller. This behavior is due both to the intrinsic instability of the duct and to the criterion used for data extraction, which involves discarding the same initial portion of the transient for all heights. For larger h/R values, this interval does not fully include the quasi-steady phase, resulting in an apparently higher standard deviation, Table 5.9.

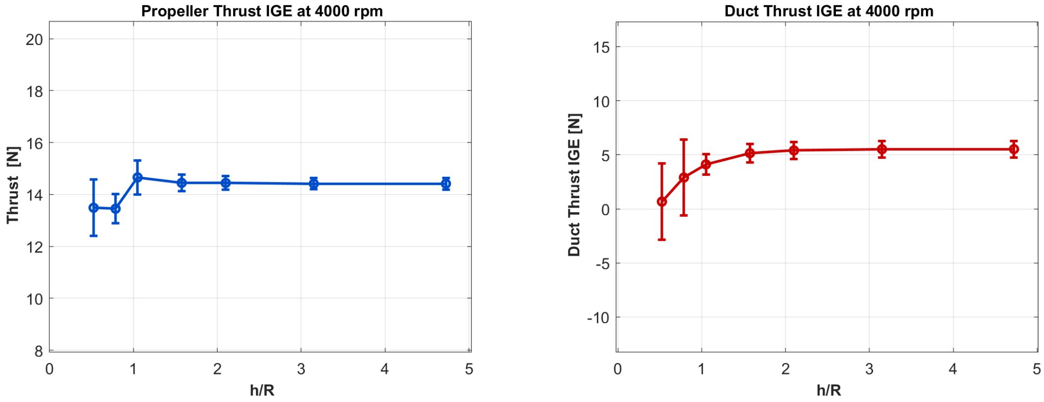

(a) Propeller

(b) Duct

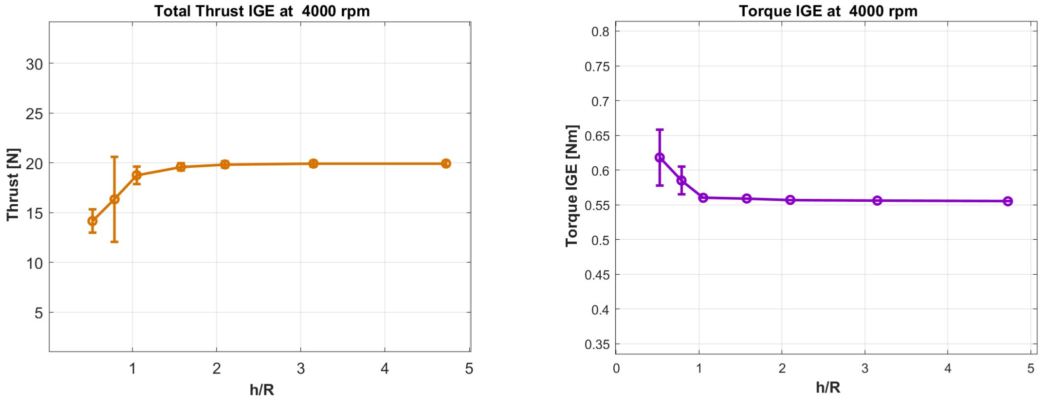

(c) Total

(d) Torque

Figure 5.28: Standard deviations at 4000 rpm as a function of the h/R ratio of the thrust for the propeller (a), duct (b), total system (c), and torque (d)

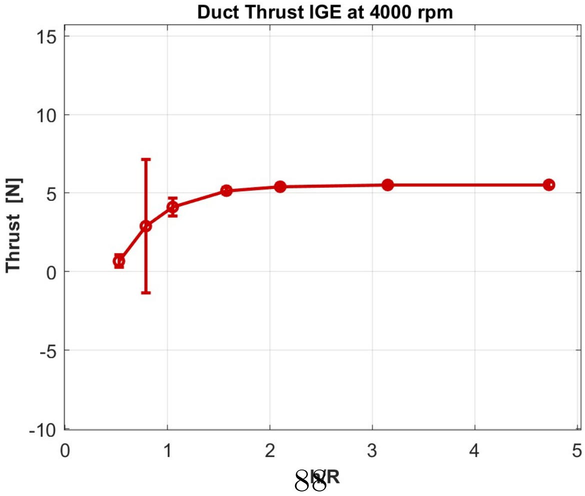

Figure 5.29: Duct standard deviation at 4000 rpm considering only the quasi-steady portion, showing reduced deviations at higher h/R due to increased stability.

For clarity, a second graph, Figure 5.29, was created showing the standard deviation of the duct considering only the portion in the quasi-steady regime, without the initial transient part. Compared to the previous results, where the same discard criterion was applied for all heights, this graph clearly shows that the deviations decrease as the height from the ground increases, demonstrating that for high h/R values the results are indeed more stable, Table 5.12.

Table 5.12: Duct thrust with standard deviations and percentage errors, cosidering only the quas-stead

h/R	T_{IGE}	T_{OGE}	SD_{IGE}	SD_{OGE}	err%$_{\text{IGE}}$	err%$_{\text{OGE}}$
0.52	0.700	5.398	0.390	0.060	55.71	1.11
0.79	2.897	5.398	4.240	0.060	146.36	1.11
1.05	4.110	5.398	0.570	0.060	13.87	1.11
1.57	5.150	5.398	0.200	0.060	3.88	1.11
2.10	5.402	5.398	0.170	0.060	3.15	1.11
3.15	5.515	5.398	0.170	0.060	3.08	1.11
4.72	5.522	5.398	0.170	0.060	3.08	1.11

The standard deviation of the torque is very low, as shown in Figure 5.28(d), and it becomes negligible for $h/R \geq 1.05$, as reported in Table 5.11.

In conclusion the analysis of the standard deviations shows that ground effect influences the different components of the setup in distinct ways. The propeller exhibits good stability as h/R increases, while the duct is the most sensitive element, with pronounced fluctuations at low heights. Torque deviations are very small and tend to vanish under OGE conditions. Overall, the results confirm the instability associated with the duct and the reduction of oscillations as the interaction with the ground decreases.

Wake and Velocity Field Visualization

As for the OGE conditions, wake visualizations are also reported for the IGE case at four different heights above the ground: $h/R = 0.525$, $h/R = 1.05$, $h/R = 2.1$, and $h/R = 4.73$. For each case, the figure on the left shows the velocity streamlines colored according to their magnitude, while the images on the right display the velocity component along the z direction. Because the velocity magnitudes vary widely between cases, different color scales were used to allow meaningful comparisons.

At the smallest distance, $h/R = 0.525$ (Figure 5.30(a)), intense flow circulations can be observed, with a wall jet spreading widely along the sides. In the second case, $h/R = 1.05$ (Figure 5.30(c)), the wall jet is less extended, making it easier to identify the internal flow recirculation region that cannot expand laterally. These effects gradually weaken for larger clearances, approaching the OGE conditions at $h/R = 4.73$ (Figure 5.31(c)).

Observing the images on the right, it can be seen that, with respect to the ground centerline, the velocity distributions are symmetric, showing opposite color intensities that reflect the reversed sign of the velocity while maintaining equal magnitude.

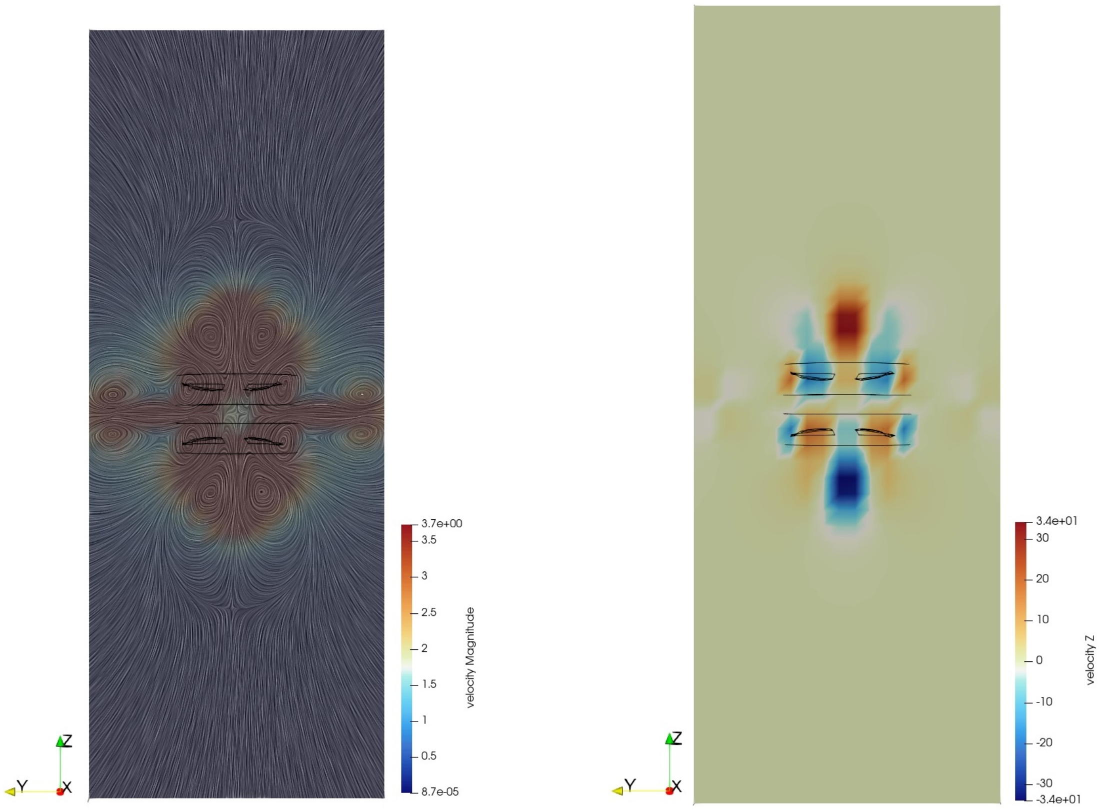

(a) h/R=0.525

(b) h/R=0.525

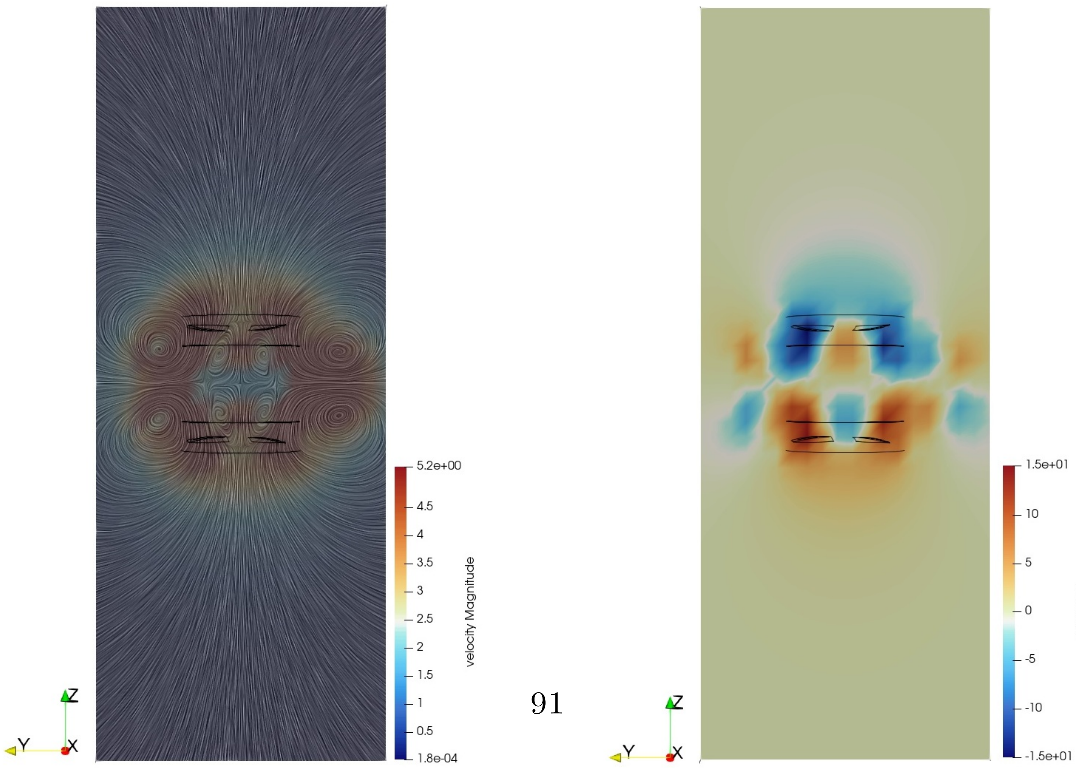

(c) h/R=1.05

(d) h/R=1.05

Figure 5.30: Comparison of individual contributions to the thrust ratio for the three configurations (a), (b), (c) and of the torque ratio (d).

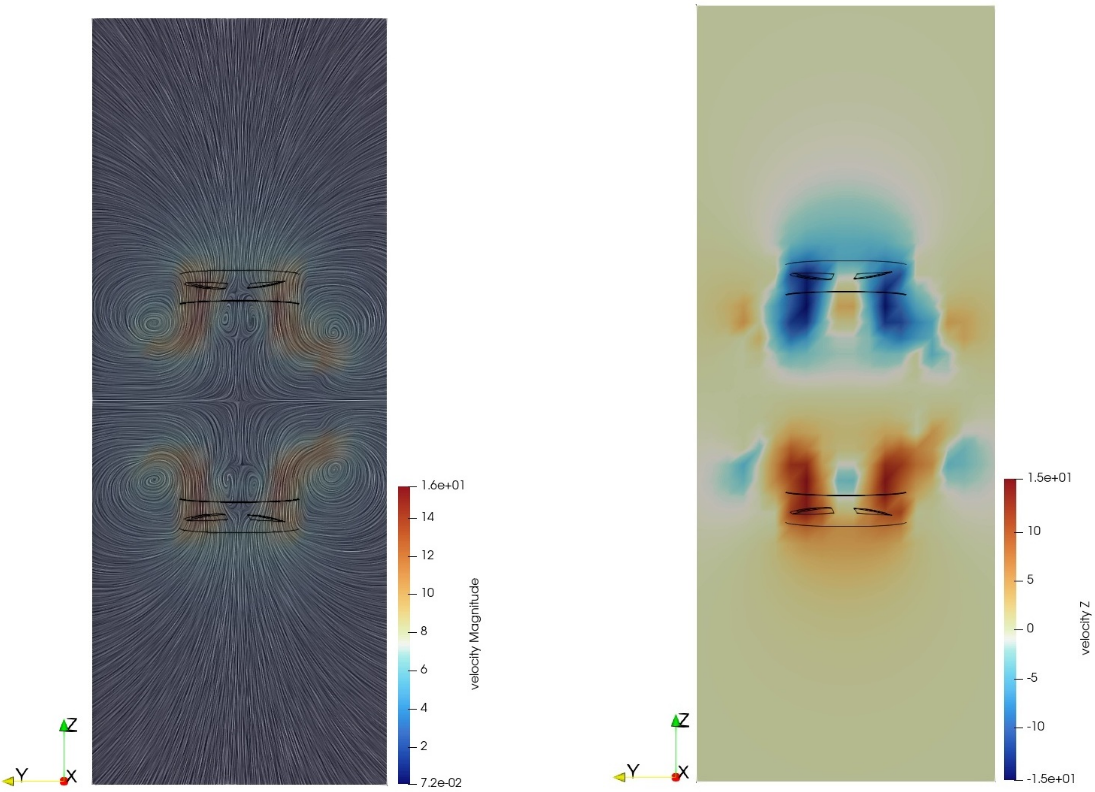

(a) h/R=2.1

(b) h/R=2.1

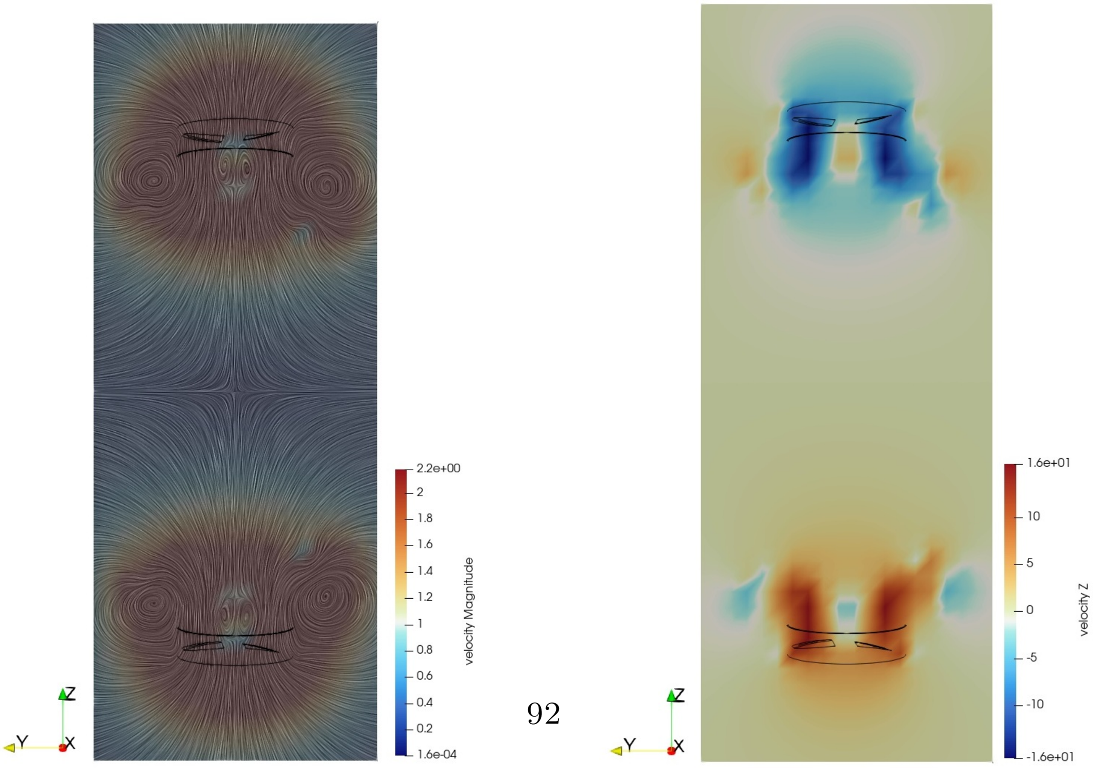

(c) h/R=4.73

(d) h/R=4.73

Figure 5.31: Comparison of individual contributions to the thrust ratio for the three configurations (a), (b), (c) and of the torque ratio (d).

Chapter 6

Experimental Analysis

Previous experimental studies on ground effect, as well as findings reported in the literature, show noticeable discrepancies regarding the behavior of ducted rotors near the ground—specifically, whether the presence of the duct leads to an increase or a decrease in thrust as the rotor approaches the ground. This uncertainty makes it essential to perform dedicated experiments on the present setup, in order to obtain data that can be directly compared with the numerical results.

Ideally, the experimental tests would be carried out directly on the Hovera drone; however, this is rather complex, as it requires longer implementation times and the current state of the drone does not allow reliable data measurements, also requiring the development of a control system. For this reason, the experiments were conducted on a model of much smaller dimensions than the Hovera. Although not a scaled model of the drone, the setup reproduces two key elements: the APC 15x13.5 three-bladed propeller and a duct specifically designed for this experiment. As previously mentioned, this study represents a continuation of a previous one involving an open propeller, with the aim of investigating the effects introduced by the addition of the duct.

This chapter is organized as follows: in the first part, the propeller used and its characteristics, as provided by the manufacturer, are described. Then, the experimental setup is presented, including the instrumentation and testing procedure. Finally, the experimental results obtained with the addition of the duct are presented and analyzed, with comparisons to the relevant theories and previously obtained numerical predictions, in order to highlight the effects of the ducted configuration.

6.1 Propeller characteristics and manufacturer data

The propeller used is an APC 15x13.5 three-blade propeller, which has a diameter of 15 inches and a pitch of 13.5 inches, it allows achieving a high tip Reynolds number without requiring excessively high power levels that would be difficult to manage. APC propellers are often chosen for experimental studies due to their standardized specifications and ready availability.

Figure 6.1: APC three blades propeller 15x13.5, ref [36].

The data provided by the manufacturer, including geometric properties and mass, are presented in Table 6.1. Detailed geometric characteristics, such as twist angles and chord lengths at several stations along the propeller, are reported in Table 6.2, highlighting the main values relevant for this work.

Performance data for different propeller rotational speeds and advance ratios J are available from [36]; in our case, for the ground effect, we will use J = 0. Table 6.2 shows the extrapolated values of Thrust, Torque, and Power in the units of interest for rotational speeds ranging from 1000 to 9000 RPM, with rows corresponding to J = 0.

Table 6.1: Main specifications of the propeller in inches and millimeters, ref [36].

Specification	Value (in.)	Value (mm)
Pitch	13.5	343
Propeller Diameter	15	381
Hub Diameter	1.50	38.1
Hub Thickness	0.63	16.0
Shaft Diameter	5/16	7.94
Product Weight	3.39 oz	96.1 g

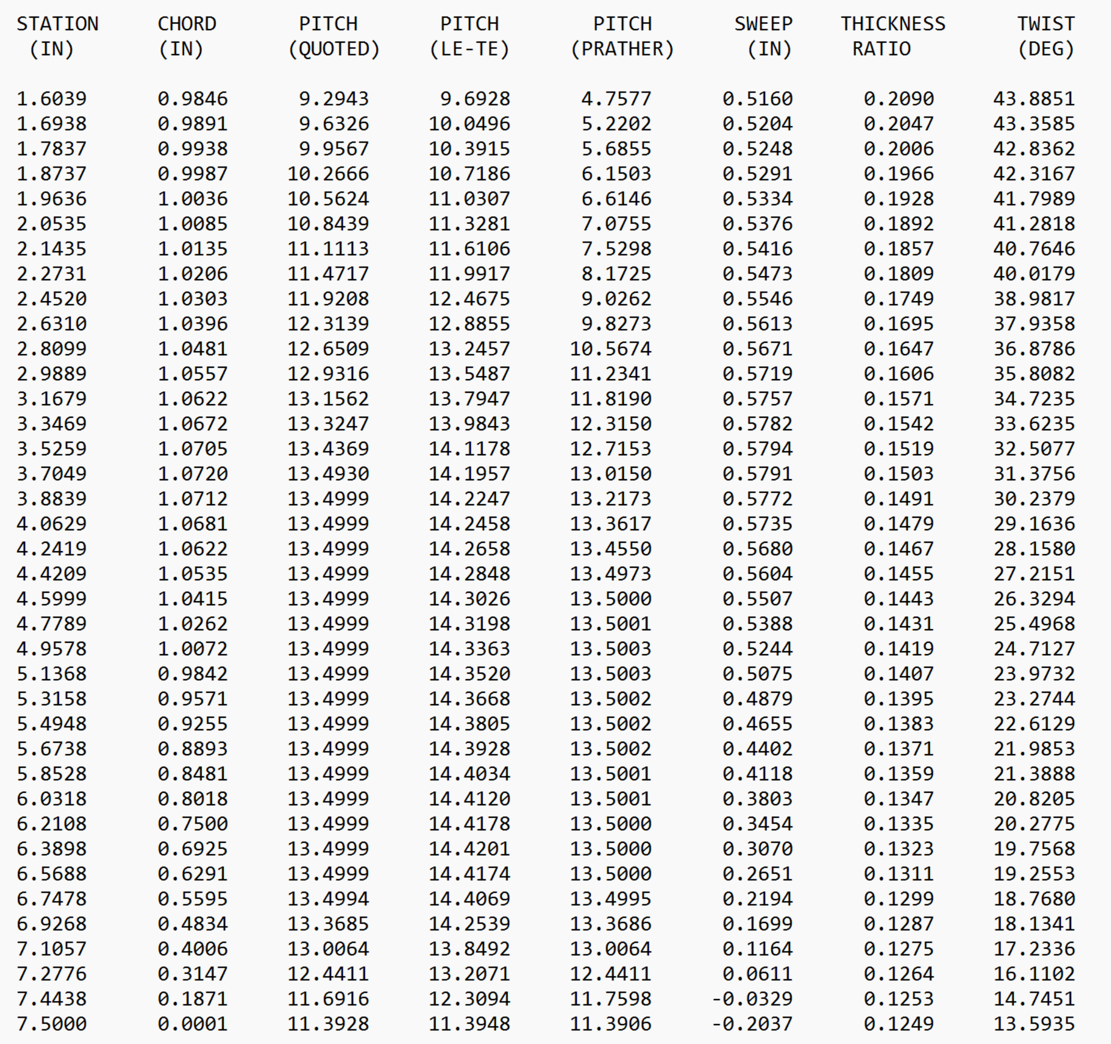

STATION (IN)	CHORD (IN)	PITCH (QUOTED)	PITCH (LE-TE)	PITCH (PRATHER)	SWEEP (IN)	THICKNESS RATIO	TWIST (DEG)
1.6039	0.9846	9.2943	9.6928	4.7577	0.5160	0.2090	43.8851
1.6938	0.9891	9.6326	10.0496	5.2202	0.5204	0.2047	43.3585
1.7837	0.9938	9.9567	10.3915	5.6855	0.5248	0.2006	42.8362
1.8737	0.9987	10.2666	10.7186	6.1503	0.5291	0.1966	42.3167
1.9636	1.0036	10.5624	11.0307	6.6146	0.5334	0.1928	41.7989
2.0535	1.0085	10.8439	11.3281	7.0755	0.5376	0.1892	41.2818
2.1435	1.0135	11.1113	11.6106	7.5298	0.5416	0.1857	40.7646
2.2731	1.0206	11.4717	11.9917	8.1725	0.5473	0.1809	40.0179
2.4520	1.0303	11.9208	12.4675	9.0262	0.5546	0.1749	38.9817
2.6310	1.0396	12.3139	12.8855	9.8273	0.5613	0.1695	37.9358
2.8099	1.0481	12.6509	13.2457	10.5674	0.5671	0.1647	36.8786
2.9889	1.0557	12.9316	13.5487	11.2341	0.5719	0.1606	35.8082
3.1679	1.0622	13.1562	13.7947	11.8190	0.5757	0.1571	34.7235
3.3469	1.0672	13.3247	13.9843	12.3150	0.5782	0.1542	33.6235
3.5259	1.0705	13.4369	14.1178	12.7153	0.5794	0.1519	32.5077
3.7049	1.0720	13.4930	14.1957	13.0150	0.5791	0.1503	31.3756
3.8839	1.0712	13.4999	14.2247	13.2173	0.5772	0.1491	30.2379
4.0629	1.0681	13.4999	14.2458	13.3617	0.5735	0.1479	29.1636
4.2419	1.0622	13.4999	14.2658	13.4550	0.5680	0.1467	28.1580
4.4209	1.0535	13.4999	14.2848	13.4973	0.5604	0.1455	27.2151
4.5999	1.0415	13.4999	14.3026	13.5000	0.5507	0.1443	26.3294
4.7789	1.0262	13.4999	14.3198	13.5001	0.5388	0.1431	25.4968
4.9578	1.0072	13.4999	14.3363	13.5003	0.5244	0.1419	24.7127
5.1368	0.9842	13.4999	14.3520	13.5003	0.5075	0.1407	23.9732
5.3158	0.9571	13.4999	14.3668	13.5002	0.4879	0.1395	23.2744
5.4948	0.9255	13.4999	14.3805	13.5002	0.4655	0.1383	22.6129
5.6738	0.8893	13.4999	14.3928	13.5002	0.4402	0.1371	21.9853
5.8528	0.8481	13.4999	14.4034	13.5001	0.4118	0.1359	21.3888
6.0318	0.8018	13.4999	14.4120	13.5001	0.3803	0.1347	20.8205
6.2108	0.7500	13.4999	14.4178	13.5000	0.3454	0.1335	20.2775
6.3898	0.6925	13.4999	14.4201	13.5000	0.3070	0.1323	19.7568
6.5688	0.6291	13.4999	14.4174	13.5000	0.2651	0.1311	19.2553
6.7478	0.5595	13.4994	14.4069	13.4995	0.2194	0.1299	18.7680
6.9268	0.4834	13.3685	14.2539	13.3686	0.1699	0.1287	18.1341
7.1057	0.4006	13.0064	13.8492	13.0064	0.1164	0.1275	17.2336
7.2776	0.3147	12.4411	13.2071	12.4411	0.0611	0.1264	16.1102
7.4438	0.1871	11.6916	12.3094	11.7598	-0.0329	0.1253	14.7451
7.5000	0.0001	11.3928	11.3948	11.3906	-0.2037	0.1249	13.5935

Figure 6.2: Geometric Data – APC Propeller 15×13.5 ref [36].

Table 6.2: Propeller performance data for different RPM with J=0, ref [36].

RPM	C_T	C_P	P (W)	Q (Nm)	T (N)	Mach	Re
1000	0.1539	0.0879	4.007	0.038	1.104	0.06	23168
2000	0.1547	0.0795	28.982	0.138	4.439	0.12	46336
3000	0.1551	0.0761	93.611	0.298	10.016	0.18	69503
4000	0.1554	0.0742	216.513	0.517	17.846	0.24	92669
5000	0.1558	0.0731	416.623	0.796	27.947	0.30	115834
6000	0.1561	0.0725	713.437	1.135	40.339	0.36	138997
7000	0.1565	0.0721	1127.234	1.538	55.045	0.42	162158
8000	0.1570	0.0720	1679.331	2.005	72.092	0.48	185318
9000	0.1574	0.0720	2392.360	2.538	91.507	0.54	208475

6.2 Experimental setup and instrumentation

The aim is to set up an experimental configuration that allows the evaluation of the effects of the duct on the propeller in OGE and of the entire system in IGE. What will be described is the same experiment carried out by my colleague, but with the addition of the components necessary for this work.

The experiment is conducted inside the wind tunnel at the RMIT laboratories, in a climate-controlled indoor facility large enough to avoid boundary interference. Figure 6.3 shows pictures of the entire system, which can be divided into two groups: a fixed group and a movable group. The fixed group is mounted on the floor using screws and consists of the load cell, to which the motor and propeller are sequentially attached, and the duct, held in the desired position relative to the propeller by two fixed supports anchored to the base. The propeller is positioned at a height of 0.8 m above the floor, more than twice its diameter, thus avoiding interactions between the flow and the ground.
The second part of the setup consists of a vertical wall measuring 1.6 × 1.6 m, obtained by joining two foam blocks attached to a tubular aluminum frame that holds it in place. A movable vertical wall was chosen instead of a horizontal one because it is easier to reposition, and the distances at which it will be placed from the first group are marked on the floor with masking tape.
The experimental configuration is designed to allow: 1) Variation of the distance between the propeller and the vertical plane representing the ground 2) Adjustment of the rotational speed 3) Easy removal or addition of the duct.

The parts involved in the experimental setup therefore include a load cell, a motor, a duct, the propeller, a DC power supply and a vertical wall. The following elements are now described in detail to make the experiment fully replicable.

Load Cell

Thrust and torque are measured using a Flight Stand 15 load cell from Tyto Robotics, a six-axis device capable of covering a thrust range (T_x, T_y, T_z) of ±150 N and a torque range (Q_x, Q_y, Q_z) of 8 Nm, suitable for the force and torque measurements expected from the propeller data provided by the manufacturer and from the numerical simulations. Figure 6.4 shows this instrument, whose full CAD, from Ref. [37], is provided in the appendix.
Equipped with an optical sensor for RPM measurement, the system allows a very wide rotational speed range, with the values used in this experiment being much lower than the maximum of 30000 rpm, and requires a voltage from 0 to 180 V and a current from 0 to 150 A.

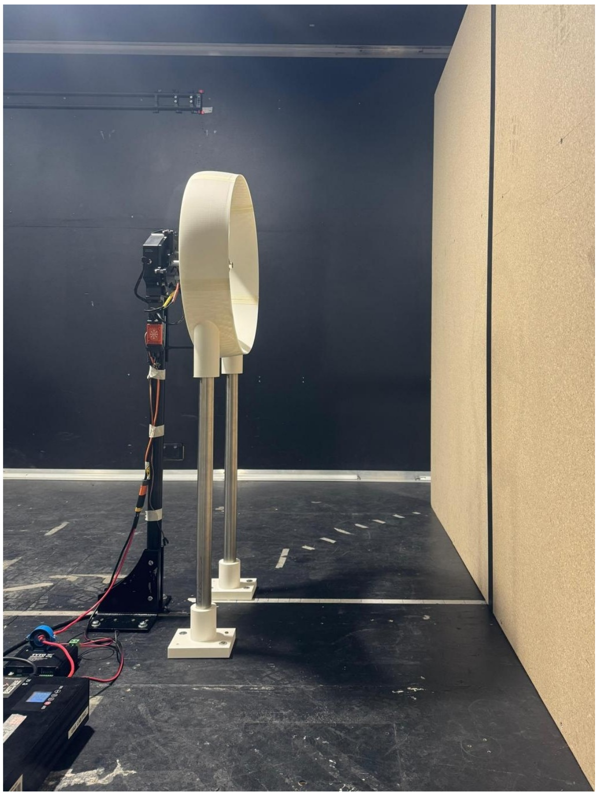

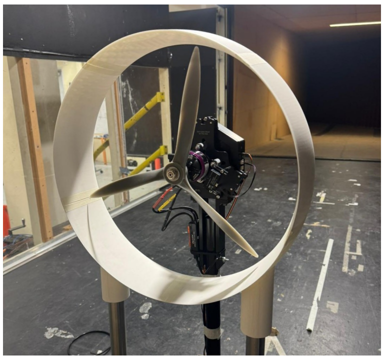

(b) Ducted on the front

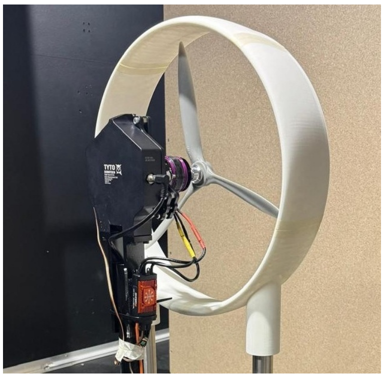

(a) Overall setup with instrumentation

(c) Ducted on the back

Figure 6.3: Photographs of the experimental setup: (a) overall view, (b) ducted configuration on the front, and (c) ducted configuration on the back.

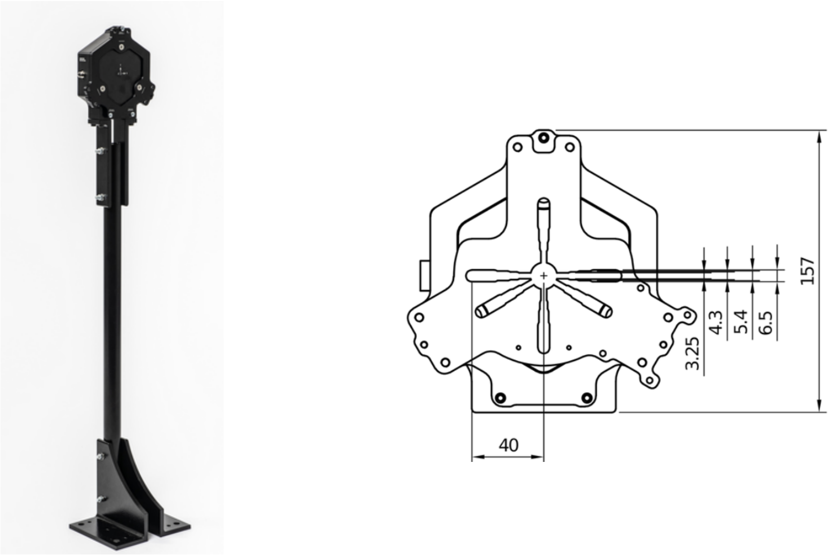

Figure 6.4: Front view of the load cell assembly: left image shows Flight Stand 15 load cell, right image shows detailed component in front view, ref [37].

The insert at the front part, shown in Figure 6.4, allows the motor to be mounted, and the system ensures that the propeller is positioned at the center of the vertical wall.

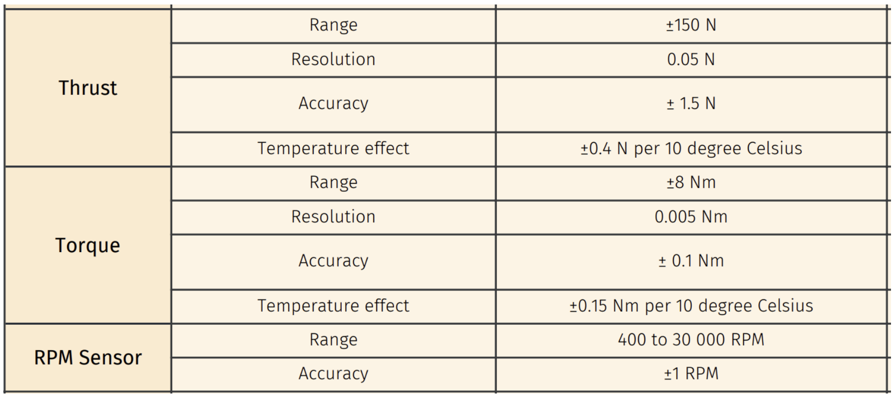

Thrust	Range	±150 N
	Resolution	0.05 N
	Accuracy	± 1.5 N
	Temperature effect	±0.4 N per 10 degree Celsius
Torque	Range	±8 Nm
	Resolution	0.005 Nm
	Accuracy	± 0.1 Nm
	Temperature effect	±0.15 Nm per 10 degree Celsius
RPM Sensor	Range	400 to 30 000 RPM
	Accuracy	±1 RPM

Figure 6.5: Datasheet Load Cell, ref [37].

Motor

For the selection of the motor, it was first necessary to perform an engine sizing using the actuator disk model, based on the power, thrust, and torque requirements of the propeller at a rotational speed of 6000 RPM, which is higher than the maximum speed that will be reached during the experimental phase. The rotor disk area is:

$$A = \pi R^2 = \pi \cdot (0.1905)^2 \approx 0.1140\ m^2$$

The ideal induced velocity is:

$$v_i = \sqrt{\frac{T}{2\rho A}} = \sqrt{\frac{40.339}{2 \cdot 1.225 \cdot 0.1140}} \approx 12 m/s$$

The ideal induced power is:

$$P_i = T \cdot v_i = 40.339 \cdot 12 \approx 484W$$

In an actuator disk model, a correction factor is introduced to account for non-ideal losses:

$$P_{shaft} \approx (1.25 \div 1.5) \cdot P_i \approx 605 \div 726W$$

A similar value is reported by the manufacturer.

Another point to consider is that not all the power delivered by the motor to the propeller is converted into useful propulsive power; therefore, a motor efficiency of

$\eta \approx 80\%$ is assumed and a 6S LiPo battery ($V \approx 22.2V$) is used:

$$P_{el} = \frac{P_{shaft}}{\eta} = 907.5W$$

Taking into account the power estimate just performed, an A50-16S V4 motor was selected, with its specifications shown in Figure 6.6. This motor can be easily connected to the load cell, and the motor shaft is inserted into the propeller.

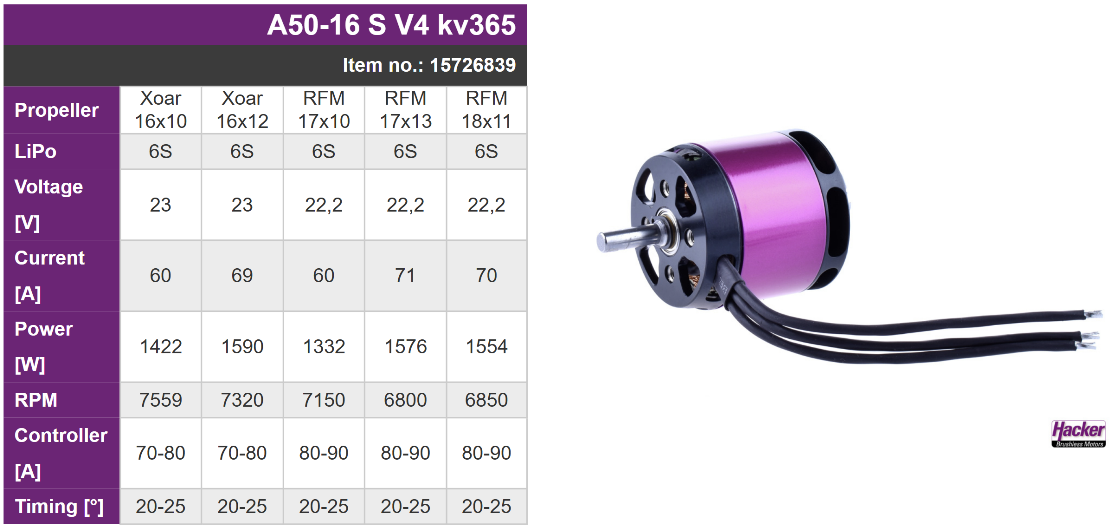

A50-16 S V4 kv365

Item no.: 15726839

Propeller	Xoar 16x10	Xoar 16x12	RFM 17x10	RFM 17x13	RFM 18x11
LiPo	6S	6S	6S	6S	6S
Voltage [V]	23	23	22,2	22,2	22,2
Current [A]	60	69	60	71	70
Power [W]	1422	1590	1332	1576	1554
RPM	7559	7320	7150	6800	6850
Controller [A]	70-80	70-80	80-90	80-90	80-90
Timing [°]	20-25	20-25	20-25	20-25	20-25

Figure 6.6: Overview of the motor: table of specifications (left) and photo of the Hacker A50-16S V4 motor (right), ref [38].

The motor, as well as all other electronic components, given the low power and voltage levels involved, is powered directly by a DC power supply connected to the laboratory mains.

Duct

The duct was modeled in SolidWorks as a rotational solid generated by revolving a NACA 0018 profile, based on the design used by [20] in their experimental tests. As specified before the duct dimensions were chosen so that the internal diameter provides a clearance equal to 2.9% of the propeller radius consequently, the internal diameter is 390.9 mm, while the external diameter measures 427 mm. Moreover, the chord of the duct is 100 mm to allow the system to be positioned at a reduced distance from the wall. The duct has two extensions at the bottom with holes that allow two 509 mm tubes to be inserted, which in turn are mounted in two supports anchored to the floor.

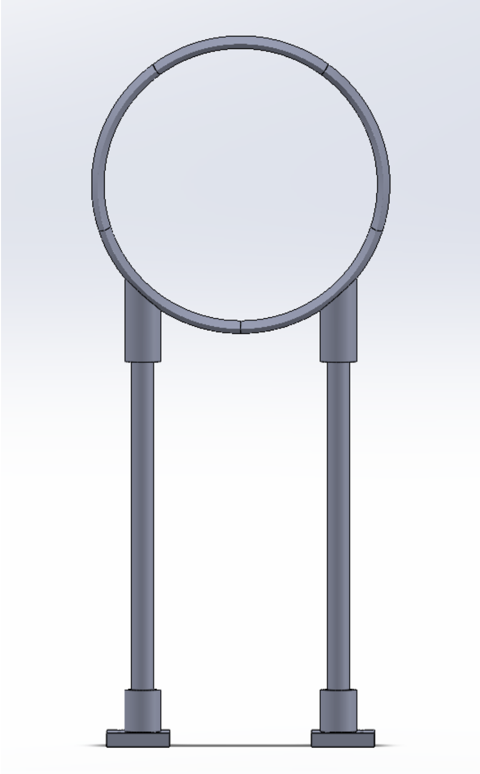

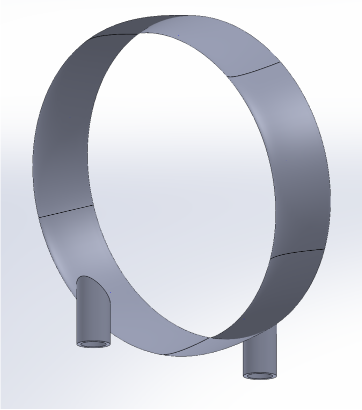

(b) Duct structure only

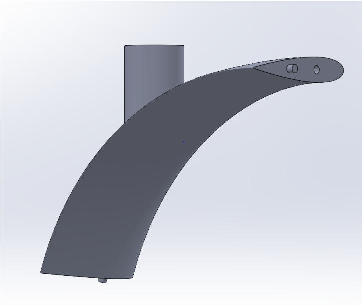

(a) Complete duct assembly with supports

(c) Mounting interface detail

Figure 6.7: Overall view of the duct system and support integration.

Both the duct and the support were 3D-printed in Polylactic Acid (PLA) using a Bambu Lab 3D printer with a 0.4 mm nozzle diameter. Given that the duct dimensions exceeded the printer's build volume, the CAD model was divided into five parts, and for each of them inserts were created to allow assembly without the need for glue or screws.

6.3 Testing procedures

The measurements were carried out in two stages: first with the ducted-propeller in out-of-ground-effect (OGE) conditions and subsequently in-ground-effect (IGE) conditions, in order to evaluate the presence of the duct on aerodynamic performance and the influence of ground proximity..

The motor rotational speed was controlled electronically through a predefined throttle sequence (Fig. 6.8). The procedure began by experimentally determining the throttle values corresponding to specific motor speeds. Once the correct values were identified, an automatic speed control was implemented. The control sequence consisted of assigning each throttle value a start time, ensuring a gradual transition from the system being inactive to reaching the target speeds. The values of interest were 1180, 1240, and 1320, corresponding approximately to 3000, 4000, and 5000 RPM, respectively. The initial and final phases of the sequence ensured smooth acceleration and deceleration, minimizing transient effects in the measurements, while the use of different rotational speeds enabled the acquisition of load data down to 1500 RPM.

Measurements were initially carried out in OGE and subsequently in IGE at the following distances between the propeller and the wall: 0.10 m, 0.15 m, 0.20 m, 0.30 m, 0.40 m, 0.60 m, and 0.90 m, corresponding respectively to h/R=0.525, 0.787, 1.05, 1.78, 2.1, 3.15, 4.73. Multiple repetitions were performed at each test condition to assess measurement repeatability, resulting in a total of 4 tests in OGE and 28 in IGE.

Measurements were recorded after the system reached steady-state conditions, and the acquired thrust and torque data were then analyzed to derive the corresponding nondimensional performance coefficients.

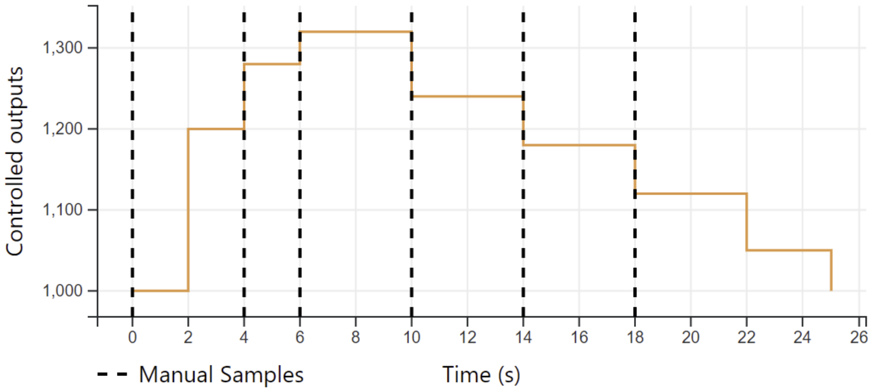

Figure 6.8: Automated throttle control sequence used during data acquisition.

6.4 Results

This section presents the experimental results, obtained by extracting the steady-state portions of the recorded signals while discarding the initial and final transients caused by throttle adjustments. The tests for each distance were repeated four times using the same automated throttle control sequence; however, slight variations in the achieved RPM values occurred between repetitions. To obtain consistent reference conditions, a linear regression was applied to estimate the thrust and torque at specific RPM values for both IGE and OGE configurations. The data processing was performed in MATLAB.

The section first recalls the main results from the previous open propeller experiments, and then analyzes the performance variations introduced by the presence of the duct under both OGE and IGE conditions.

It should be noted that the data obtained in this experiment do not measure the loads experienced by the duct or shrouded propeller system, but only reflect how the propeller performance varies, since it is the only component connected to the load cell.

6.4.1 Results from the previous Open propeller study

Figure 6.9 presents the experimental results for $T_{\mathrm{IGE}}/T_{\mathrm{OGE}}$ and $Q_{\mathrm{IGE}}/Q_{\mathrm{OGE}}$ for the open propeller case. At 3200 RPM, the thrust ratio increases as the propeller approaches the wall, whereas for the other speeds it tends to decrease after a nearly constant trend at low h/R ratios. This behavior is in good agreement with the numerical predictions, as illustrated in Figure 6.10. Similarly, the torque ratio follows the expected numerical trend, approaching a value of 1 in OGE, although slightly higher induced losses are observed in proximity to the ground.

6.4.2 Results OGE Shrouded Rotor

In the literature and from numerical simulations, it has been observed that the presence of the duct leads a slight reduction in thrust and an increase in torque for the propeller.

This behavior is also evident in the experimental thrust results, as shown in Table 6.3, with reductions ranging from -2.15% to -8.05% when moving from the OP to the SR configuration. Conversely, the torque exhibits a peculiar trend, with variations ranging from 0.39% to -2.80%.

It is interesting to note that, by overlaying the experimental results with the numerically obtained data, as shown in Figure 6.11, the two curves almost coincide with each other, thus validating the obtained results.

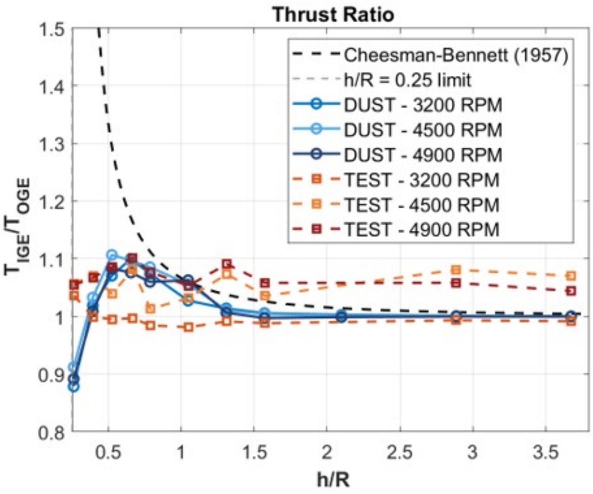

Figure 6.9: Experimental Results: $T_{\mathrm{IGE}}/T_{\mathrm{OGE}}$ vs h/R for the Open Propeller, ref previous work.

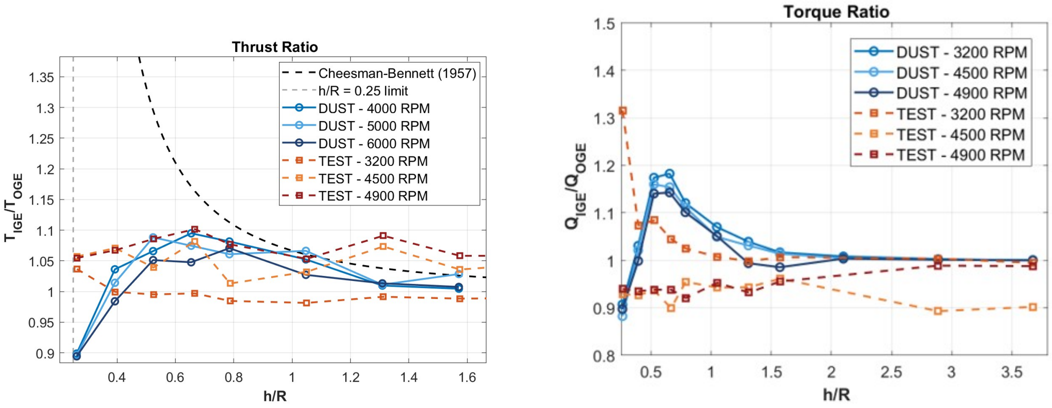

(a) Thrust ratio comparison

(b) Torque ratio comparison

Figure 6.10: Comparison of experimental (TEST) and numerical ($DUST$) results for the open propeller: (a) thrust ratio and (b) torque ratio as a function of nondimensional clearance h/R, ref previous work.

Table 6.4 shows, for selected RPM values, the percentage difference between numerical simulations and experimental results, with thrust errors below 12.33%,which decrease as the RPM increases, and torque errors below 7.62%.

This difference between numerical and experimental results may partly be due to the fact that, during assembly, the relative positions of the duct and the propeller were adjusted to avoid interference issues, and therefore may not have exactly matched

Table 6.3: Thrust and Torque for the OGE propeller at different RPM, with and without duct (experimental), and percentage difference between OP (REF) and SR.

	RPM	2600	3000	4000	4500	4900
OGE OP	Thrust [N]	/	/	16.051	21.013	25.029
(REF)	Torque [Nm]	/	/	0.59092	0.79288	0.90422
OGE SR	Thrust [N]	6.4931	8.8842	15.706	19.975	23.015
	Torque [Nm]	0.25613	0.34193	0.59325	0.75742	0.87891
Error [%]	Thrust	/	/	-2.15	-4.95	-8.05
From OP to SR	Torque	/	/	0.39	-4.45	-2.80

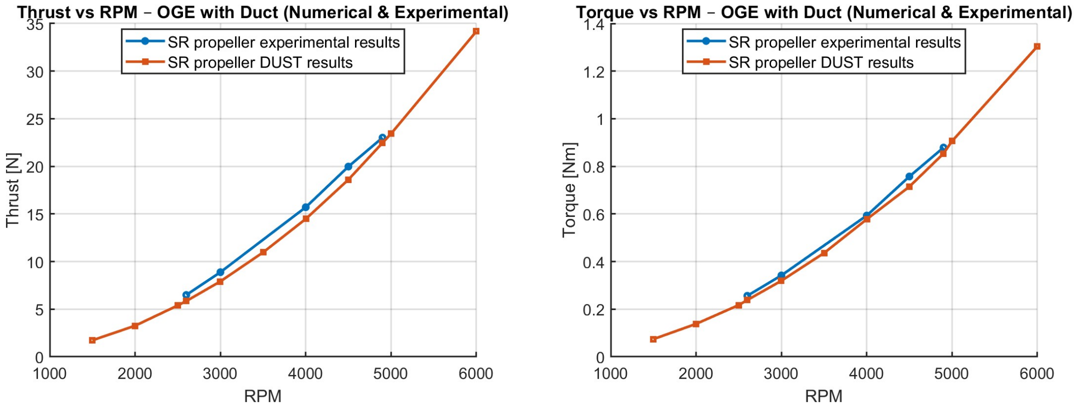

(a) Thrust comparison vs RPM (b) Torque comparison vs RPM

Figure 6.11: Comparison of experimental and numerical (*DUST*) results for the ducted propeller: (a) thrust and (b) torque as a function of RPM.

the configuration used in the simulations, resulting in the observed discrepancies.

Table 6.4: Percentage differences between propeller numerical and experimental results.

RPM	Thrust diff [%]	Torque diff [%]
2600	11.15	7.62
3000	12.33	7.19
4000	8.45	2.64
4500	7.48	6.08
4900	2.55	3.04

6.4.3 Results IGE Shrouded Rotor

In this paragraph, the experimental results are presented to illustrate how the performance of a ducted propeller changes as it approaches the ground.
Figure 6.12 (a) shows the trend of $T_{\text{IGE}}/T_{\text{OGE}}$ as a function of h/R for different RPM values. For most RPMs, the thrust ratio gradually increases as the rotor gets closer to the ground, reaching a maximum before slightly decreasing for $h/R \leq 0.8$. An exception is observed at 4900 RPM, where the thrust ratio remains nearly constant in this range. As h/R increases, the thrust ratio tends to stabilize, approaching unity and the corresponding out-of-ground-effect (OGE) values. For reference, the curve proposed by Cheeseman and Bennett is also shown, providing a benchmark from the literature, although it is not the most accurate model for the current setup.
Figure 6.12 (b) presents the corresponding torque ratio, $Q_{\text{IGE}}/Q_{\text{OGE}}$, which remains relatively monotonic and close to unity across all tested conditions, showing less pronounced variations compared to the thrust ratio.

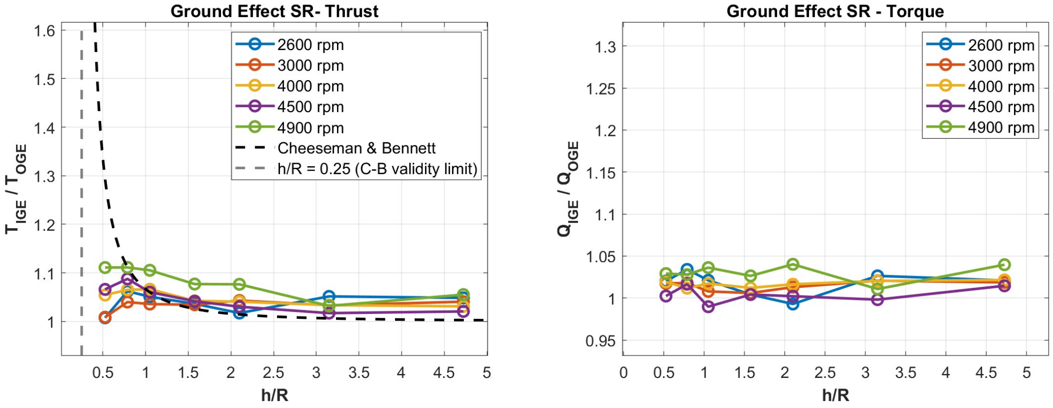

(a) Thrust ratio

(b) Torque ratio

Figure 6.12: Experimental comparison of thrust and torque ratios in ground effect (*IGE*) and out of ground effect (*OGE*) conditions for the ducted propeller at different RPM.

To allow a proper comparison, experimental and numerical results were reported at the same rotational speeds: 1500, 2000, 2500, and 3000 RPM. A good agreement is observed between the two datasets, particularly for thrust in regions close to the ground. Torque values from the numerical simulations are slightly underestimated compared to experimental measurements; however, at $h/R = 0.53$, the results are almost coincident. Figure 6.13 shows the overlay of experimental and numerical data, highlighting the consistency of the observed trends across both approaches.

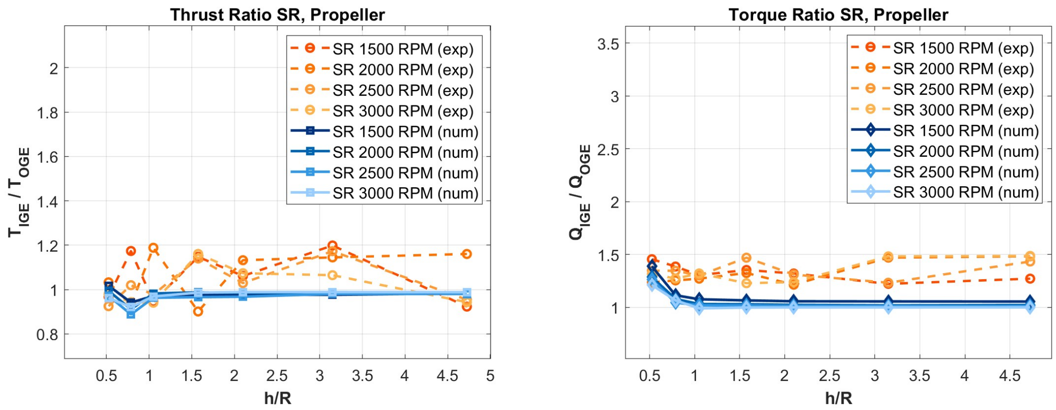

(a) Thrust ratio (b) Torque ratio

Figure 6.13: Comparison of Thrust and Torque Ratios in IGE for Ducted Propeller, Considering Only Propeller Data.

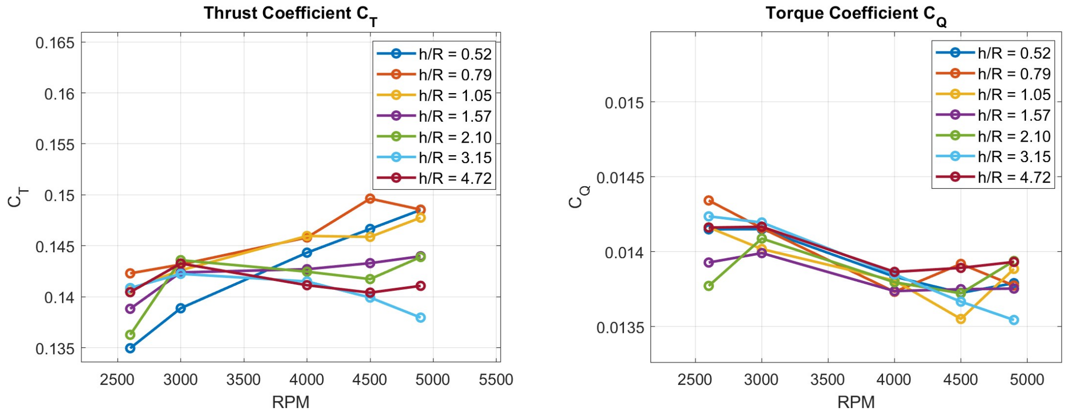

(a) Thrust Coefficient (b) Torque Coefficient

Figure 6.14: Comparison of Thrust and Torque Coefficient in IGE for Ducted Propeller, Considering Only Propeller Data.

Figure 6.14 shows the trends of the thrust and torque coefficients as a function of RPM for different h/R ratios, although they do not exhibit very regular patterns.

In general, considering both OGE and IGE results, it can be concluded that the experimental data are in good agreement with the numerical predictions, demonstrating the validity of the simulations performed with DUST. It is important to note, however, that the reported data refer only to the propeller, and not to the duct or the complete system. Therefore, further studies are needed to fully address this aspect and to further confirm the accuracy of the numerical results.

Chapter 7

Conclusions

This work investigated the aerodynamic behavior of small ducted propellers operating in proximity to the ground, with particular focus on the influence of the duct on thrust and torque generation. Both numerical and experimental approaches were employed to provide a comprehensive understanding of the system. The mid-fidelity vortex-based solver DUST was used to simulate the propeller behavior under various ground-clearance conditions, and the results were validated against measurements obtained in a controlled indoor environment. The study analyzed three propeller configurations, the baseline propeller, a halved propeller, and a helicopter-type rotor, considering both out-of-ground-effect (OGE) and in-ground-effect (IGE) conditions. Among these, special attention was given to the baseline propeller, as it represents the actual configuration tested experimentally and thus provides the most reliable data. The other two configurations were included for completeness, to investigate the influence of blade twist and to observe how geometrical modifications affect performance. The numerical analysis focused on the individual contributions of the propeller and duct, as well as their combined effect on total thrust and torque, in order to highlight the mechanisms underlying performance variations near the ground.

From the numerical analysis, the presence of the duct was found to have a significant and strongly condition-dependent influence on the aerodynamic performance of the propeller. The numerical simulations were also performed at different rotational speeds to assess the influence of RPM on performance. In general, higher RPM values resulted in greater total thrust and slightly higher torque, confirming that the observed trends are consistent across different operating conditions.

1. **Out of Ground Effect (OGE) conditions:** The duct provided a clear benefit, consistently increasing the total thrust compared to the isolated propeller. This improvement can be explained by the additional thrust generated by

the duct itself: the rotation of the blades induces a flow that creates pressure variations along the inner duct surface, resulting in a net force that contributes positively to the overall thrust.
Among the three numerical configurations, the baseline propeller exhibited similar propeller thrust values between the open and ducted cases. As a result, the increase in total thrust, up to about 50%, is mainly due to the duct contribution. In the halved-twist and helicopter-twist configurations, larger differences between the isolated and ducted propeller were observed, although the presence of the duct always resulted in an increase in total thrust.
A similar behavior was observed for torque, which changed only slightly across all three configurations, with the installation of the duct resulting in an increase in total torque of up to 18% in the baseline case.
Additionally, the thrust distribution per unit blade span was examined. The results highlight a noticeable increase in thrust near the blade tip when the duct is installed, which is consistent with the attenuation of tip-vortex-induced losses. Conversely, a reduction in thrust was observed in the inner blade region close to the hub. Providing a definitive explanation for this behavior would require further dedicated investigations, ideally supported by PIV measurements, which could not be performed within the limited timeframe of this work.

2. **In Ground Effect (IGE) conditions:** The numerical results showed a certain degree of variability; therefore, the reported values were obtained by averaging the simulations at each rotor-to-ground distance. The analysis was carried out for multiple rotor-to-ground heights, allowing the assessment of performance trends as a function of clearance.
The standard deviations, calculated for each component (propeller, duct, and total system), are larger near the ground and decrease significantly at higher h/R values. For the propeller, the results are relatively stable, with maximum errors of 8%. For the duct, simulations are highly unstable for $h/R < 1$, while for larger distances they become more consistent, and higher h/R values allow a reliable assessment of the duct contribution. Standard deviations for the torque are the lowest, indicating very limited variation compared to thrust.
Focusing on the baseline propeller, a clear decrease in the thrust ratio $T_{\text{IGE}}/T_{\text{OGE}}$ is observed as the rotor approaches the ground. A more pronounced reduction occurs for the duct loads, which begin decreasing for $h/R < 2$. As a result, the total thrust decreases in proximity to the ground, consistent with findings reported in the literature. In terms of torque, an increase in the ratio $Q_{\text{IGE}}/Q_{\text{OGE}}$ is observed near the ground, while for $h/R > 1$ the torque remains essentially constant. The halved-twist and helicopter rotor configurations exhibit different trends in both thrust and torque distributions

compared to the baseline propeller.

For the experimental investigation, only the effects of the duct in OGE and the ground in IGE on the propeller were measured, as it was the only part connected to the load cell. The tests were performed at rotational speeds consistent with those used in the numerical simulations to allow a direct comparison. The main findings for each scenario are summarized below and subsequently compared with the numerical results:

1. **OGE performance:** The addition of the duct generally resulted in a slight reduction of propeller thrust compared to the open propeller, consistent with trends observed in the numerical simulations. Torque variations were minor but followed a similar pattern, showing a slight increase or decrease depending on the RPM. Overall, the experimental thrust and torque data exhibit good agreement with the numerical predictions, with maximum deviations of approximately 12% for thrust and 7% for torque, validating the reliability of the simulation approach for OGE conditions.
2. **IGE performance:** As the propeller approached the ground, the thrust ratio $T_{\mathrm{IGE}}/T_{\mathrm{OGE}}$ increased for most RPM values, reaching a maximum before slightly decreasing at very low h/R values ($h/R \lesssim 0.8$). The torque ratio $Q_{\mathrm{IGE}}/Q_{\mathrm{OGE}}$ remained largely monotonic, with only minor deviations. These trends closely match the numerical results, particularly for thrust near the ground, while the torque ratio remains largely consistent with the simulations.
3. **Overall assessment:**The experimental results confirm the trends predicted by the DUST simulations, demonstrating that the numerical approach reliably captures the effects of both the duct and ground proximity on the propeller.

Future work will need to expand the experimental investigation to account for the loads on the duct as well as the complete ducted propeller system, enabling a thorough validation of the numerical simulations. Complementary analyses using techniques such as PIV would provide a more detailed understanding of the thrust distribution near the propeller hub. In addition, these studies, which have so far focused on a single propeller with duct, should be extended to the full Hovera configuration, incorporating appropriate modifications to the experimental setup to capture the integrated system behavior.

List of Figures

List of Acronyms and Symbols

Acronym	**Description**
IGE	In Ground Effect
OGE	Out of Ground Effect
$UAVs$	Unmanned Aerial Vehicles
$MAVs$	Micro or Miniature Air Vehicles
$HTOLS$	Horizontal Take-Off and Landing
$VTOLs$	Vertical Take-Off and Landing
$E-VTOL$	Electric Vertical Take-Off and Landing
RPM	Revolutions Per Minute
CV	Control Volume
PL	Power Loading
Re	Reynolds number
ADT	Actuator Disk Theory
BET	Blade Element Momentum Theory
$BEMT$	Blade Element Momentum Theory
AOA	Angle Of Attack
VRS	Vortex Ring State
EGE	Extreme Ground Effect
OP	Open Propeller
SR	Shrouded Rotor

Table 7.1: Acronyms used in this thesis

Symbol	**Description**
D	Rotor diameter
ω	Induced angular velocity
V	Velocity
A	Area
σ	Rotor solidity
β	Blade pitch angle
J	Advance ratio
n	Rotational speed
η	Efficiency
Ω	Angular velocity
T	Thrust
C_T	Thrust Coefficient
C_Q	Torque Coefficient
C_P	Power Coefficient
Q	Torque
P	Power
ρ	Density
p	Pitch
S	Space from rotors
m	Mass
F	Force
M	Momentum
$\dot{m}$	Mass flow rate
r	Radius
L	Lift
D	Drag
C_l	Lift coefficient
C_d	Drag coefficient
c	Chord
α	Angle of attack
ϕ	Blade angle
N	Number of blades
z	Height from ground
s	Semi-span
$Mach$	Mach number
t	Time
δ	Blade-duct tip clearence
θ	Twist
λ	Inflow ratio distribution

Table 7.2: Symbols used in this thesis

Chapter 8

Appendix

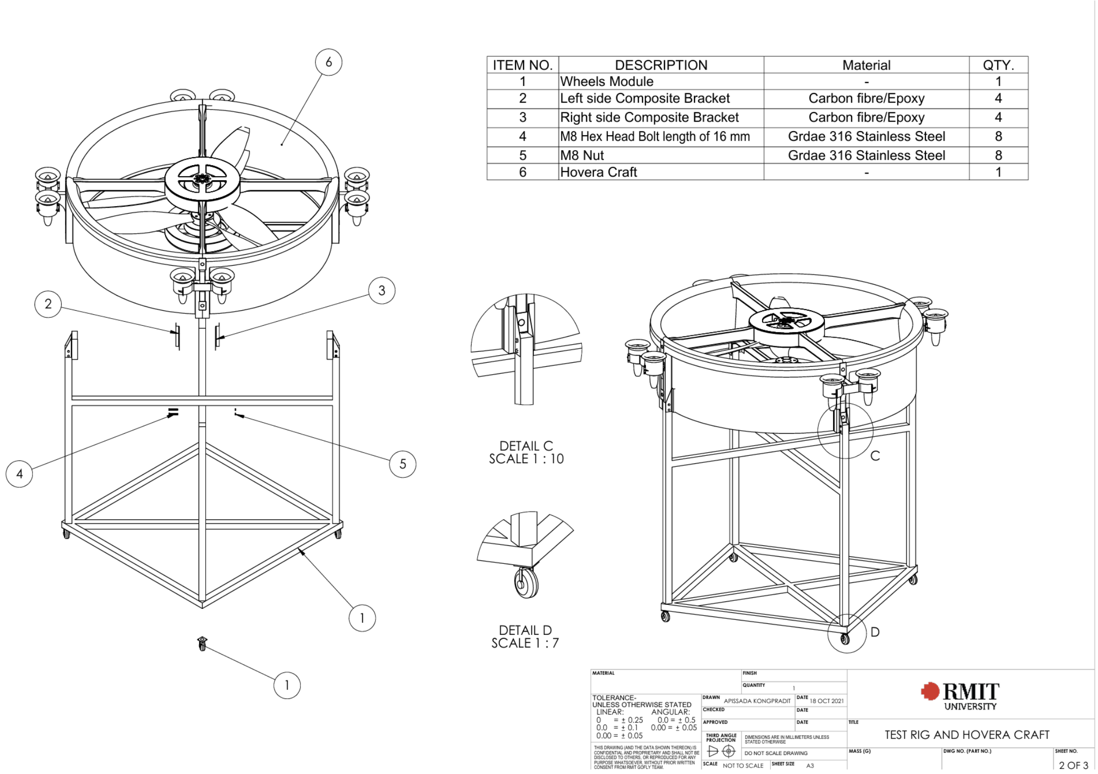

ITEM NO.	DESCRIPTION	Material	QTY.
1	Wheels Module	-	1
2	Left side Composite Bracket	Carbon fibre/Epoxy	4
3	Right side Composite Bracket	Carbon fibre/Epoxy	4
4	M8 Hex Head Bolt length of 16 mm	Grdae 316 Stainless Steel	8
5	M8 Nut	Grdae 316 Stainless Steel	8
6	Hovera Craft	-	1

Figure 8.1: CAD Test Rig, ref [7]

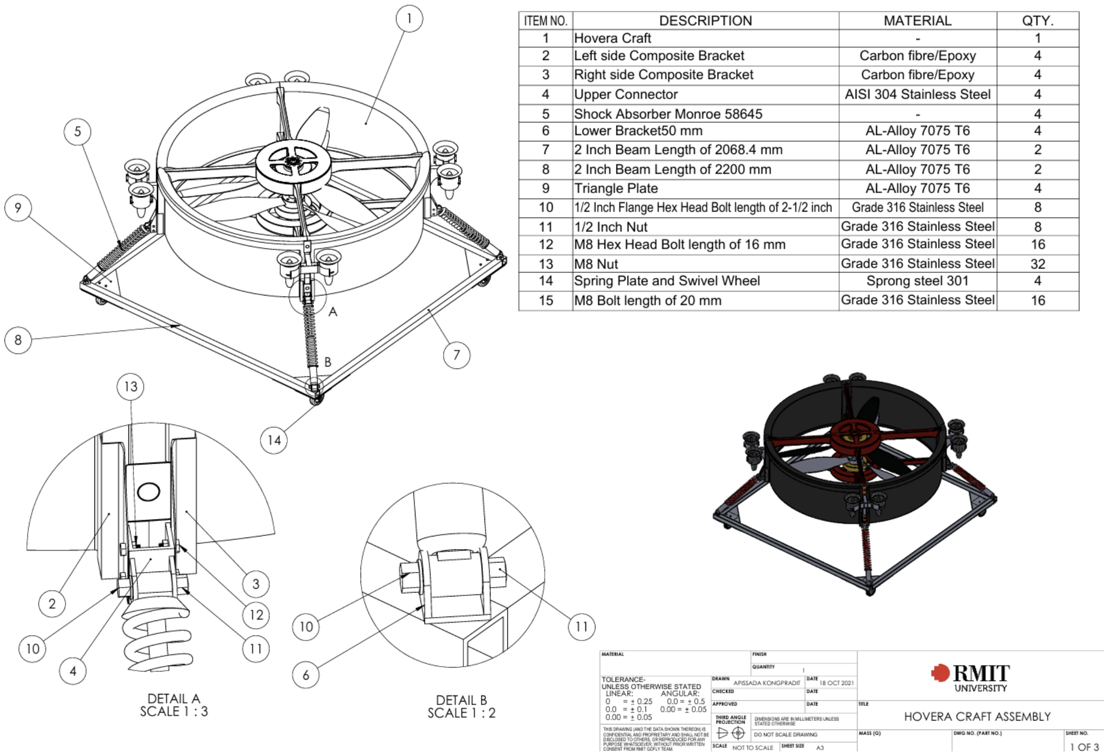

ITEM NO.	DESCRIPTION	MATERIAL	QTY.
1	Hovera Craft	-	1
2	Left side Composite Bracket	Carbon fibre/Epoxy	4
3	Right side Composite Bracket	Carbon fibre/Epoxy	4
4	Upper Connector	AISI 304 Stainless Steel	4
5	Shock Absorber Monroe 58645	-	4
6	Lower Bracket50 mm	AL-Alloy 7075 T6	4
7	2 Inch Beam Length of 2068.4 mm	AL-Alloy 7075 T6	2
8	2 Inch Beam Length of 2200 mm	AL-Alloy 7075 T6	2
9	Triangle Plate	AL-Alloy 7075 T6	4
10	1/2 Inch Flange Hex Head Bolt length of 2-1/2 inch	Grade 316 Stainless Steel	8
11	1/2 Inch Nut	Grade 316 Stainless Steel	8
12	M8 Hex Head Bolt length of 16 mm	Grade 316 Stainless Steel	16
13	M8 Nut	Grade 316 Stainless Steel	32
14	Spring Plate and Swivel Wheel	Sprong steel 301	4
15	M8 Bolt length of 20 mm	Grade 316 Stainless Steel	16

MATERIAL
FINISH
QUANTITY 1
TOLERANCE-
UNLESS OTHERWISE STATED
LINEAR: 0 = ± 0.25, 0.0 = ± 0.1, 0.00 = ± 0.05
ANGULAR: 0.0 = ± 0.5, 0.00 = ± 0.05
DRAWN APISSADA KONGPRADIT DATE 18 OCT 2021
CHECKED DATE
APPROVED DATE
THIRD ANGLE PROJECTION
DIMENSIONS ARE IN MILLIMETERS UNLESS STATED OTHERWISE
DO NOT SCALE DRAWING
THIS DRAWING (AND THE DATA SHOWN THEREON) IS CONFIDENTIAL AND PROPRIETARY AND SHALL NOT BE DISCLOSED TO OTHERS, OR REPRODUCED FOR ANY PURPOSE WHATSOEVER, WITHOUT PRIOR WRITTEN CONSENT FROM RMIT GOFLY TEAM.
SCALE NOT TO SCALE
SHEET SIZE A3
RMIT UNIVERSITY
TITLE HOVERA CRAFT ASSEMBLY
MASS (G)
DWG NO. (PART NO.)
SHEET NO. 1 OF 3

Figure 8.2: CAD Hovera Craft Assembly, ref [7]

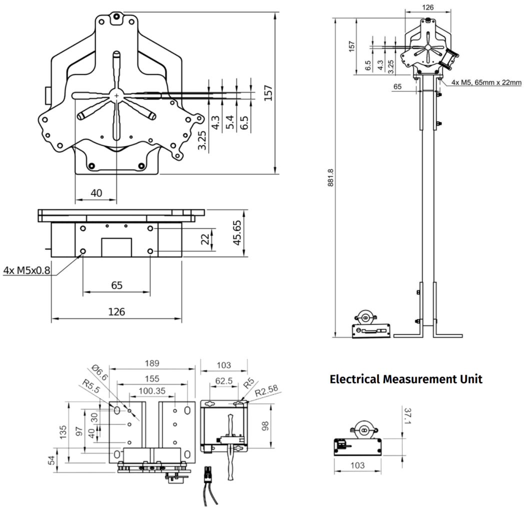

Figure 8.3: CAD model of the load cell assembly

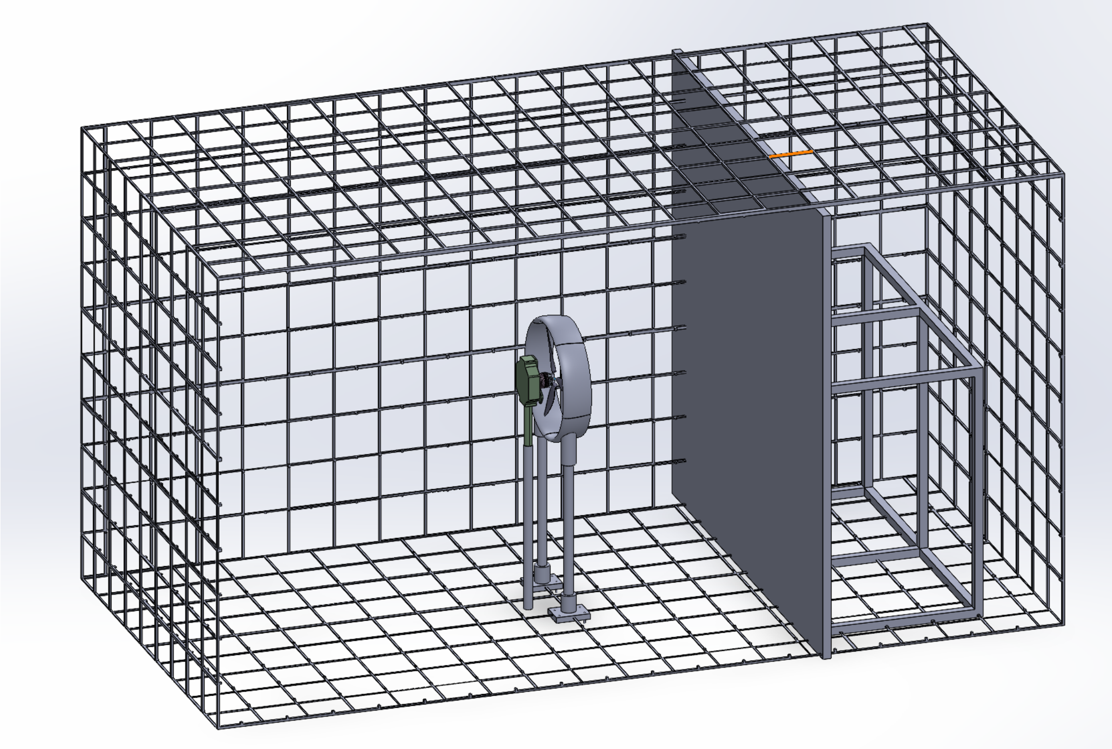

Figure 8.4: Overview of the CAD model of the entire test setup, enclosed here in a grid for greater clarity.

Bibliography

[1] Gabriel Georgiev, Filip Panayotov, Vladimir Serbezov, and Michael Todorov. «Experimental study of static characteristics of a helicopter rotor in ground effect». In: *AIP Conference Proceedings*. AIP Publishing, Jan. 2024. DOI: `10.1063/5.0186410` (cit. on pp. 1, 11, 42).

[2] Dario Floreano and Robert J. Wood. «Science, technology and the future of small autonomous drones». In: *Nature* 521.7553 (2015), pp. 460–466. DOI: `10.1038/nature14542` (cit. on p. 1).

[3] M. Hassanalian and A. Abdelkefi. «Classifications, applications, and design challenges of drones: A review». In: *Progress in Aerospace Sciences* 91 (2017), pp. 99–131. DOI: `10.1016/j.paerosci.2017.04.003` (cit. on pp. 1–3).

[4] S. A. Conyers, M. J. Rutherford, and K. P. Valavanis. «An empirical evaluation of ground effect for small-scale rotorcraft». In: *2018 IEEE International Conference on Robotics and Automation (ICRA)*. Brisbane, Australia: IEEE, May 2018 (cit. on pp. 3, 11–14, 26, 27, 43, 44).

[5] RMIT University. *Hovera Project – GoFly Competition*. Accessed: 24 August 2025. 2020. URL: `https://rmitgofly.wordpress.com/` (cit. on pp. 3, 5, 6).

[6] M. Tugnoli, D. Montagnani, M. Syal, G. Droandi, and A. Zanotti. «Midfidelity Approach to Aerodynamic Simulations of Unconventional VTOL Aircraft Configurations». In: 115 (2021), p. 106804. DOI: `10.1016/j.ast.2021.106804` (cit. on pp. 3, 62).

[7] RMIT University Hovera Team. *Hovera GoFly Final Report*. PDF report provided by the team. 2021 (cit. on pp. 7, 121, 122).

[8] Giuseppe Mangialomini. *L'elica - The Propeller: Principi di funzionamento e caratteristiche delle eliche*. 2011 (cit. on p. 8).

[9] P. E. Tanner, A. D. Overmeyer, L. N. Jenkins, C. S. Yao, and S. M. Bartram. «Experimental Investigation of Rotorcraft Outwash in Ground Effect». In: NF1676L-21054. May 2015. URL: `https://ntrs.nasa.gov/citations/20160006428` (cit. on pp. 11, 43).

[10] W. Johnson. *NDARC: NASA Design and Analysis of Rotorcraft.* Technical Publication NASA/TP-2009-215402. NASA, Dec. 2009, pp. 87–89. URL: `https://ntrs.nasa.gov/citations/20100021405` (cit. on p. 12).

[11] J. Lighthill. «A simple fluid-flow model of ground effect on hovering». In: *Journal of Fluid Mechanics* 93.4 (1979), pp. 745–758. DOI: `10.1017/S0022112079002393`. URL: `https://doi.org/10.1017/S0022112079002393` (cit. on pp. 12, 28, 29).

[12] Snorri Gudmundsson. «General Aviation Aircraft Design». In: *General Aviation Aircraft Design, Second Edition.* Second Edition. Butterworth-Heinemann, 2022, pp. 638–649. DOI: `10.1016/B978-0-12-818465-3.00015-X` (cit. on pp. 14, 15, 19, 20).

[13] Nikolas S. Zawodny, Noah H. Schiller, Nicole A. Pettingill, and Glenn L. Medina. *Aerodynamic and Acoustic Characterization of a Ducted Propeller in a Small Hover Anechoic Chamber.* Technical Memorandum NASA/TM-20250009190. Public document, Work of the U.S. Government, Public Use Permitted. Langley Research Center, Hampton, Virginia; Marshall Space Flight Center, Huntsville, Alabama: National Aeronautics and Space Administration (NASA), Sept. 2025. URL: `https://ntrs.nasa.gov/citations/20250009190` (cit. on pp. 16, 17, 36–38, 73, 74).

[14] Faisal Mahmuddin. «Rotor Blade Performance Analysis with Blade Element Momentum Theory». In: *Energy Procedia* 105 (2017). 8th International Conference on Applied Energy, ICAE2016, 8-11 October 2016, Beijing, China, pp. 1123–1129. ISSN: 1876-6102. DOI: `https://doi.org/10.1016/j.egypro.2017.03.477`. URL: `https://www.sciencedirect.com/science/article/pii/S1876610217305180` (cit. on p. 21).

[15] «Iterative BEMT analysis extended to model coaxial rotor aerodynamic performance in hover». In: *Aerospace Science and Technology* 161 (2025), p. 110122. ISSN: 1270-9638. DOI: `https://doi.org/10.1016/j.ast.2025.110122`. URL: `https://www.sciencedirect.com/science/article/pii/S1270963825001932` (cit. on pp. 21, 22).

[16] W. Z. Stepniewski. *Rotary-wing Aerodynamics. Volume 1: Basic Theories of Rotor Aerodynamics with Application to Helicopters.* Contractor Report (CR) NASA-CR-3082. Philadelphia, PA, United States: NASA, 1979. URL: `https://ntrs.nasa.gov/citations/19790013868` (cit. on pp. 22, 23).

[17] I. C. Cheeseman and W. E. Bennett. *The effect of the ground on a helicopter rotor in forward flight.* Technical Report. London: Ministry of Supply, Aeronautical Research Council, 1957. URL: `https://aerade.cranfield.ac.uk/handle/1826.2/3590` (cit. on pp. 26, 64).

[18] Jay Wilhelm and Gina Eberhart. «Development of a Ground Effect BEMT Analysis Method for Multirotor sUAS». In: Jan. 2018. DOI: `10.2514/6.2018-0747` (cit. on pp. 26, 46).

[19] Zhenlong WU, Tianyu ZHANG, Huijun TAN, Haoyu ZHOU, Wei CHEN, and Maixiang XIE. «Hovering rotor aerodynamics in extreme ground effect». In: *Chinese Journal of Aeronautics* 37.7 (2024), pp. 204–219. ISSN: 1000-9361. DOI: `https://doi.org/10.1016/j.cja.2024.02.020`. URL: `https://www.sciencedirect.com/science/article/pii/S1000936124000645` (cit. on pp. 27, 49–51).

[20] J. Xu, J. Yu, X. Lu, Z. Long, Y. Xu, and H. Sun. «Aerodynamic performance and numerical analysis of the coaxial contra-rotating propeller lift system in eVTOL vehicles». In: *Mathematics* 12.1056 (2024). DOI: `10.3390/math12071056`. URL: `https://doi.org/10.3390/math12071056` (cit. on pp. 31, 33, 65, 100).

[21] Hai Li, Zaibin Chen, and Hongguang Jia. «Experimental Investigation on Hover Performance of a Ducted Coaxial-Rotor UAV». In: *Sensors* 23.14 (2023). ISSN: 1424-8220. DOI: `10.3390/s23146413`. URL: `https://www.mdpi.com/1424-8220/23/14/6413` (cit. on pp. 31–33, 70).

[22] Jagan Raj R. and Gowtham G. «Numerical investigation and performance comparison of UAV propeller with varying duct configuration». In: *Aircraft Engineering and Aerospace Technology* 96.5 (2024), pp. 707–714. DOI: `10.1108/AEAT-12-2023-0348` (cit. on pp. 33, 34, 36, 74).

[23] Wei Wei, Shiyi Wei, Zhifang Ke, Meng Guo, Yongjie Shu, Qingkai Meng, Leilei Jia, Maofeng Zhang, and Shurui Han. «Optimizing the Aerodynamic Performance of a Duct–Rotor System for Drones: A Comprehensive Study on the Coupled Parameters». In: *Drones* 9.1 (2025). ISSN: 2504-446X. DOI: `10.3390/drones9010045`. URL: `https://www.mdpi.com/2504-446X/9/1/45` (cit. on pp. 34, 35, 57, 73, 74).

[24] Yanxiong Zhao, Yun Tian, and Zhiqiang Wan. «Aerodynamic Characteristics of a Ducted Fan Hovering and Transition in Ground Effect». In: *Aerospace* 9.10 (Sept. 2022), p. 572. DOI: `10.3390/aerospace9100572` (cit. on pp. 37, 53, 54, 56, 84).

[25] Sema Yilmaz, Doruk Erdem, and M. Kavsaoğlu. «Effects of Duct Shape on a Ducted Propeller Performance». In: Jan. 2013. ISBN: 978-1-62410-181-6. DOI: `10.2514/6.2013-803` (cit. on pp. 37, 74).

[26] Anita I. Abrego, Robert W. Bulaga, and Michael Rutkowski. «Performance Study of a Ducted Fan System». In: *American Helicopter Society Aerodynamics, Acoustics and Test and Evaluation Technical Specialists Meeting.* Preprint (Draft being sent to journal), Work of the US Government, Public Use Permitted. NASA Ames Research Center / Millennium Jet, Inc. San Francisco, CA, United States, Jan. 2002. URL: `https://ntrs.nasa.gov/citations/20020052231` (cit. on p. 38).

[27] Jie () Gong, Jiangming () Ding, and Lianzhou () Wang. «Propeller–duct interaction on the wake dynamics of a ducted propeller». In: *Physics of Fluids* 33.7 (July 2021), p. 074102 (cit. on pp. 38–40).

[28] Antonio Posa and Riccardo Broglia. «Comparison between the wake systems of conventional and ducted propellers». In: *Journal of Fluid Mechanics* 1011 (2025), A15. DOI: `10.1017/jfm.2025.314` (cit. on pp. 39–41, 76).

[29] Donghui Chen, Shanyuan Jiang, Yihua Xu, Yuhao Wang, Jinchao Xiong, and Yun Luo. «Experimental Study on the Ground Effect of Rotor Lift». In: *Nanchang Hangkong University* (2018). Received: Oct. 22nd, 2018; accepted: Nov. 7th, 2018; published: Nov. 14th, 2018. URL: `https://www.researchgate.net/publication/328935255_Experimental_Study_on_the_Ground_Effect_of_Rotor_Lift` (cit. on p. 43).

[30] G. Georgiev. «Blade element – momentum aerodynamic model of a helicopter rotor operating at low-Reynolds numbers in ground effect». In: *Aviation* 29.2 (May 2025), pp. 71–81. DOI: `10.3846/aviation.2025.23587` (cit. on pp. 46–48).

[31] Daniel Griffiths, Shreyas Ananthan, and J. Leishman. «Predictions of Rotor Performance in Ground Effect Using a Free-Vortex Wake Model». In: *Journal of the American Helicopter Society* 50 (Oct. 2005), pp. 302–314. DOI: `10.4050/1.3092867` (cit. on pp. 48, 49).

[32] Michael P. Kinzel, Jason K. Cornelius, Sven Schmitz, Jose L. Palacios, Jack W. Langelaan, Douglas Adams, and Ralph Lorenz. «An Investigation of the Behavior of a Coaxial Rotor in Descent and Ground Effect». In: *Propeller/Rotorcraft/Wind Turbine Aerodynamics I.* 2019. DOI: `10.2514/6.2019-1098` (cit. on p. 52).

[33] Han Han, Changle Xiang, Bin Xu, and Yong Yu. «Experimental and computational investigation on comparison of micro-scale open rotor and shrouded rotor hovering in ground effect». In: *Proceedings of the Institution of Mechanical Engineers, Part G: Journal of Aerospace Engineering* 235 (Aug. 2020), p. 095441002094929. DOI: `10.1177/0954410020949292` (cit. on pp. 55–58, 82, 83, 85).

[34] Yiwei LUO, Tianfu AI, Yuhang HE, Bin XU, Yuping QIAN, and Yangjun ZHANG. «Numerical investigation on unsteady characteristics of ducted fans in ground effect». In: *Chinese Journal of Aeronautics* 36.9 (2023), pp. 79–95. ISSN: 1000-9361. DOI: `https://doi.org/10.1016/j.cja.2023.04.004`. URL: `https://www.sciencedirect.com/science/article/pii/S100093612300119X` (cit. on pp. 56, 58–60, 80–82, 84).

[35] Politecnico di Milano and Airbus A3. *DUST: Documentation and User Manual.* `https://public.gitlab.polimi.it/DAER/dust/-/blob/master/DUST_user_manual/DUST_user_manual.pdf`. 2023 (cit. on p. 61).

[36] APC Propeller Official Website. `https://apcpropeller.com`. Accessed: 2025-09-16. 2025 (cit. on pp. 94–96).

[37] Tytorobotics. *Flight Stand 15.* Accessed: 2025-09-17. 2025. URL: `https://www.tytorobotics.com/pages/flight-stand-15?srsltid=AfmBOorV3CVn5Yp71MyxFsRBz6LERe-dtWAzi_ET7oKDyriwApZaZX3Y` (cit. on pp. 97–99).

[38] Hacker Motor GmbH. *Hacker A50-16S V4 kv365.* Accessed: 2025-09-17. 2025. URL: `https://www.hacker-motor-shop.com/Brushless-Motors/Hacker-Outrunner/Hacker-A50/A50-14pol/A50-16-S-V4-kv365.htm?shop=hacker_e&a=article&ProdNr=15726839&p=6681` (cit. on p. 100).